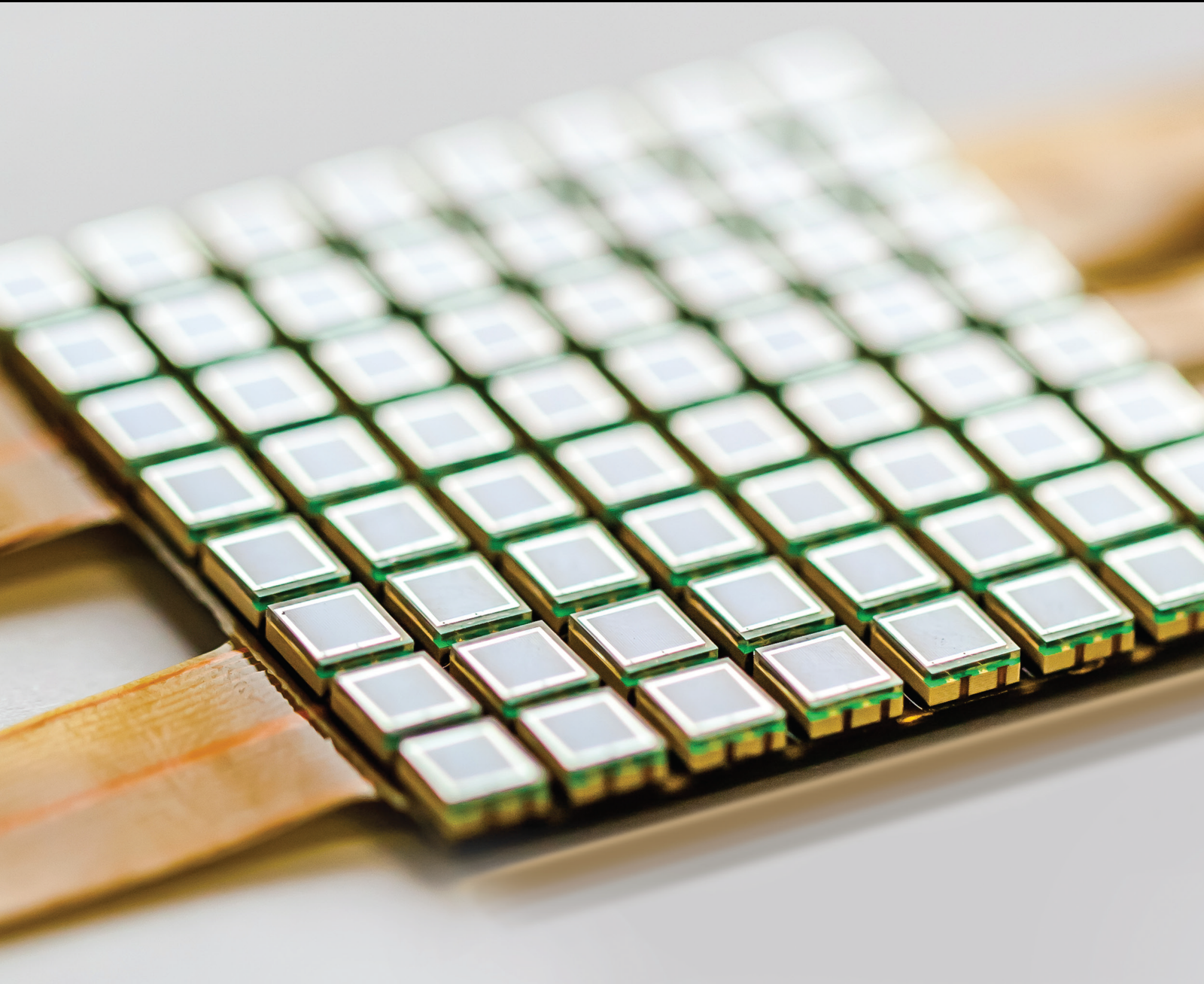


# Wearable and Implantable Sensory Systems for Brain Monitoring

Lead Guest Editor: Mohamed Atef

Guest Editors: Hassan Mostafa, Mousen El-Melegy, Tiago H. Falk, and Salam Gabran





---

# **Wearable and Implantable Sensory Systems for Brain Monitoring**

Journal of Sensors

---

## **Wearable and Implantable Sensory Systems for Brain Monitoring**

Lead Guest Editor: Mohamed Atef

Guest Editors: Hassan Mostafa, Moumen El-  
Melegy, Tiago H. Falk, and Salam Gabran



Copyright © 2020 Hindawi Limited. All rights reserved.



This is a special issue published in "Journal of Sensors." All articles are open access articles distributed under the Creative Commons Attribution License, which permits unrestricted use, distribution, and reproduction in any medium, provided the original work is properly cited.



# Chief Editor

Harith Ahmad , Malaysia

## Associate Editors

Duo Lin , China  
Fanli Meng , China  
Pietro Siciliano , Italy  
Guiyun Tian, United Kingdom

## Academic Editors

Ghufran Ahmed , Pakistan  
Constantin Apetrei, Romania  
Shonak Bansal , India  
Fernando Benito-Lopez , Spain  
Romeo Bernini , Italy  
Shekhar Bhansali, USA  
Matthew Brodie, Australia  
Ravikumar CV, India  
Belén Calvo, Spain  
Stefania Campopiano , Italy  
Binghua Cao , China  
Domenico Caputo, Italy  
Sara Casciati, Italy  
Gabriele Cazzulani , Italy  
Chi Chiu Chan, Singapore  
Sushank Chaudhary , Thailand  
Edmon Chehura , United Kingdom  
Marvin H Cheng , USA  
Lei Chu , USA  
Mario Collotta , Italy  
Marco Consales , Italy  
Jesus Corres , Spain  
Andrea Cusano, Italy  
Egidio De Benedetto , Italy  
Luca De Stefano , Italy  
Manel Del Valle , Spain  
Franz L. Dickert, Austria  
Giovanni Diraco, Italy  
Maria de Fátima Domingues , Portugal  
Nicola Donato , Italy  
Sheng Du , China  
Amir Elzwawy, Egypt  
Mauro Epifani , Italy  
Congbin Fan , China  
Lihang Feng, China  
Vittorio Ferrari , Italy  
Luca Francioso, Italy

Libo Gao , China  
Carmine Granata , Italy  
Pramod Kumar Gupta , USA  
Mohammad Haider , USA  
Agustin Herrera-May , Mexico  
María del Carmen Horrillo, Spain  
Evangelos Hristoforou , Greece  
Grazia Iadarola , Italy  
Syed K. Islam , USA  
Stephen James , United Kingdom  
Sana Ullah Jan, United Kingdom  
Bruno C. Janegitz , Brazil  
Hai-Feng Ji , USA  
Shouyong Jiang, United Kingdom  
Roshan Prakash Joseph, USA  
Niravkumar Joshi, USA  
Rajesh Kaluri , India  
Sang Sub Kim , Republic of Korea  
Dr. Rajkishor Kumar, India  
Rahul Kumar , India  
Nageswara Lalam , USA  
Antonio Lazaro , Spain  
Chengkuo Lee , Singapore  
Chenzong Li , USA  
Zhi Lian , Australia  
Rosalba Liguori , Italy  
Sangsoon Lim , Republic of Korea  
Huan Liu , China  
Jin Liu , China  
Eduard Llobet , Spain  
Jaime Lloret , Spain  
Mohamed Louzazni, Morocco  
Jesús Lozano , Spain  
Oleg Lupan , Moldova  
Leandro Maio , Italy  
Pawel Malinowski , Poland  
Carlos Marques , Portugal  
Eugenio Martinelli , Italy  
Antonio Martinez-Olmos , Spain  
Giuseppe Maruccio , Italy  
Yasuko Y. Maruo, Japan  
Zahid Mehmood , Pakistan  
Carlos Michel , Mexico  
Stephen. J. Mihailov , Canada  
Bikash Nakarmi, China



Ehsan Namaziandost , Iran  
Heinz C. Neitzert , Italy  
Sing Kiong Nguang , New Zealand  
Calogero M. Oddo , Italy  
Tinghui Ouyang, Japan  
SANDEEP KUMAR PALANISWAMY ,  
India  
Alberto J. Palma , Spain  
Davide Palumbo , Italy  
Abinash Panda , India  
Roberto Paolesse , Italy  
Akhilesh Pathak , Thailand  
Giovanni Pau , Italy  
Giorgio Pennazza , Italy  
Michele Penza , Italy  
Sivakumar Poruran, India  
Stelios Potirakis , Greece  
Biswajeet Pradhan , Malaysia  
Giuseppe Quero , Italy  
Linesh Raja , India  
Maheswar Rajagopal , India  
Valerie Renaudin , France  
Armando Ricciardi , Italy  
Christos Riziotis , Greece  
Ruthber Rodriguez Serrezuela , Colombia  
Maria Luz Rodriguez-Mendez , Spain  
Jerome Rossignol , France  
Maheswaran S, India  
Ylias Sabri , Australia  
Sourabh Sahu , India  
José P. Santos , Spain  
Sina Sareh, United Kingdom  
Isabel Sayago , Spain  
Andreas Schütze , Germany  
Praveen K. Sekhar , USA  
Sandra Sendra, Spain  
Sandeep Sharma, India  
Sunil Kumar Singh Singh , India  
Yadvendra Singh , USA  
Afaque Manzoor Soomro , Pakistan  
Vincenzo Spagnolo, Italy  
Kathiravan Srinivasan , India  
Sachin K. Srivastava , India  
Stefano Stassi , Italy

Danfeng Sun, China  
Ashok Sundramoorthy, India  
Salvatore Surdo , Italy  
Roshan Thotagamuge , Sri Lanka  
Guiyun Tian , United Kingdom  
Sri Ramulu Torati , USA  
Abdellah Touhafi , Belgium  
Hoang Vinh Tran , Vietnam  
Aitor Urrutia , Spain  
Hana Vaisocherova - Lislalova , Czech  
Republic  
Everardo Vargas-Rodriguez , Mexico  
Xavier Vilanova , Spain  
Stanislav Vitek , Czech Republic  
Luca Vollero , Italy  
Tomasz Wandowski , Poland  
Bohui Wang, China  
Qihao Weng, USA  
Penghai Wu , China  
Qiang Wu, United Kingdom  
Yuedong Xie , China  
Chen Yang , China  
Jiachen Yang , China  
Nitesh Yelve , India  
Aijun Yin, China  
Chouki Zerrouki , France


## Contents

---

**DWT-Net: Seizure Detection System with Structured EEG Montage and Multiple Feature Extractor in Convolution Neural Network**

Zhe Zhang, Yun Ren, Nabil Sabor, Jing Pan, Xiaona Luo, Yongfu Li , Yucai Chen , and Guoxing Wang  
Research Article (13 pages), Article ID 3083910, Volume 2020 (2020)

**A Multichannel fNIRS System for Prefrontal Mental Task Classification with Dual-level Excitation and Deep Forest Algorithm**

Cheng Chen, Yizhen Wen, Shaoyang Cui, Xiangao Qi, Zhenhong Liu, Linfeng Zhou, Mingyi Chen, Jian Zhao , and Guoxing Wang  
Research Article (10 pages), Article ID 1567567, Volume 2020 (2020)

**Improved Spatial Resolution of Electroencephalogram Using Tripolar Concentric Ring Electrode Sensors**

Xiang Liu, Oleksandr Makeyev , and Walter Besio   
Research Article (9 pages), Article ID 6269394, Volume 2020 (2020)

**Time-Frequency Linearization of Reactive Cortical Responses for the Early Detection of Balance Losses**

Giovanni Mezzina , and Daniela De Venuto   
Research Article (14 pages), Article ID 9570748, Volume 2019 (2019)

## Research Article

# DWT-Net: Seizure Detection System with Structured EEG Montage and Multiple Feature Extractor in Convolution Neural Network

Zhe Zhang,<sup>1</sup> Yun Ren,<sup>2</sup> Nabil Sabor,<sup>1,3</sup> Jing Pan,<sup>2</sup> Xiaona Luo,<sup>2</sup> Yongfu Li ,<sup>1</sup> Yucai Chen ,<sup>2</sup> and Guoxing Wang<sup>1</sup>

<sup>1</sup>Department of Micro-Nano Electronics and MoE Key Lab of Artificial Intelligence, Shanghai Jiao Tong University, Shanghai 200240, China

<sup>2</sup>Department of Neurology, Shanghai Jiao Tong University Affiliated Children's Hospital of Shanghai, Shanghai 200062, China

<sup>3</sup>Electrical and Electronics Engineering Department, Faculty of Engineering, Assiut University, Assiut 71516, Egypt

Correspondence should be addressed to Yongfu Li; liyongfu.sg@gmail.com and Yucai Chen; chenyc@shchildren.com.cn

Received 21 November 2019; Revised 3 July 2020; Accepted 30 July 2020; Published 25 August 2020

Academic Editor: Moumen El-Melegy

Copyright © 2020 Zhe Zhang et al. This is an open access article distributed under the Creative Commons Attribution License, which permits unrestricted use, distribution, and reproduction in any medium, provided the original work is properly cited.

Automated seizure detection system based on electroencephalograms (EEG) is an interdisciplinary research problem between computer science and neuroscience. Epileptic seizure affects 1% of the worldwide population and can lead to severe long-term harm to safety and life quality. The automation of seizure detection can greatly improve the treatment of patients. In this work, we propose a neural network model to extract features from EEG signals with a method of arranging the dimension of feature extraction inspired by the traditional method of neurologists. A postprocessor is used to improve the output of the classifier. The result of our seizure detection system on the TUSZ dataset reaches a false alarm rate of 12 per 24 hours with a sensitivity of 59%, which approaches the performance of average human detector based on qEEG tools.

## 1. Introduction

Electroencephalograph (EEG) recording refers to the measurement of electrical activity resulting from postsynaptic potentials within the brain [1]. The EEG analysis is used for diagnosing neural dysfunction, such as epileptic seizure, cerebrovascular disease, and brain tumor. With the fast development in data science and machine/deep learning techniques of past decades, automated EEG analysis has great potential in bringing forward an attractive advancement in accuracy and efficiency of diagnosis and treatment of neural dysfunctions [1].

The basic requirement for treatment in different kinds of epilepsy is to identify epileptic seizure features from EEG signals. The equipment for EEG signal acquisition systems is relatively inexpensive; however, the cost for training or hiring a certified neurologist to read and report EEG data is considerably much higher [2]. At the moment, the interpretation of

EEG recordings depends heavily on the judgment of neurologists [3]. It is also time-consuming and tedious to perform 24/7 EEG monitoring to avoid missing epileptic cases [4]. Moreover, the nonstationary nature [5] of EEG and artifacts provides both interrater and intrarater disagreements that degrade diagnosis validity [6]. An automated EEG diagnostic system that provides effective, subjective, and accurate seizure detection is thus needed.

The problem of automatic seizure detection can be divided into two main steps, feature extraction and classifier training. Considerable amounts of works have been done with this two-step procedure for better detection accuracy, including time-frequency feature map with a support vector machine (SVM) [3, 7], nonlinear features with different types of classifiers [5, 8, 9], and features based on time-frequency image with image recognition methods [10, 11]. These researches have provided different methodologies for seizure detection. However, since these works have only been

validated on datasets with less than 25 patients [3], additional verifications are required to validate their methods on a larger dataset. Additional signal processing techniques might be required to fine-tune their methods for practical usage. Recently, an increasing number of researchers start to utilize neural network (NN) methods due to its inherent automatic feature extraction characteristics [12–14]. San-segundo et al. analyzed the use of deep neural network for epileptic EEG signal classification with different inputs and suggested empirical mode decomposition for better performance in focal versus nonfocal classification and Fourier transform for seizure detection [15]. Tsiouris et al. presented the long short-term memory (LSTM) method in seizure detection using EEG signals, expanding the use of traditional deep learning algorithms in this field [16]. However, a common problem of these NN methods is that few of them take advantage of existing neurological knowledge to improve the model’s accuracy and converge speed.

Controlling of feature extraction provides us with the method to apply neurological knowledge to the model. ChronoNet [17] introduced the concept of multiple-time-scale feature extraction, where inception layers encode time-series information before fusion of the EEG signal. However, this work treats the EEG channels as feature channels at the beginning of the model, failing to learn signal patterns of individual EEG channels. Eberlein et al. [12] performed convolution on EEG signals with kernels ranging over multiple channels to detect local patterns instead of a single channel. Although the authors tried several topologies over the number of channels to be convoluted together, the accuracy is limited due to insufficient representative features in EEG recordings. Both works introduced the idea of manually adjusting the input domain in the early stage of the neural network in seek of better performance of their model. However, to the best of our knowledge, none of the existing research has conducted feature extraction techniques on both temporal and regional patterns as in the field of seizure detection.

To address the aforementioned issues, we propose to use wavelet coefficient packages as input features and introduce the concept of local pattern inception into the neural network model as our seizure detection system. Our model is trained and examined with an up-to-date real clinical EEG dataset [18] that provides a sensitivity of 59.07% at a false alarm rate of 12/24 hours, reaching the average human performance [19].

The key contributions of our work are summarized as follows:

- (1) *Dataset Preparation.* We propose a single reference EEG montage for seizure detection to solve the problem of independence and dependence of adjacent electrodes.
- (2) *Feature Extraction.* We propose a feature extraction method inspired by neurologists’ way of reading EEG to improve feature extraction of DWT-Net for seizure detection with efficient computing cost.
- (3) *Neural Network Optimization.* We optimize the kernel size of the convolution layers to deal with differ-

ent temporal resolutions of various discrete wavelet coefficients.

- (4) *Postprocessor.* We optimize the system by concatenating the classifier with a finite-state-machine postprocessor.

The rest of the paper is organized as follows: Section 2 presents preliminaries about EEG recording methods and seizure detection datasets with problem definition. In Section 3, we propose our seizure detection system with detailed methods including feature extraction, network structure, and postprocessor. The experimental results and discussion are presented in Section 4, followed by conclusion in Section 5.

## 2. Preliminaries

In this section, we will discuss the present EEG recording techniques and related datasets and define our problem statement based on the evaluation matrices.

*2.1. EEG Recording Methods.* For clinical epilepsy treatment, noninvasive EEG signal recording is a preferable method because of ethical concerns and medical risks [20]. EEG signals are typically acquired with equipment via the potential difference between pairs of recording electrodes placed on the scalp surface. The measurement between any two electrodes is considered an EGG channel.

According to the “International 10-20 system” measurement standard, the electrodes are distributed across the brain scalp to ensure the reproducibility of EEG experiment [21]. The notation of “10” and “20” defines that the distances between adjacent electrodes are either 10% or 20% of the total longitudinal or transverse distance of the skull. There are a total of 19 recording electrodes and two referential electrodes. Each electrode has a “positional” code and a number; an odd number represents the left brain position, and an even number represents the right brain. As illustrated in Figure 1, the electrode “T3” is termed as temporal lobe (T) on the left side of the brain.

EEG signals are presented in the form of either single reference or bipolar montage, as shown in Figure 2, where a montage is defined as an ordered list of EEG channels recorded in a regular time interval [22]. Both types of montages are used by the clinicians to understand the origin and location of epileptic seizure signals. A single reference montage is also known as a referential montage with one or two referential electrodes. The referential electrodes can be auricular electrodes or averaged potential of all the electrodes. They are paired with the recording electrodes to form the channels in a single reference montage. A bipolar montage does not have referential electrodes, and it records the potential differences between pairs of recording electrodes [23].

*2.2. EEG Datasets.* To develop an automatic seizure detection system, an EEG database with well-defined epileptic recordings is required. Table 1 provides a list of open-source seizure detection datasets (corpora).

The “Bonn” corpus, from the University of Bonn [24], has been widely used for research on seizure detection [8, 11, 25].

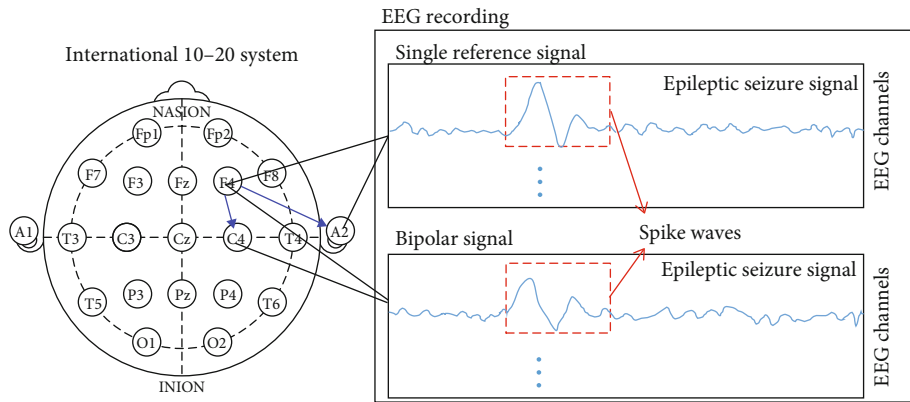


FIGURE 1: Common EEG recording method used for epileptic seizure detection.

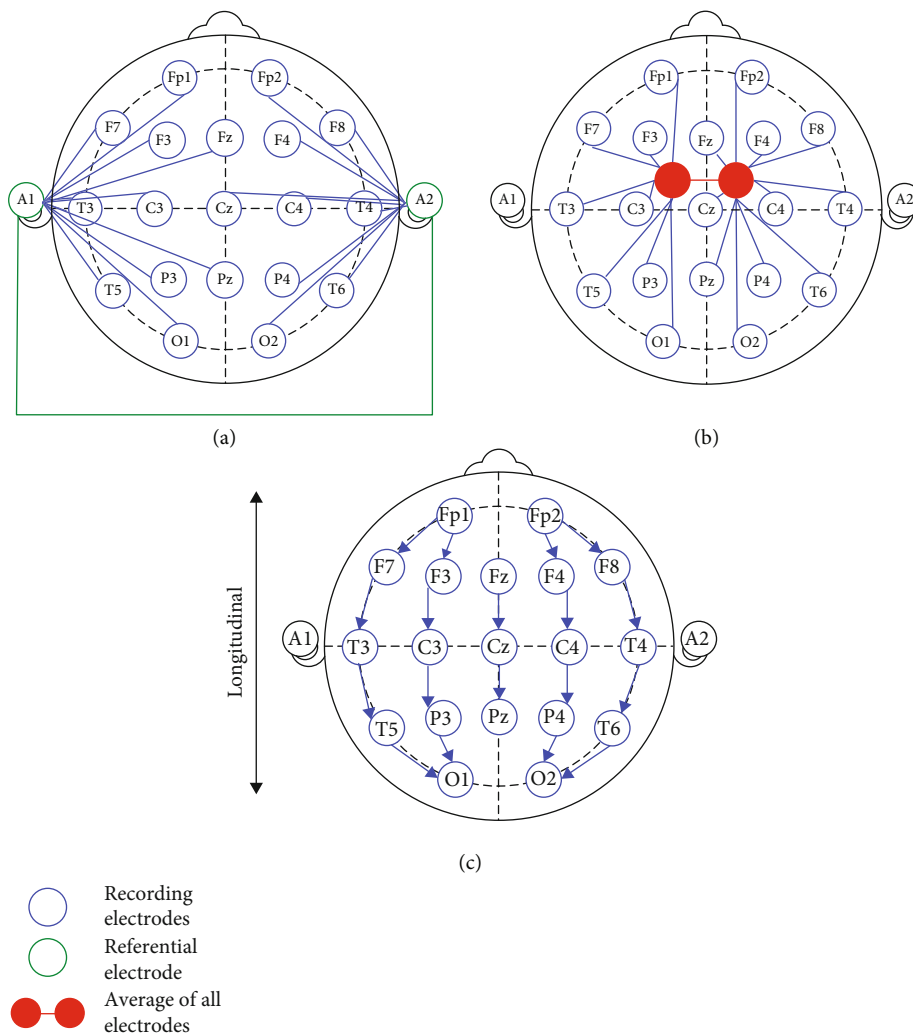


FIGURE 2: Three common EEG montages: (a) the auricular reference montage that uses electrodes on ears as referential electrodes, (b) the common average montage that uses averaged potential of all the electrodes as the referential electrode, and (c) the longitudinal bipolar montage that records the potential difference between pairs of recording electrodes.

It includes single-channel EEG recordings with a total number of 10 subjects and 100 seizure occurrences. All the EEG signals in the corpus were manually reviewed by professional clinicians to pick the representative epileptic channel and to

remove recordings with artifacts. Hence, each session retains only one EEG channel measurement.

The “CHB-MIT” scalp EEG corpus [3, 26] is another widely used dataset for seizure detection [11, 27, 28]. It



TABLE 1: Open source EEG corpus for seizure detection.

	Bonn	CHB-MIT	TUSZ
Number of subjects	10	23	315
Number of seizure occurrence	100	163	1791
Total seizure time	0.6 hours	2.8 hours	36 hours
Total record time	3.2 hours	175 hours	797 hours
% of seizure time/total time	1.88%	1.6%	4.5%
Number of seizure type	1	1	7
Number of channels	1	19	19

consists of continuous scalp EEG recordings from 23 pediatric patients undergoing medication withdrawal for epilepsy surgery evaluation at Children’s Hospital, Boston. The corpus includes 19-channel EEG recordings with a total number of 163 seizure occurrences and a total record time of 175 hours.

The Temple University Hospital Seizure Detection Corpus (TUSZ) [29] is the largest open-source EEG corpus for seizure detection and provides an accurate representation of actual clinical conditions. This corpus is still undergoing updates, and the version used in this paper is v1.5.0. Currently, this corpus includes 19-channel EEG recordings with a total number of 315 subjects, 1791 seizure occurrences, and a total record time of 797 hours. In particular, this corpus is the only dataset that provides different types of epileptic seizure signal. Ref. [30, 31] completed a benchmark on the classification of different types of seizures in TUSZ.

Since “Bonn” and “CHB-MIT” corpuses lack sufficient subjects and data, both corpus might not be a good representative of the real-world clinical situations [32]. Hence, we have adopted the “TUSZ” corpus for our study to develop a seizure detection system.

**2.3. Problem Formulation and Definitions.** We define the following evaluation matrices used to evaluate the performance of a seizure detection system against the “TUSZ” corpus.

*Definition 1. (seizure density function).* An ideal seizure detection system or human marker is expected to label each seizure in the recordings with an accurate start time and end time. An evaluation method [6] is considered to describe the EEG signals by a seizure density function, which varies between 0 and 1 throughout the record. An ideal density function of a detection system is a function of time with the value 1 during the detections and 0 elsewhere.

*Definition 2. (sensitivity (Sen)).* Sensitivity is defined as the ratio between the total number of detected seizure events and the total number of all labelled seizure events in the EEG record,

$$\text{Sen} = \frac{\text{Total number of correctly recognized seizure events}}{\text{Total number of labelled seizure events}}, \quad (1)$$

where a detected seizure event is defined if the average value of seizure density function over the event duration exceeds the threshold  $p$ .

*Definition 3. (specificity (Sp)).* Specificity is defined as the ratio between the number of detected normal event and the total number of all labelled normal events in the EEG record,

$$\text{Sen} = \frac{\text{Total number of recognized normal events}}{\text{Total number of labelled normal events}}, \quad (2)$$

where a normal event is defined if the average value of seizure density function over the event duration falls below the threshold  $p$ .

*Definition 4. (true positive rate (TPR)).* The true positive rate is defined as the ratio between the number of detected seizure events and the total number of events recognized as seizure events,

$$\text{TPR} = \frac{\text{Total number of correctly recognized seizure events}}{\text{Total number of detected seizure events}}. \quad (3)$$

*Definition 5. (false alarm rate (FAR)).* A false alarm occurs if the integral of seizure density function over a nonseizure event exceeds seizure density threshold  $p$ . The false alarm rate over a period of 24 hours is defined as the ratio between the number of false alarm events and the duration of the EEG recorded in the unit of 24 hours.

$$\text{FAR} = \frac{\text{Total number of false alarm events}}{\text{Total duration}}. \quad (4)$$

With the above definitions, the epileptic seizure detection problem is formulated as follows.

*Problem 1. (epileptic seizure detection).* Given a corpus that contains EEG channels with normal and seizure events, train a seizure detection system based on sliding window method. For each sliding window, the sensitivity and specificity of whether it contains a seizure event should be maximized. For the final output of the system, the false alarm rate of seizure events detection should be minimized.

### 3. Feature Extraction Methods and Neural Network Model

#### 3.1. Feature Extraction

**3.1.1. Montage Selection.** The number of channels and the selection of EEG montage have a direct impact on the performance of the classification system [33]. In the TUSZ corpus, it contains more than 40 different channel configurations and 4 different types of reference points. As shown in Figure 3, after our preliminary study on channel selection based on [34, 35], we have decided to use 19 channels from single reference montage based on the “International 10-20 system” to ensure the generality of our model.



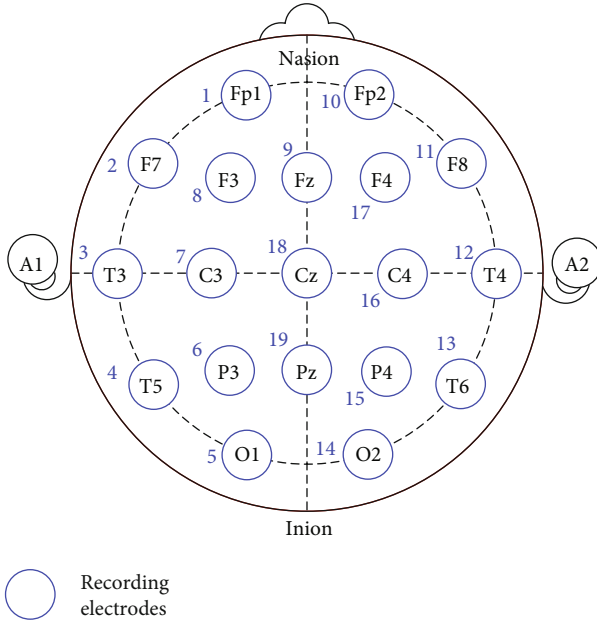


FIGURE 3: Channel sequence of the proposed single reference montage. The sequence is derived from the longitudinal bipolar montage and presented with numbers.

In this work, we have arranged the single reference EEG channels in a new montage to extract the spatial information of the EEG signals. The order of the channels is derived from the longitudinal bipolar montage recommended by standard neurophysiology guidelines [36]. In this montage, each pair of recording electrodes from neighboring channels corresponds to a channel in the longitudinal bipolar montage. For example, the pair of channel Fp1-reference and F7-reference corresponds to Fp1-F7 in the bipolar montage. A bipolar montage can be derived from single reference montages, because the subtraction of two channels with the same referential electrode would cancel the effects of the reference point [37]. Hence, this single reference montage that maintains the bipolar sequence enables the neural network not only to detect features from the single reference electrodes but also make it possible to draw information from the difference between two neighboring electrodes, which mimics the bipolar montage. Compared with other montages, the proposed single reference montage provides the classifier with more information than only using traditional single reference or bipolar montages as the input signal. The related experimental results will be discussed in Section 4.

**3.1.2. Window Length Selection.** To derive the seizure density function from continuous EEG recordings, the EEG signals need to be processed with moving-window analysis. Neurologists typically evaluate the symptom based on 10-second windows of EEG signals [14]. However, a large proportion of the events in the “TUSZ” corpus are shorter than 10 seconds. Thus, we have selected two shorter windows, 1-second and 5-second windows. With the 250 Hz sampling rate of the TUSZ corpus, the 1-second and 5-second windows

contain 19 single reference EEG channels with 250 and 1250 sampling points per channel, respectively.

**3.1.3. EEG Noise Removal and Normalization.** An eighth-order Butterworth filter of 49 to 51 Hz was applied to each window to filter out power-line noise. Each signal was further normalized with Z-score normalization [38], obeying the following equation:

$$X = \frac{x - x_{\text{mean}}}{\sigma_x}, \quad (5)$$

where  $x_{\text{mean}}$  and  $\sigma_x$  represent the mean value and the standard deviation of this EEG within the window duration. The result of Z-score normalization is a signal with zero mean and a standard deviation of 1.

**3.1.4. Discrete Wavelet Transformation.** Discrete wavelet transformation (DWT) is a wavelet decomposition method [39]. This method decomposes a discrete signal into packages of coefficients that represent approximate and detailed information by calculating the inner product of the signal and mother wavelet functions. EEG signals can be seen as a time sequence signal consisting of different frequency components. Thus, the packages of coefficients correspond to the lower and higher frequency component of the signal, respectively. As shown in Figure 4, a detailed package represents a frequency component  $D_{n,m}$ , which corresponds to the frequency range of  $[fs/2^{m+1} \text{ Hz}, fs/2^m \text{ Hz}]$ , where  $fs$  is the sampling rate (250 Hz),  $m = 1, 2, \dots, n$ , and  $n$  is the total level of decomposition.

Most of the related studies use inverse-DWT after DWT to reconstruct EEG into time-sequence signals of different frequency components [5, 25, 28]. In our study, we use the coefficients directly as input features. This method has been tested in other fields such as fault diagnosis [40].

The fourth Daubechies mother wavelet function (db4) is a widely used mother wavelet function in the field of EEG analysis [10, 35, 41]. The morphological characteristic of this mother wavelet function resembles EEG signals. From our preliminary study, we have identified four wavelet coefficient packages decomposed by db4 that represent the lowest frequency components of the EEG, as those frequency components are more related to epileptic signals. The length of the db4 wavelet filter is 8. We can get the length of the decomposed coefficient package, by the following equation

$$\text{Len}(\text{coef } f) = \text{floor} \left[ \frac{(\text{len}(\text{data}) + \text{len}(\text{filter}) - 1)}{2} \right]. \quad (6)$$

The wavelet decomposition stops when the signal becomes shorter than the db4 filter length. Based on the origin signal length 1250 and 250, the maximum decomposition level for 5-second window and 1-second window are 7 and 5, respectively. We take the middle of 1024 sampling points from 1250 sampling points for 5-second windows and 260 sampling points with overlapping of 10 sampling points for 1-second windows. With this method, the length of the coefficient packages representing the lowest frequency components

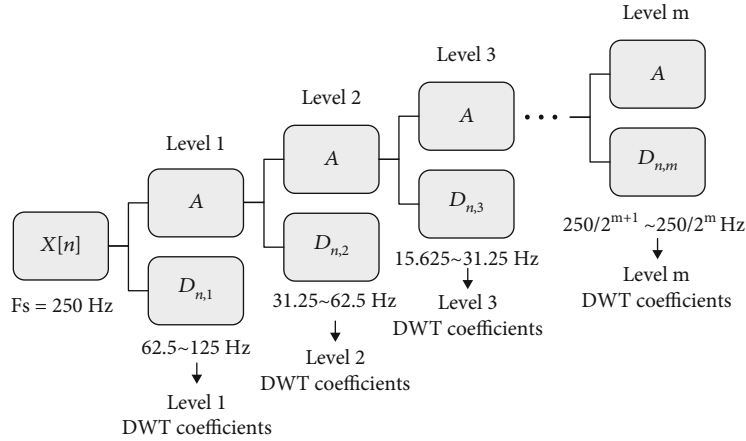


FIGURE 4: An illustration of discrete wavelet transformation used in 5-second window.  $n$  is chosen as 6. For 1-second window, the maximum decomposition level is limited to 5 due to fewer sampling points.

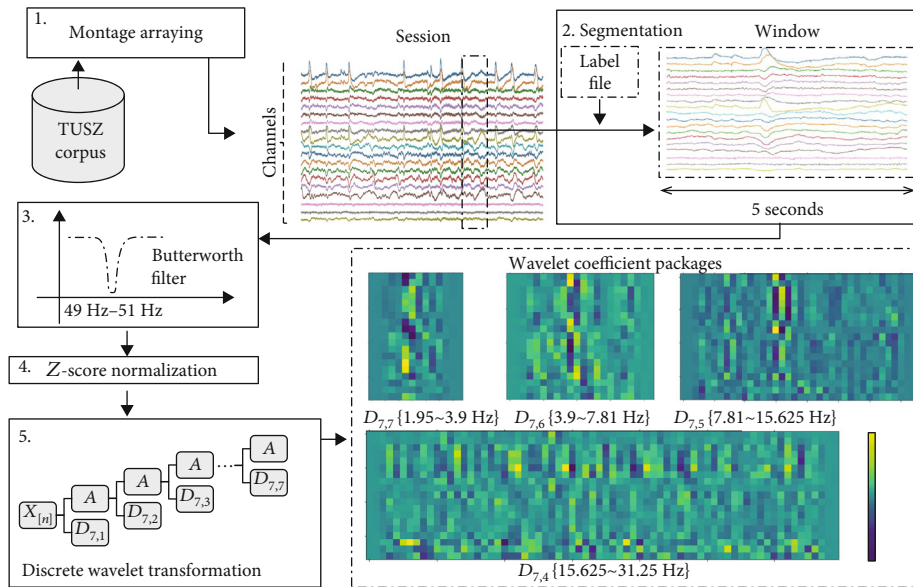


FIGURE 5: Systematic flow of the proposed feature extraction method with 5-second window. Firstly, the EEG signals from TUSZ dataset are restructured into the proposed montage of 19 channels. Secondly, 5-second windows of epileptic and normal EEG are extracted according to the labeling file of the sessions. The windows then go through a Butterworth filter to eliminate power-line interference. After Z-score normalization, the signal is decomposed into discrete wavelet coefficients. Four coefficient packages representing information of lower frequency bands are used as input of the classifier.

for both 1-second and 5-second windows will be 14, 22, 38, and 70, making our model suitable for both window sizes. The proposed feature extraction method is summarized and illustrated in Figure 5.

**3.2. DWT-Net Structure.** Neurologists read EEG signals and recognize abnormal waveforms in the individual channels as well as the correlations between adjacent EEG channels [1]. Their method seeks features from both the time-frequency domain and the spatial domain to ensure that epileptic signals that are unclear in a single domain can be detected.

In this work, we designed a CNN structure called DWT-Net to mimic the above feature extraction methodology. The

model has 9 layers and generates the seizure density of each EEG window. The input of our model is four coefficient packages with sizes of  $C * L_i$  ( $i = 0, 1, 2, 3$ ), where  $C$  represents the number of preprocessed input EEG channels and  $L_i$  represents the length of  $i_{th}$  coefficient package. According to the preprocessed data,  $C$  is 19 and  $L_i$  equals to 14, 22, 38, and 70, respectively.

After the input layer, we implemented multiple feature extractors to process the wavelet packages separately. The method of multiple feature extractors has been used to model local pairwise feature interactions for image recognition [42]. To mimic the abnormal signal identification methodology of neurologists, we extended the concept and implemented a 4-way feature extractor to guide the model. As a result, the

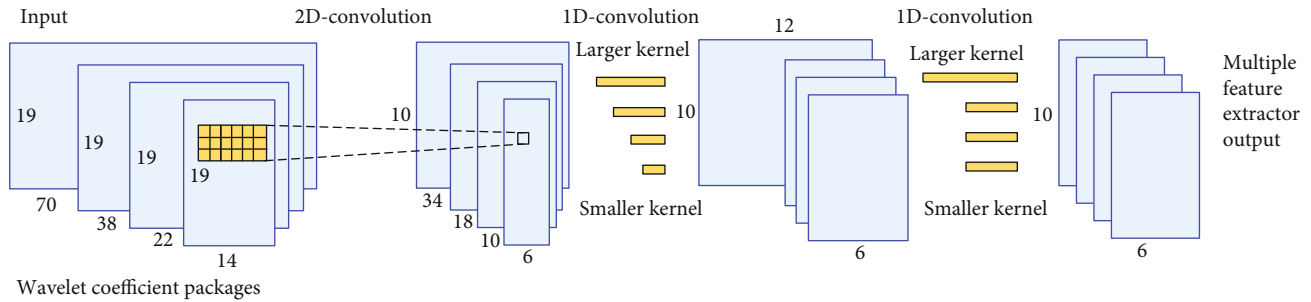


FIGURE 6: Using larger 1D convolution kernel for feature map with larger temporal resolution to normalize the feature maps of the multiple feature extractor.

model will extract features along different domains in a pre-defined order. The second dimension of the feature maps refers to the time steps in the wavelet coefficient packages. It is illustrated in Figure 6 that by adjusting the second dimension of the kernel sizes, strides, and paddings of our convolution layers, we can normalize the temporal resolutions of different DWT coefficient packages. As shown in Figure 7, the details of the model with multiple feature extractors are described as follows:

- (1) 4 wavelet coefficient packages are fed to the 4-input feature extractors
- (2) Each package undergoes the first convolution layer with a kernel size of (3, 6) and stride of 2 for the inception of local temporal and spatial features. The first dimension of the kernel size refers to the number of channels involved in the convolution and is chosen to be 3. With a stride of 2, it ensures that each EEG channel has a chance to interact with neighboring 2 channels. Note that the first convolution layer halves feature dimension along the number of channels
- (3) Two 1d convolution layers are used to extract features along with the temporal dimension of each channel. Different sizes of kernels are used in these two layers between feature extractors for different input coefficient packages. The kernels in size of (1,  $N$ ) with larger  $N$  are used for longer coefficient packages, as shown in Figure 6. The sizes of  $N$ , strides, and paddings are carefully chosen to ensure that the shape of output feature maps is normalized correctly
- (4) The output of the third convolution layer is convolved using a kernel size of (3, 3)
- (5) A max-pooling layer is applied to the product of the last kernel, reducing the feature map size to  $5 \times 3$
- (6) The feature map then goes through a dropout layer with a 50% dropout proportion to achieve the effect of auto denoising and prevent overfitting
- (7) The results of 4 feature extractors are stacked by the first dimension into a 3D feature space of  $4 \times 5 \times 3$ .

The first dimension now represents the frequency-domain of the signal

- (8) The last convolution layer with a kernel size of 3 is applied to the 3D feature map. This layer fuse features from different frequency bands together
- (9) Another max-pooling layer is used to reduce the size of the feature map to  $2 \times 3 \times 2$
- (10) The resulting 768 features are fully connected to the output of 2 neurons after two fully connected layers

**3.3. Designing of the Real-Time System.** The softmax output from the classifier is a probability vector of a dimension two, including the probability of the  $n^{\text{th}}$  EEG window to be epileptic EEG  $P_{\text{seizure}}$  and the probability of the  $n^{\text{th}}$  EEG window to be normal EEG  $P_{\text{normal}}$ . As illustrated in Algorithm 1, the postprocessor processes the EEG signal windows by sequence. Starting with state=negative, once the  $n^{\text{th}}$  window is detected as epileptic, the result of the  $n^{\text{th}}$  EEG window  $\text{Result}_n$  will be set to Epileptic and the state is changed to Positive (lines 8-9). Under this condition, the system raises the possibility of the next two windows to be epileptic by  $P_{\text{up}}$ , which is set to 0.1 in this work. If the next 2 consecutive windows  $\text{Result}_{n+1}$  and  $\text{Result}_{n+2}$  failed to be detected as Epileptic. The  $n^{\text{th}}$  window will be regarded as a false alarm and  $\text{Result}_n$  will be revised to Normal (line 25). Likewise, a single Normal window between two Epileptic windows will be revised to Epileptic. Although such postprocessor brings about a latency of 10 seconds, the proposed postprocessor smooths the sequential hypotheses of the classifiers and provides a moderate effect in suppressing FAR and increasing Sen.

## 4. Experiment Results and Discussion

**4.1. Dataset Preparation.** In this work, we have chosen the latest version v1.5.0 of the “TUSZ” corpus. In TUSZ, the EEG labels are given with a start time and an end time for each EEG recording. The resolution of the labels in the TUSZ dataset is 0.0001 second. We can define an event with its start time and end time. The sessions of the corpus that includes eight classes of events (“background” event and 7 “epileptic” events) are listed in Table 2. As we are not going to include seizure classification in our system, all the epileptic classes

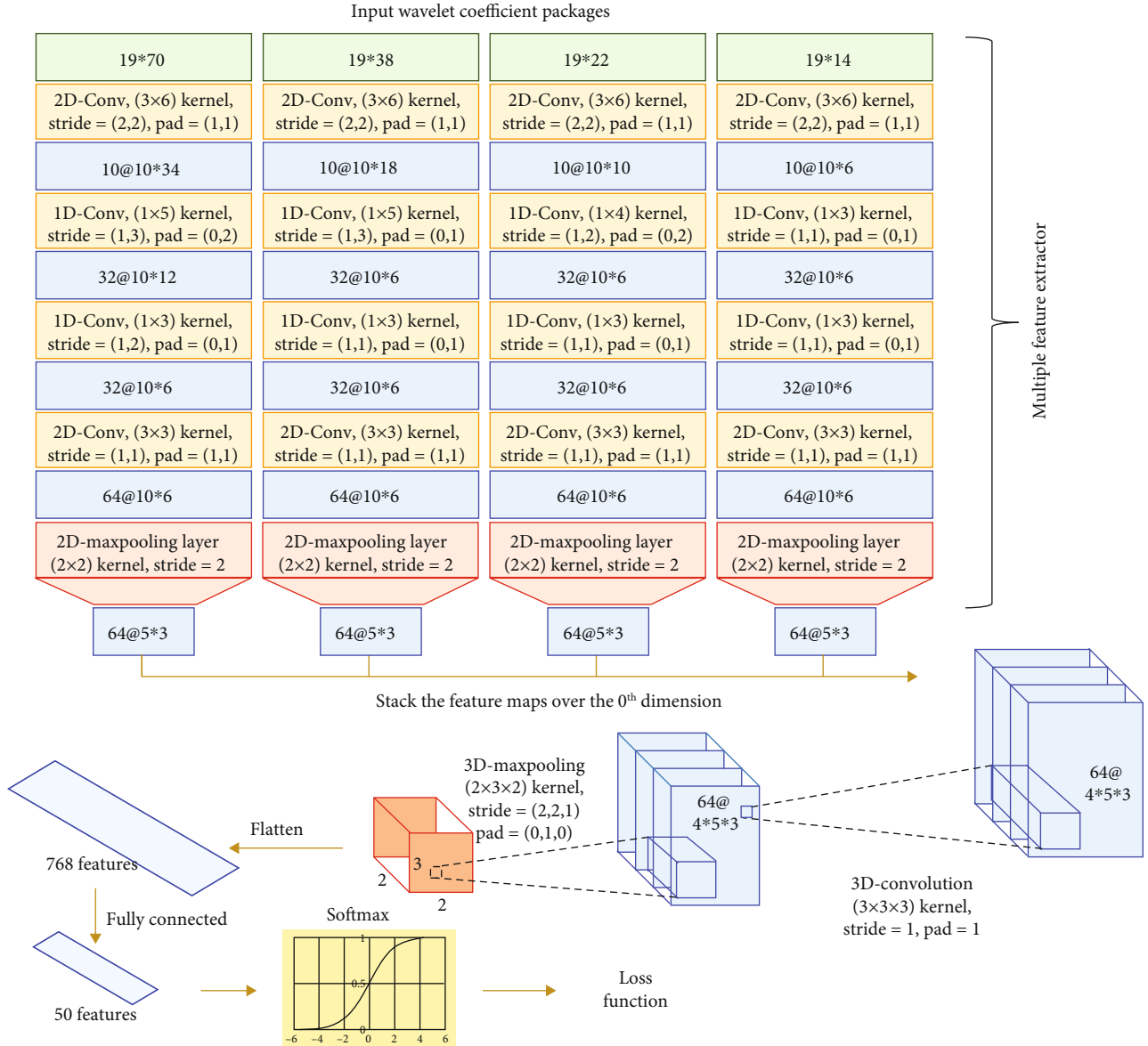


FIGURE 7: Structure of DWT-Net. The upper part illustrates the structure of multiple feature extractor proposed for better feature extraction performance with regard to epileptic EEG signal. In the bottom part, outputs of the multiple feature extractor are stacked into a 3D feature map, which goes through common convolution layers for classification.

are considered “positive” events and the background class “negative” events in the experiment, respectively. Because the window length of our seizure detection system is only 5 seconds, we regard seizure events with short breaks as separate events to make the best use of the labels.

The first minute of an EEG recording provides tale-tail signs whether the signal is epileptic or not because the epileptic signal is strongest at the beginning of a seizure [17]. Hence, limiting the length of the events can provide better classification performance. However, extracting only 60 seconds of signal from the events will result in shortage of training data required for training a deep learning model and make the classifier less adaptable. To balance the amount of training data and classifier performance, for events greater than 400 seconds, only the first 400 seconds are included.

A total number of 6971 and 2238 sessions were used as the train and test sets predefined by TUSZ. After feature extraction, 119,491 5-second windows were generated with details showed in Table 3. Correspondingly, the 1-second windows were derived from the 5-second windows.

**4.2. Training of Window-Based Classifier.** The proposed model was constructed with the open-source framework Pytorch [43]. The weights of the neural network were initialized with Kaiming normalization [44] to improve weight convergence during the training of our model with ReLu activation layers. The weighted cross-entropy was selected as the loss function of the classifier. We have used the Adam optimization method [45] with  $\beta_1$  of 0.9,  $\beta_2$  of 0.999, learning rate of 0.0005, and weight decay (L2 penalty regularization)

```

Require:  $P_{seizure}$ ,  $P_{normal}$ ,  $P_{up}$ 
Output:  $Result_n$ ,  $n=1,2,\dots$ 
1: Initialize System State  $State \leftarrow Negative$ 
2: while New EEG window do
3:   if  $State == Negative$  then
4:     if  $P_{seizure} < P_{normal}$  then
5:       next  $State \leftarrow Negative$ 
6:        $Result_n \leftarrow Normal$ 
7:     else
8:       next  $State \leftarrow Positive$ 
9:        $Result_n \leftarrow Epileptic$ 
10:    end if
11:  end if
12:  if  $State == Positive$  then
13:    if  $P_{seizure} + P_{up} < P_{normal}$  then
14:      next  $State \leftarrow Smooth$ 
15:       $Result_n \leftarrow Normal$ 
16:    else
17:      next  $State \leftarrow Positive$ 
18:       $Result_n \leftarrow Epileptic$ 
19:    end if
20:  end if
21:  if  $State == Smooth$  then
22:    if  $P_{seizure} + P_{up} < P_{normal}$  then
23:      next  $State \leftarrow Negative$ 
24:       $Result_n \leftarrow Normal$ 
25:       $Result_{n-2} \leftarrow Normal$ 
26:    else
27:      next  $State \leftarrow Positive$ 
28:       $Result_n \leftarrow Positive$ 
29:       $Result_{n-1} \leftarrow Positive$ 
30:    end if
31:  end if
32: end while

```

ALGORITHM 1. Algorithm for state machine post-processor

TABLE 2: Number of sessions for classes in TUSZ v1.5.0.

Class	Train set	Test set
Background	5313	1597
Focal nonspecific seizure	1015	283
Generalized nonspecific seizure	342	175
Complex partial seizure	147	59
Tonic seizure	18	51
Simple partial seizure	49	3
Tonic clonic seizure	37	21
Absence seizure	50	49

of 0.005. The Adam method combines the advantages of AdaGrad [46] and RMSprop [47], and it automatically adjusts the learning rate during training to accelerate the convergence of the model. The learning rate is adjusted according to TPR result between the default value 0.001 [43] and 0.0005, which is a similar technique reported in [14]. Similarly, the weight decay is adjusted from the default value 0 to 0.005 which is a similar technique reported in [17] to achieve better performance. We use default settings given

TABLE 3: Number of 5-second windows in the experiment.

	Negative	Positive
Train set	71674	15542
Test set	26058	6217

TABLE 4: Classifier performance on TUSZ.

Classifier	Sensitivity	Specificity	TPR
5 sec window origin dataset	45.69%	76.06%	23.11%
1 sec window origin dataset	35.86%	83.25%	28.59%
5 sec window 5-fold	77.23%	83.41%	37.78%
1 sec window 5-fold	79.10%	81.38%	34.61%
5 sec window with +1 conv layers	76.28%	80.91%	34.90%
5 sec window with +2 conv layers	77.82%	81.33%	34.35%
5 sec window without SMOTE	67.89%	82.45%	33.49%
5 sec window double banana montage	70.98%	73.17%	33.34%

by Pytorch for other parameters (e.g.,  $\beta_1$  and  $\beta_2$ ) as these parameters have a negligible effect on the learning speed or the accuracy based on our experimental trials.

The synthetic minority oversampling technique (SMOTE) [48] is adopted to deal with the imbalanced dataset problem between positive and negative classes. SMOTE generates samples in a minority class by calculating an interpolation between a randomly selected minority class sample and one of its  $k$ -nearest minority class neighbors. With a batch size of 64, 56 samples were taken from the dataset and eight minor class samples were generated. This method decreases the ratio between negative and positive samples from 2.25 to 1.6.

Each classifier in our experiment undergoes 180 epochs during the training. The performance comparison between different classifiers is shown in Table 4. TUSZ provides an original segmentation of the training and validation datasets. We shuffled the dataset to create a random dataset for  $k$ -fold evaluation. The results based on the original dataset and  $k$ -fold evaluation were both examined, and  $k$  was chosen to be 5 so that the number of samples in the training phase and the validation phase is similar to the original dataset. The result of the  $k$ -fold evaluation is remarkably better than the result of the original dataset on Sen and TPR. This phenomenon can be explained through the  $k$ -fold dataset is shuffled to balance the proportion of different classes of epileptic events in the training and validation sets, which improve the intrinsic performance of the dataset. Thus, the rest of the results discussed in the paper were all obtained with  $k$ -fold evaluation.

The best overall result was obtained by the 5-second window classifier with the SMOTE technique, whose performance versus epoch is shown in Figure 8. The sensitivity of the 5-second window classifier without SMOTE will drop by 9% with similar specificity performance. Deeper models based on DWT-Net were constructed by increasing the number of convolution layers by 1 to 2 in the network after the



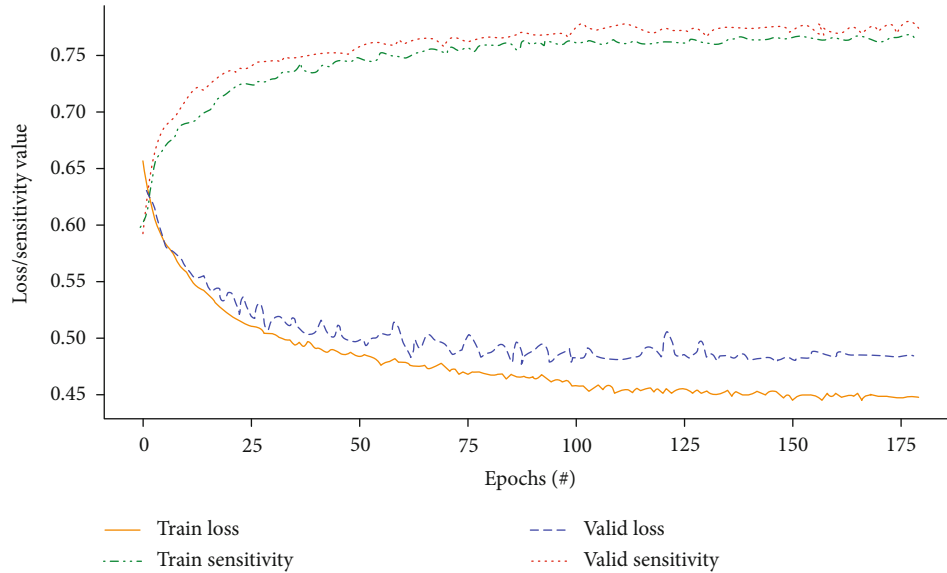


FIGURE 8: The loss and sensitivity values during training and validation of our proposed 5-second-window DWT-Net classifier.

TABLE 5: Results of the proposed seizure detection system in comparison with results reported in other work.

	System/ $p$ value	Sensitivity	Specificity	FAR
Deep learning methods in [14]	HMM	30.32%	80.07%	244
	HMM/SdA	35.35%	73.35%	77
	HMM/LSTM	30.05%	80.53%	60
	IPCA/LSTM	32.97%	77.57%	73
	CNN/MLP	39.09%	76.84%	77
	CNN/LSTM	30.83%	96.86%	7
	$p = 80\%$	25.44%	97.05%	3
Our DWT-Net system based on 5-second DWT-Net	$p = 76\%$	30.25%	96.64%	4
	$p = 70\%$	33.45%	96.10%	5
	$p = 60\%$	42.35%	94.93%	6
	$p = 35\%$	59.07%	89.72%	12
	$p = 90\%$	19.40%	95.01%	6
Our DWT-Net system based on 1-second DWT-Net	$p = 83.2\%$	30.07%	93.83%	7
	$p = 80\%$	33.45%	96.10%	5
	$p = 70\%$	42.35%	94.93%	6
	$p = 62.6\%$	49.29%	72%	12

inception layers of the multiple feature extractor. According to the experimental results shown in Table 4, the additional convolution layers cannot provide any improvement in the classifier's performance. It can be concluded that our proposed model can effectively learn features from the input and thus reduce the complicity of a neural network model.

The classifier's ability to learn spatial information from our proposed montage is tested by another trial using the double banana montage. The TPR result without our proposed montage drops by 4.4%. Hence, with the combined techniques (our proposed montage and the classifier), we can improve the Sen of the classifier by 16%.

**4.3. Evaluation of Seizure Detection System.** An epileptic event is defined when the average seizure density function value over its duration is higher than the threshold  $p$ . This output is compared with labeled ground truth for the calculation of Sen and FAR. The results based on 1-second and 5-second detection windows are shown in Table 5. Different values of the threshold  $p$  were examined to characterize the system. Given the same  $p$ , the performance of the system based on the 5-second window classifier performs better than 1-second system by an average increase of 7% in sensitivity. The specificity of the 1-second system drops sharply when the threshold decreases, while the 5-second system still holds

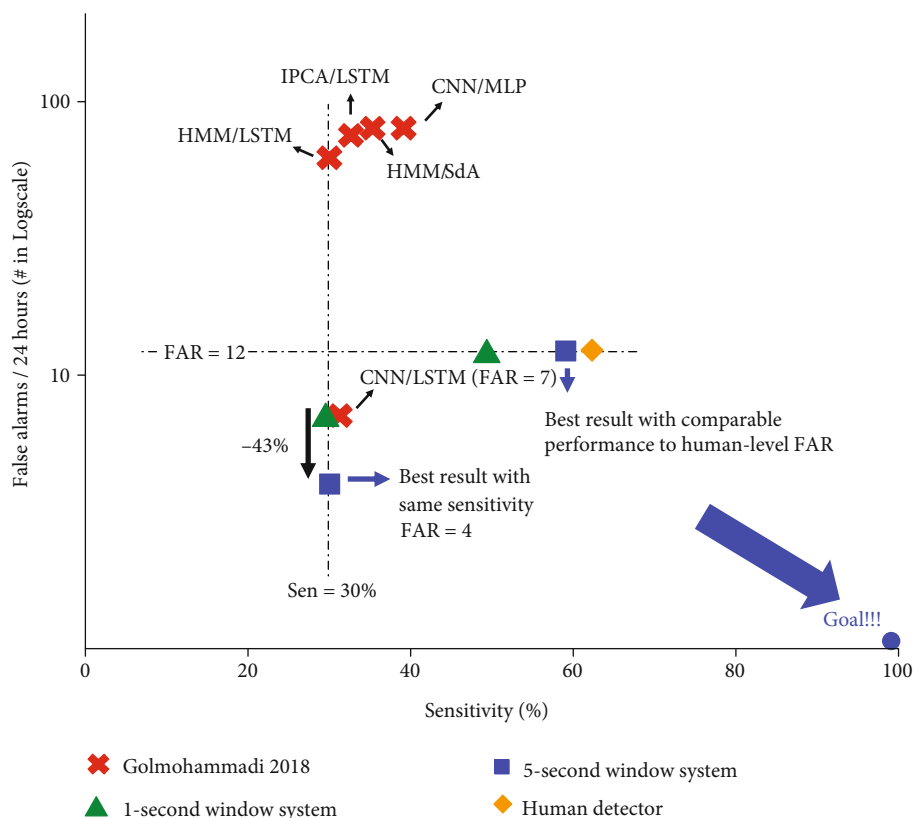


FIGURE 9: FAR versus Sen. Our system based on 5-second DWT-Net classifier achieves the best FAR of 4/24 hours with the sensitivity level of 30%, exceeding the CNN/LSTM model by a 43% decrease in FAR. The method also approaches average human-level detector based on the qEEG tool with a Sen of 59.07% at FAR of 12/24 hours.

a specificity of 89.72% with a 0.35 threshold. We conclude that our model can obtain better features from a 5-second window classifier, whose input wavelet coefficients represent more information at the lower frequency band of 2 to 32 Hz. This result agrees with clinical knowledge that the representative frequency band of seizure is below 30 Hz, proving the model's ability to learn meaningful representative features of EEG signals with the proposed method.

Comparing with the state-of-the-art works [14], we have provided a figure of FAR versus sensitivity in Figure 9 to illustrate the advantage of our proposed system. The system based on 5-second DWT-Net classifier achieves the best FAR of 4/24 hours with the same sensitivity level of 30.25%, exceeding the CNN/LSTM model by 43% decrease in FAR. It is reported by [19] that for similar tasks, the average human performance based on qEEG tools is within the range of 65% sensitivity with a FAR of 12 per 24 hours. To compare the system with human performance, the FAR is fixed to 12/24 hours by adjusting the density threshold  $p$ , and our system can detect seizure events with a sensitivity of 59.07%. The proposed system is almost reaching the performance of an expert clinician with a diagnostic tool.

## 5. Conclusion

In this work, the cooperative design of a multiple feature extractor CNN structure with wavelet coefficient packages

as input is derived from the proposed EEG montage. We introduced a system for automatic real-time detection of epileptic EEG events. Multiple feature extractors are used in our proposed DWT-Net to guide the feature extraction behavior of the model and improve its ability to incept local temporal and spatial features. A sensitivity of 59% is obtained with a FAR of 12/24 hours. While the system improves the state-of-the-art result of the automatic seizure detector to nearly a human level, it does not require an additional computation cost or more neural network layers. Our proposed method achieves similar performance compared to the human-level detector with qEEG tools. In practice, however, the combination of qEEG tools and raw EEG used by neurologists provides better accuracy. Our system can be more robust with additional verification done by the neurologists.

## Data Availability

The data used to support the findings of this study are included within the article.

## Conflicts of Interest

The authors declare that we have no financial or personal relationship with other people or organizations that could inappropriately influence or bias the content of this paper.



## Acknowledgments

This research is supported in part by the National Key Research and Development Program of China under Grant No. 2019YFB2204500 and in part by the National Science Foundation of China under Grant No. 61874171 and in part by the Science, Technology and Innovation Action Plan of Shanghai Municipality, China, under Grant No. 1914220370.

## References

- [1] D. L. Schomer and F. H. Lopes da Silva, *Niedermeyer's Electroencephalography: Basic Principles, Clinical Applications, and Related Fields*, Oxford University Press, Oxford, UK, 2017.
- [2] S. López, G. Suarez, D. Jungreis, I. Obeid, and J. Picone, "Automated identification of abnormal adult EEGs," in *2015 IEEE Signal Processing in Medicine and Biology Symposium (SPMB)*, Philadelphia, PA, USA, December 2015.
- [3] A. H. Shoeb, "Application of machine learning to epileptic seizure onset detection and treatment," PhD thesis, Massachusetts Institute of Technology, 2010.
- [4] M. Sharma, R. B. Pachori, and U. Rajendra Acharya, "A new approach to characterize epileptic seizures using analytic time-frequency flexible wavelet transform and fractal dimension," *Pattern Recognition Letters*, vol. 94, pp. 172–179, 2017.
- [5] U. R. Acharya, S. V. Sree, P. C. A. Ang, R. Yanti, and J. S. Suri, "Application of non-linear and wavelet based features for the automated identification of epileptic EEG signals," *International Journal of Neural Systems*, vol. 22, no. 2, article 1250002, 2012.
- [6] S. B. Wilson, M. L. Scheuer, C. Plummer, B. Young, and S. Pacia, "Seizure detection: correlation of human experts," *Clinical Neurophysiology*, vol. 114, no. 11, pp. 2156–2164, 2003.
- [7] A. Rizal and S. Hadiyoso, "Sample entropy on multidistance signal level difference for epileptic EEG classification," *The Scientific World Journal*, vol. 2018, Article ID 8463256, 6 pages, 2018.
- [8] S. Ghosh-Dastidar and H. Adeli, "Improved spiking neural networks for EEG classification and epilepsy and seizure detection," *Integrated Computer-Aided Engineering*, vol. 14, no. 3, pp. 187–212, 2007.
- [9] M. D. K. Hasan, M. A. Ahamed, M. Ahmad, and M. A. Rashid, "Prediction of Epileptic Seizure by Analysing Time Series EEG Signal Using -NN Classifier," *Applied Bionics and Biomechanics*, vol. 2017, Article ID 6848014, 12 pages, 2017.
- [10] Y. Cao, Y. Guo, H. Yu, and X. Yu, "Epileptic seizure auto-detection using deep learning method," in *2017 4th International Conference on Systems and Informatics (ICSAI)*, Hangzhou, China, November 2017.
- [11] Y. Li, W. Cui, M. Luo, K. Li, and L. Wang, "Epileptic seizure detection based on time-frequency images of EEG signals using Gaussian mixture model and gray level co-occurrence matrix features," *International Journal of Neural Systems*, vol. 28, no. 7, article 1850003, 2018.
- [12] M. Eberlein, R. Hildebrand, R. Tetzlaff et al., "Convolutional neural networks for epileptic seizure prediction," in *IEEE International Conference on Bioinformatics and Biomedicine*, Madrid, Spain, December 2018.
- [13] M. Golmohammadi, S. Ziyabari, V. Shah et al., "Gated recurrent networks for seizure detection," in *Signal Processing in Medicine and Biology Symposium*, Philadelphia, PA, USA, December 2017.
- [14] M. Golmohammadi, S. Ziyabari, V. Shah, S. L. de Diego, I. Obeid, and J. Picone, "Deep architectures for automated seizure detection in scalp EEGs," in *International Conference on Machine Learning*, Stockholm, Sweden, July 2017.
- [15] R. San-Segundo, M. Gil-Martín, L. F. D'Haro-Enríquez, and J. M. Pardo, "Classification of epileptic eeg recordings using signal transforms and convolutional neural networks," *Computers in Biology and Medicine*, vol. 109, no. 6, pp. 148–158, 2019.
- [16] K. M. Tsiouris, V. C. Pezoulas, M. Zervakis, S. Konitsiotis, D. D. Koutsouris, and D. I. Fotiadis, "A long short-term memory deep learning network for the prediction of epileptic seizures using EEG signals," *Computers in Biology and Medicine*, vol. 99, pp. 24–37, 2018.
- [17] S. Roy, I. Kiral-Kornek, and S. Harrer, "ChronoNet: a deep recurrent neural network for abnormal EEG identification," *Artificial Intelligence in Medicine*, vol. 11526, pp. 47–56, 2019.
- [18] V. Shah, E. von Weltin, S. Lopez et al., "The temple university hospital seizure detection corpus," *Frontiers in Neuroinformatics*, vol. 12, p. 83, 2018.
- [19] C. B. Swisher, C. R. White, B. E. Mace et al., "Diagnostic accuracy of electrographic seizure detection by neurophysiologists and non-neurophysiologists in the adult ICU using a panel of quantitative EEG trends," *Journal of Clinical Neurophysiology*, vol. 32, no. 4, pp. 324–330, 2015.
- [20] F. Carpi and D. De Rossi, "Non invasive brain-machine interfaces," *Ariadna Final Report*, vol. 31, pp. 1–30, 2006.
- [21] R. W. Homan, J. Herman, and P. Purdy, "Localisation cerebrale des electrodes places selon le systeme international 10-20," *Electroencephalography and Clinical Neurophysiology*, vol. 66, no. 4, pp. 376–382, 1987.
- [22] "How do reference montage and electrodes setup affect the measured scalp eeg potentials?," *Journal of Neural Engineering*, vol. 15, no. 2, article 026013, 2018.
- [23] M. Sazgar and M. G. Young, "Overview of EEG, electrode placement, and montages," in *Absolute Epilepsy and EEG Rotation Review*, pp. 117–125, Springer International Publishing, 2019.
- [24] R. G. Andrzejak, K. Lehnertz, F. Mormann, C. Rieke, P. David, and C. E. Elger, "Indications of nonlinear deterministic and finite-dimensional structures in time series of brain electrical activity: dependence on recording region and brain state," *Physical Review E*, vol. 64, no. 6, article 061907, 2001.
- [25] S. Ghosh-Dastidar, H. Adeli, and N. Dadmehr, "Mixed-band wavelet-chaos-neural network methodology for epilepsy and epileptic seizure detection," *IEEE Transactions on Biomedical Engineering*, vol. 54, no. 9, pp. 1545–1551, 2007.
- [26] A. L. Goldberger, L. A. Amaral, L. Glass et al., "PhysioBank, PhysioToolkit, and PhysioNet: components of a new research resource for complex physiologic signals," *Circulation*, vol. 101, no. 23, pp. E215–E220, 2000.
- [27] P. Thodoroff, J. Pineau, and A. Lim, "Learning robust features using deep learning for automatic seizure detection," in *Proceedings of the 1st Machine Learning for Healthcare Conference*, Los Angeles, CA, USA, August 2016.
- [28] A. Bhattacharyya and R. B. Pachori, "A multivariate approach for patient specific EEG seizure detection using empirical wavelet transform," *IEEE Transactions on Biomedical Engineering*, vol. 64, no. 9, pp. 2003–2015, 2017.

- [29] A. Harati, S. López, I. Obeid, J. Picone, M. Jacobson, and S. Tobochnik, "The TUH EEG CORPUS: a big data resource for automated EEG interpretation," in *2014 IEEE Signal Processing in Medicine and Biology Symposium (SPMB)*, Philadelphia, PA, USA, December 2014.
- [30] I. R. D. Saputro, N. D. Maryati, S. R. Solihati, I. Wijayanto, S. Hadiyoso, and R. Patmasari, "Seizure type classification on EEG signal using support vector machine," *Journal of Physics: Conference Series*, vol. 1201, article 012065, 2019.
- [31] S. Roy, U. Asif, J. Tang, and S. Harrer, "Machine learning for seizure type classification: setting the benchmark," 2019, <https://arxiv.org/abs/1902.01012>.
- [32] M. Golmohammadi, A. H. Harati Nejad Torbati, S. Lopez de Diego, I. Obeid, and J. Picone, "Automatic analysis of EEGs using big data and hybrid deep learning architectures," *Frontiers in Human Neuroscience*, vol. 13, no. 3, p. 76, 2019.
- [33] S. López, A. Gross, S. Yang, M. Golmohammadi, I. Obeid, and J. Picone, "An analysis of two common reference points for EEGs," in *2016 IEEE Signal Processing in Medicine and Biology Symposium (SPMB)*, Philadelphia, PA, USA, December 2016.
- [34] J. Duun-Henriksen, T. W. Kjaer, R. E. Madsen, L. S. Remvig, C. E. Thomsen, and H. B. D. Sorensen, "Channel selection for automatic seizure detection," *Clinical Neurophysiology*, vol. 123, no. 1, pp. 84–92, 2012.
- [35] M. Qaraqe, M. Ismail, and E. Serpedin, "Band-sensitive seizure onset detection via CSP-enhanced EEG features," *Epilepsy & Behavior: E&B*, vol. 50, no. 7, pp. 77–87, 2015.
- [36] J. N. Acharya, A. J. Hani, P. Thirumala, and T. N. Tsuchida, "American clinical neurophysiology society guideline 3: a proposal for standard montages to be used in clinical EEG," *The Neurodiagnostic Journal*, vol. 56, no. 4, pp. 253–260, 2017.
- [37] D. Hagemann, E. Naumann, and J. F. Thayer, "The quest for the EEG reference revisited: a glance from brain asymmetry research," *Psychophysiology*, vol. 38, no. 5, pp. 847–857, 2010.
- [38] U. R. Acharya, H. Fujita, S. L. Oh et al., "Deep convolutional neural network for the automated diagnosis of congestive heart failure using ecg signals," *Applied Intelligence*, vol. 49, no. 1, pp. 16–27, 2019.
- [39] A. Teolis, *Discrete wavelet transform*, Birkhäuser, Boston, 1998.
- [40] M. Zhao, M. Kang, B. Tang, and M. Pecht, "Multiple wavelet coefficients fusion in deep residual networks for fault diagnosis," *IEEE Transactions on Industrial Electronics*, vol. 66, no. 6, pp. 4696–4706, 2019.
- [41] N. Rafiuddin, Y. Khan, and O. Farooq, "Feature extraction and classification of EEG for automatic seizure detection," in *2011 International Conference on Multimedia, Signal Processing and Communication Technologies*, Aligarh, India, December 2011.
- [42] T.-Y. Lin, A. R. Chowdhury, and S. Maji, "Bilinear CNN models for fine-grained visual recognition," in *2015 IEEE International Conference on Computer Vision (ICCV)*, Santiago, Chile, December 2015.
- [43] A. Paszke, S. Gross, S. Chintala et al., "Automatic differentiation in PyTorch," in *IEEE Conference on Neural Information Processing Systems*, Long Beach, USA, December 2017.
- [44] K. He, X. Zhang, S. Ren, and J. Sun, "Delving deep into rectifiers: surpassing human-level performance on ImageNet classification," in *2015 IEEE International Conference on Computer Vision (ICCV)*, Santiago, Chile, December 2015.
- [45] D. Kingma and J. Ba, "Adam: a method for stochastic optimization," in *International Conference on Learning Representations*, San Diego, CA, USA, May 2015.
- [46] J. Duchi, E. Hazan, and Y. Singer, "Adaptive subgradient methods for online learning and stochastic optimization," *Journal of Machine Learning Research*, vol. 12, no. 7, pp. 257–269, 2011.
- [47] L. Bottou and Y. LeCun, "Large scale online learning," in *Advances in Neural Information Processing Systems 16 (NIPS 2003)*, pp. 217–225, MIT Press, Cambridge, MA, 2004.
- [48] N. V. Chawla, K. W. Bowyer, L. O. Hall, and W. P. Kegelmeyer, "SMOTE: synthetic minority over-sampling technique," *Journal of Artificial Intelligence Research*, vol. 16, pp. 321–357, 2002.

## Research Article

# A Multichannel fNIRS System for Prefrontal Mental Task Classification with Dual-level Excitation and Deep Forest Algorithm

**Cheng Chen, Yizhen Wen, Shaoyang Cui, Xiangao Qi, Zhenhong Liu, Linfeng Zhou, Mingyi Chen, Jian Zhao , and Guoxing Wang**

*Department of Micro/Nano Electronics, Shanghai Jiao Tong University, Shanghai 200240, China*

Correspondence should be addressed to Jian Zhao; [zhaojianycc@sjtu.edu.cn](mailto:zhaojianycc@sjtu.edu.cn)

Received 14 December 2019; Revised 28 April 2020; Accepted 5 May 2020; Published 12 June 2020

Academic Editor: Hassan Mostafa

Copyright © 2020 Cheng Chen et al. This is an open access article distributed under the Creative Commons Attribution License, which permits unrestricted use, distribution, and reproduction in any medium, provided the original work is properly cited.

This paper presents a multichannel functional continuous-wave near-infrared spectroscopy (fNIRS) system, which collects data under a dual-level light intensity mode to optimize SNR for channels with multiple source-detector separations. This system is applied to classify different cortical activation states of the prefrontal cortex (PFC). Mental arithmetic, digit span, semantic task, and rest state were selected as four mental tasks. A deep forest algorithm is employed to achieve high classification accuracy. By employing multigrained scanning to fNIRS data, this system can extract the structural features and result in higher performance. The proposed system with proper optimization can achieve 86.9% accuracy on the self-built dataset, which is the highest result compared to the existing systems.

## 1. Introduction

Brain monitoring has been applied to study human brain activity and explore the brain-computer interfaces in recent years. There are many different types of noninvasive brain activity monitoring methods. Traditional techniques such as functional magnetic resonance imaging (fMRI) and positron emission tomography (PET) are expensive and unsuitable for continuous daily brain monitoring. Therefore, some portable and wearable neuroimaging techniques became more popular choices, especially the functional near-infrared spectroscopy (fNIRS).

fNIRS is an optical technique based on the attenuation of near-infrared light that enables us to monitor hemodynamic and metabolic changes during cortical activation [1]. As a noninvasive technique with a balanced spatial-temporal resolution, fNIRS has drawn increasing attention as a powerful alternative or supplement to traditional neuroimaging techniques over the past years [2]. According to measuring changes in the concentrations of tissue chromophores,

mainly oxy- and deoxyhemoglobin, fNIRS can be applied to assess functional brain activities in different mental tasks.

Since the brain-computer interface (BCI) technology paves a new way to interact with machines through brain activity, it draws increased research efforts. As a result, novel fNIRS and hybrid fNIRS-EEG systems have been proposed to develop BCI applications with novel analysis algorithms and signal processing techniques [3–7].

A very attractive brain region for BCI application is the prefrontal cortex (PFC), which provides high-quality signals without the interference of the hair and becomes a suitable and popular measurement region in fNIRS. It is known that the PFC is involved in various executive functions, working memory, and semantic tasks [8].

Nowadays, there are many commercial fNIRS equipment in the market for researchers. Most of them provide excellent performance on brain activation detection. But all of these systems are either very complex not suitable for portability or very expensive not suitable for larger scale research study. To implement an fNIRS system for collecting data in the

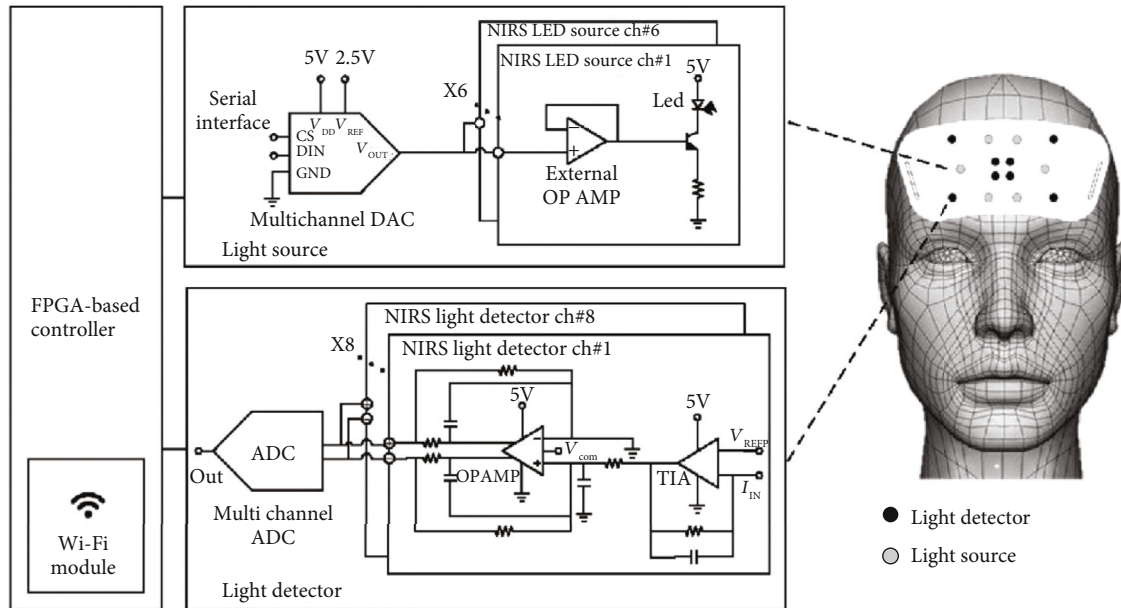


FIGURE 1: Overall system diagram of proposed NIRS system.

PFC, there are several light-emitting diode (LED) sources and detectors located on the brain region of interest to obtain optical channels. In previous studies, some systems use a single source-detector separation distance [9–12], and some systems use multiple source-detector separation distances [13, 14]. Since detected light intensity varies considerably not only with source-detector separation distance but also with light intensity emitted by light source and tissue optical characteristics, it is necessary to do a careful channel by channel calibration to improve the signal quality for channels with different source-detector separation distances, which means the outputs of all detectors have high signal-to-noise ratio (SNR) rather than saturation.

Calibration should be supported by a hardware which is usually expensive. There are two ways to do the traditional self-adaptive calibration. One is adjusting the emitted source light intensity to enable the detected light intensity achieving the input range of the detect circuit. The other way is adjusting the light detection gain, sensitivity of the light sensor, and related front-end circuit to make the output signal in a proper range of an analog-digital converter (ADC). Besides the complicity of the fNIRS hardware, the adaptive procedure for calibration in software is also complicated, especially for multiple source-detector separation layout configuration which is more flexible for specific brain monitors. What is more, the complicated fNIRS system's size and weight could not be that compact for wearable applications, and its expensive price also limits the large-scale use of fNIRS.

Building a robust model to classify trial data is also essential to the fNIRS-BCI system. Previous studies also verify the feasibility of classifying several mental tasks in the PFC (e.g., mental arithmetic). So far, there are lots of binary classification models and some of them can achieve high accuracy, even on a single trial [4, 6, 7]. However, the multiclass classification of mental tasks in the PFC has not been well studied yet. Different cortical activities show spatial differ-

ences in NIRS patterns, so using a multitask classification algorithm based on the multichannel system is promising for more applications in fNIRS-BCI.

Taking the above concerns into consideration, this paper proposes a dual-level light intensity method to provide more useful channels and decrease the requirement of hardware, which makes our fNIRS system more suitable for portability, as it relaxes the need to calibrate the signal channel by channel. Then, we conduct four different mental tasks to activate PFC with our multichannel NIRS system and then employ a deep forest algorithm to classify four cortical activation states. This paper also compares the performances when taking different chromophore concentrations as features and concludes the optimal parameters in feature extraction and model adjustment to achieve high accuracy.

## 2. System Design and Experimental Paradigm

**2.1. The Hardware of fNIRS System.** The overall system block diagram is shown in Figure 1. The proposed system consists of a 6-channel light source module, an 8-channel photodiode (PD) light detector module, and a field programmable gate array- (FPGA-) based controller with a built-in Wi-Fi module. Light source probes and light detector probes are placed on the forehead for light emitting and collecting, respectively.

In the consideration of measured signal sensitivity and the optional light sources in the commercial market, the 735 and 850 nm wavelengths have been selected in the system [15]. The 6-channel light source module consists of 6 double wavelength optical sources (two LEDs in one package, 735 nm and 850 nm, Ushio) and its driving circuit which utilizes a voltage buffer and a triode-based voltage-current converter to convert the output of digital-to-analog converters (DAC, AD5542A) to the corresponding LED driving current without affecting the function of the DAC. In order to implement the system with high adaptability of various



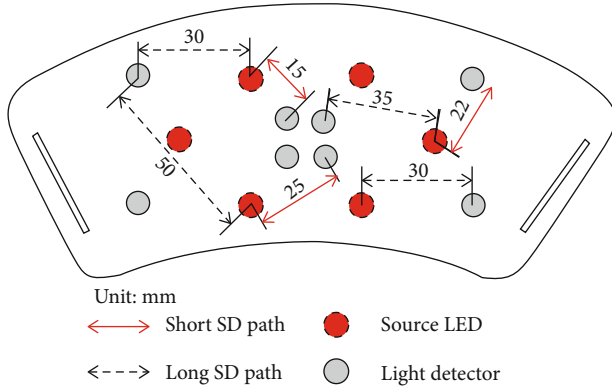


FIGURE 2: The layout of sources and detectors.

experiments and subjects, each wavelength light intensity could be adjusted from 0 mA to 50 mA with a  $0.78 \mu\text{A}$  step. The light-emitting intensity should be carefully chosen to realize a better final signal during testing based on different experiment conditions.

The light-receiving circuit generally magnifies the  $\mu\text{A}$ -level current detected by a photodiode and digitizes the amplified signal for the convenience of following data transmission and signal processing. The amplification circuit has two stages. The first stage is a transimpedance amplifier with a gain of 5000. The second stage is an active low-pass filter with a 100 kHz cutoff frequency of antialiasing, followed by a 24-bit ADC.

The controller maintains the sequences of light driving and receiving with the multithread capability of FPGA (ZYNQ7000) and encodes data received from the ADC for channel identification and data compression. The wireless communication between the system and the terminal device is implemented by the embedded transceiver in TI CC3220SF SoC for further data processing and classification.

Under the coordination of the controller, there are 48 channels working in time-division multiple access (TDMA) modulation at the switching rate of 43.8 Hz, by emitting each light source and each wavelength LED one by one at a certain intensity. A flexible probe distribution plate is designed to hold the light source and light detector probes. The layout pattern of the light source and light detector probes placed on the forehead could be custom based on the requirement of a special experiment to locate the observation points on the relative cortex region. A layout used in our BCI task classification experiment with multiple source and detector separations is shown in Figure 2.

**2.2. Data Acquisition with Dual-Level Light Intensity.** Due to the light highly scattering characteristic in the brain tissue, photons emitted by the light source will be scattered and reflected in the propagation path in the tissue, and some of the photons will be reflected out of the brain and detected by detectors. The light diffuse reflection transmission path formed by the detected photons in the brain tissue between the source and detector is banana-like shaped. And the light coming out from the brain is attenuated as the light is partly absorbed by the chromophores along the path [16, 17]. The

fNIRS system measures the light intensity through the human tissue to obtain the light attenuation change, so as to measure the concentration changes of oxyhemoglobin ( $\text{HbO}_2$ ) and deoxyhemoglobin (Hb) based on the differential form of the modified Beer-Lambert Law (dMBLL) [18–20]:

$$\Delta A = \ln \frac{I_{\text{det},2}}{I_{\text{det},1}} = L \Delta \mu_a, \quad (1)$$

where  $\Delta A$  is the change of light attenuation,  $I_{\text{det}}$  means the detected intensity values of two different states of the tissue,  $L$  is the total mean path length of detected photons, and  $\mu_a$  is the absorption coefficient of the tissue.

For different kinds of tissues, the path length  $L$  is related to the differential path length factor (DPF) and the source-detector separation distance  $d$ :

$$L = \text{DPF} \cdot d \quad (2)$$

The value of the DPF could be obtained through experiments or Monte Carlo simulations under different conditions [21, 22]. In this work, we use 5.98 and 6.5 for 735 nm and 850 nm wavelength, respectively.

From Equation (1), we know that the attenuation change is proportional to the change of absorption, which is the weighted sum of the change in the concentration of  $\text{HbO}_2$  and Hb:

$$\Delta \mu_a = \alpha_{\text{HbO}_2} \Delta c_{\text{HbO}_2} + \alpha_{\text{Hb}} \Delta c_{\text{Hb}}, \quad (3)$$

where the  $\alpha$  weights are the absorption coefficients of different chromophores. If the attenuation change is measured at two wavelengths, the concentration changes can be calculated from the detected intensity values [20]:

$$\begin{aligned} \Delta c_{\text{HbO}_2} &= \frac{\alpha_{\text{Hb}}^{\lambda_1} (\Delta A^{\lambda_2} / \text{DPF}^{\lambda_2} d) - \alpha_{\text{Hb}}^{\lambda_2} (\Delta A^{\lambda_1} / \text{DPF}^{\lambda_1} d)}{\alpha_{\text{Hb}}^{\lambda_1} \alpha_{\text{HbO}_2}^{\lambda_2} - \alpha_{\text{Hb}}^{\lambda_2} \alpha_{\text{HbO}_2}^{\lambda_1}}, \\ \Delta c_{\text{Hb}} &= \frac{\alpha_{\text{HbO}_2}^{\lambda_1} (\Delta A^{\lambda_2} / \text{DPF}^{\lambda_2} d) - \alpha_{\text{HbO}_2}^{\lambda_2} (\Delta A^{\lambda_1} / \text{DPF}^{\lambda_1} d)}{\alpha_{\text{HbO}_2}^{\lambda_1} \alpha_{\text{Hb}}^{\lambda_2} - \alpha_{\text{HbO}_2}^{\lambda_2} \alpha_{\text{Hb}}^{\lambda_1}}. \end{aligned} \quad (4)$$

Therefore, during the process of converting detected light attenuation to concentration changes of chromophores, the measurement for  $\Delta A$  is crucial to the accuracy of final results. As shown in Figure 3, the detected light intensity is related to the emitted light intensity of the source and the distance of source-detector separation. LED sources could work under two different intensity levels, and two identical photodiode detectors are marked as PD1 and PD2. The banana-like shapes show different spatial distributions of NIR lights in channels.

The total detected light intensity decreases when the interval of source-detector separation increases. However, the ratio of photons went through the white matter layer increases, which means a gain in sensitivity [23, 24]. Therefore, there is a trade-off between the detected light intensity

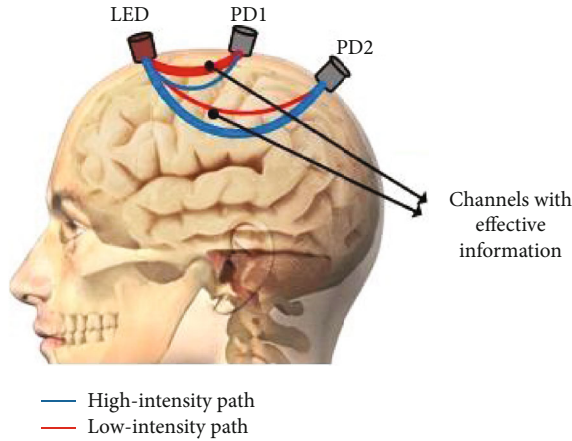


FIGURE 3: Comparison of the spatial distribution of NIR light in different channels.

and the useful information in fNIRS signal. As shown in Figure 3, if the emitted source light intensity is high, the intensity of signals in channels with a long separation distance of source-detector will be improved, but the detector of channels with a short distance might be saturated. On the contrary, if the emitted source light intensity is low, the quality of signals in the channels with a short distance of source-detector separation will be good, but the channels with a long distance might suffer from low achievable SNR. Although the SNR of some channels is not good under some conditions, it still contains effective information related to the mental state.

To achieve the optimal SNR for each channel, the light intensity of the LED source should be well chosen and be adjusted for each detector with different distances. As shown in Figure 2, there are different source-detector (SD) paths among all channels; it is obvious that single-level light intensity is unable to provide good SNR for long SD path and short SD path channels at the same time. If we calibrate light intensity for each channel and adjust the light intensity for each detector with different distances, 8 kinds of configurations will be used, and the temporal resolution will be decreased by 8 times. In order to solve the confliction between signal quality and temporal resolution, we propose a dual-level light intensity data acquisition method to balance it, as shown in Figure 4.

The single-level intensity mode is easy to realize. However, when the spaces and locations of source/detector pairs are limited, it is impossible to be adjusted properly for all measurement requirements and test objects. Since LED sources are driven by DAC, the controller in this system is able to adjust the light intensity. Therefore, the LED sources could be coded to work at different light intensity levels by software. Based on TDMA, each LED is switched on twice with high-level intensity (Lv.H) and low-level intensity (Lv.L), and all LEDs work in this mode and be switched on one by one. The switching scheme will affect the detection result, especially on the distortion between different channels. This is a common problem for time-division control method in fNIRS. If one switching cycle period (in our

system, the cycle period is  $1/43.8 \text{ Hz} = 0.023 \text{ sec}$ ) is much shorter than the response time of the brain activity hemoglobin signal (usually larger than 1 second), the effect could be ignored. And, in our system, as there is only one DAC, the light source can only be switched one by one. Each time we change the output of DAC to decide the level of light intensity, about five milliseconds later a stable output can be obtained because of the setup time of circuits. If we change the levels frequently, the total additional waiting time will become unacceptable. The number of level change in Figure 4 is one which costs the minimal additional time so as to provide the smallest distortion in final signals. In our system, we keep the light intensity exposure on the tissue much weaker than the requirement of safety standard (IEC62471).

The use of a dual-level light intensity method reduces the dependence on hardware and makes the system to be wearable. Moreover, for channels with multiple source-detector separations, there is always a better result for each channel under two levels. The calibration is to make every channel with good signal-to-noise ratio and no saturation. By using the dual-level light intensity method in a multiple separated source-detector configuration, the source-detector pair with a short separation distance will not be saturated under low-intensity emitted light, and for long separated source-detector pair, a low noise signal will be detected under high-intensity emitted light. The dual-level light intensity method expands the tolerance of source-detector separation and relaxes the need for a channel by channel calibration. By combining them together, we could maximize the number of effective channels in the limited area on the forehead. And dual-level mode sacrifices less temporal resolution than any other multilevel modes or channel by channel calibrations under multiple source-detector separations.

Finally, we use the designed fNIRS system with a custom layout pattern under dual-level light intensity mode to collect the PFC activity data during experiment. The complete output consists of 48 channels from all source-detector combination, and its preprocessing procedure is shown in Figure 5. After being applied to the dMBLL, the measured signals are then filtered by a fifth-order Butterworth filter with a passband of 0.01-1 Hz, which prepares the data for the following feature extraction.

**2.3. Experimental Paradigm.** The NIRS data were collected by our continuous-wave NIRS system with two wavelengths (735 nm and 850 nm). As shown in the right part of Figure 1, the multichannel system consists of eight detectors and six sources; all of them are attached to a special cap made of silicone, providing good coupling to the scalp. The subject needs to wear this cap during the experiment, and the setup is shown in Figure 6.

During the experiment, the subject was asked to sit in a chair and try to avoid head and body movements. Each trial comprised a 30-second prereset period to get the baseline, 5 repetitions of the given task, and a 30-second postreset period. Before each experiment, the instruction was displayed on the screen, and the subject needs to respond as quickly and as

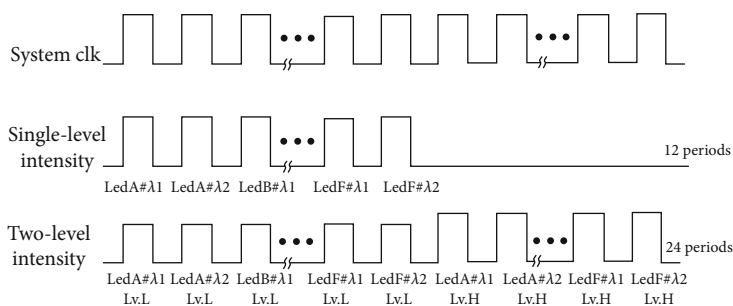


FIGURE 4: Comparison between single-level intensity and dual-level intensity.

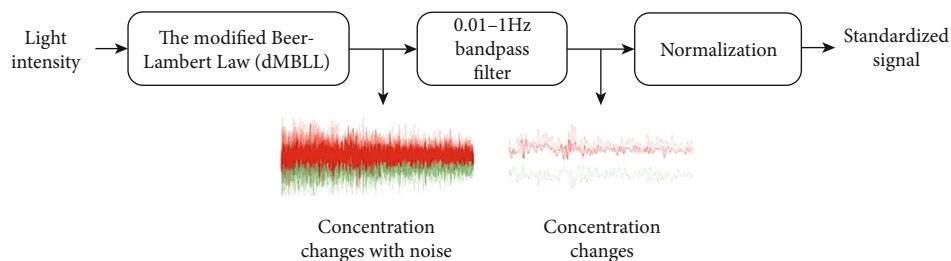


FIGURE 5: The procedure of data preprocessing.

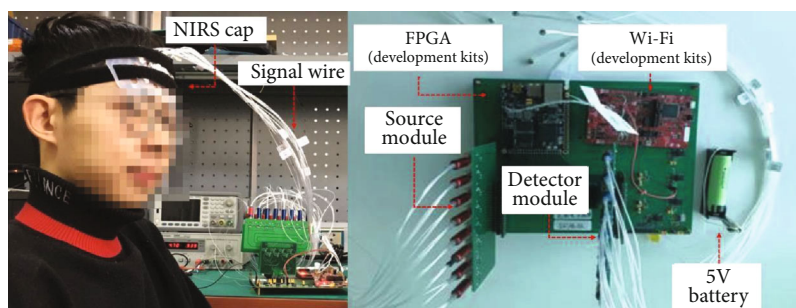


FIGURE 6: Experiment setup with the proposed system.

correctly as possible to the tasks. The experiment consists of three different tasks:

- (i) Mental arithmetic (MA) task: the subject needs to calculate the subtraction of a small prime number (such as 13, in this case) from a random three-digit number and continue to do the subtraction with successive subtractions until the task period is finished. During the MA task, only the first number is displayed on the screen.
- (ii) Digit Span (DS) task: when it begins, a random six-digit number is displayed on the screen digit by digit; each digit display lasts for 0.1 s with a 0.4 s interval. After displaying the entire number, the subject needs to recall the number in reverse order and then press the button to continue the next number display throughout the task period.
- (iii) Semantic (SM) task: two Chinese nouns randomly selected from the word database are displayed on the screen. The subject needs to use these two words to make a sentence and press the button to get the

next set of words to continue the same semantic task until the task is finished.

The experimental paradigm and an example of screen display are shown in Figure 7. All procedures are controlled by the software automatically to guarantee a standard paradigm, and the NIRS system collects data simultaneously.

### 3. Deep Forest for Mental Task Classification

Deep forest is a novel decision tree-based approach. By combining multigrained scanning with a cascaded random forest, deep forest is structurally aware and performs excellently even on small-scale data by automatically setting the model. Moreover, deep forest has fewer hyperparameters than traditional deep neural networks, and its performance is quite robust to hyperparameter settings [25]. Compared to a standard decision tree algorithm, the deep forest approach is better in a feature study as dimensionality reduction of raw data is unnecessary. Secondly, the results of deep forest are more accurate as the results are the decision of multiple classifications and regression trees. Besides, the deep forest approach



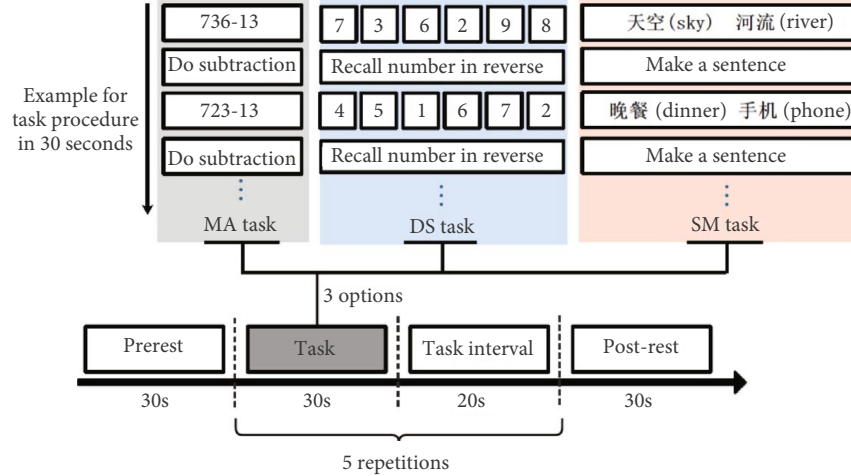


FIGURE 7: Sequence diagram of the experimental paradigm.

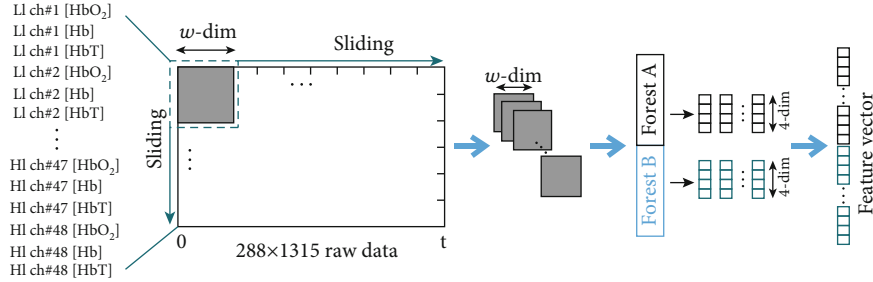


FIGURE 8: Illustration of feature reconstruction with scanning.

has the ability of parallel computing which makes it very effective.

As NIRS data are sampled at a high frequency with multiple channels, it will get high dimensions to deal with and have a strong spatial-temporal structure. For future real-time applications in the NIRS-BCI system, the classification algorithm should be as fast and efficient as possible. Since the running efficiency of deep forest is high and can be improved further with optimized parallel implementation [25], deep forest is a suitable and promising choice.

**3.1. Feature Extraction with Multigrained Scanning.** According to the experiment paradigm mentioned before, we need to select and extract the features from the raw NIRS data in advance. When selecting the concentration changes of HbO<sub>2</sub>, Hb, and HbT (a summation of HbO<sub>2</sub> and Hb) as features, there are 1315 raw features in each time sequence sampled in a 30-second task period under a frequency of 43.8 Hz. For a total of 48 channels with three variables, signals collected under low-level light intensity (LI) and high-level light intensity (HI) are concatenated into a  $288 \times 1315$  matrix as a raw instance of each task according to the given spatial locations.

Taking the spatial-temporal characteristics of NIRS data into account, we scan NIRS data in the style of processing images; thus, we can extract structural features without image

reconstruction of cortical activity. As shown in Figure 8, taking the dimensions of final feature vectors into account, the raw instance (with  $288 \times 1315$  raw features) is sliced by sliding a  $w$ -dimensional window with a step of  $s$ ; then,  $((288 - w)/s + 1)((1315 - w)/s + 1)$  new small instances will be produced, which belongs to the same task class as raw instance. If we slide the window one feature by one feature, which means the step is one, the number of new small instances is equal to  $(289 - w)(1316 - w)$  (e.g., if  $w = 288$ , sliding the window will produce 1028 small instances for each raw instance).

All instances extracted from the same size of windows will be used to train two different kinds of forest, a completely-random tree forest A and a random forest B. Since we have three tasks and a rest state, each class feature will be generated with 4 dimensions and then concatenated as transformed features. By using multiple sizes of sliding windows, different feature vectors will be generated and prepared for the following cascaded forest stage.

**3.2. Cascaded Random Forest.** Deep forest employs a cascaded structure, as illustrated in Figure 9, making each layer receive and pass feature information. Since we use multi-grained scanning, there will be several levels in each layer, and each level is an ensemble of forests based on decision trees. We use two completely random tree forests and two

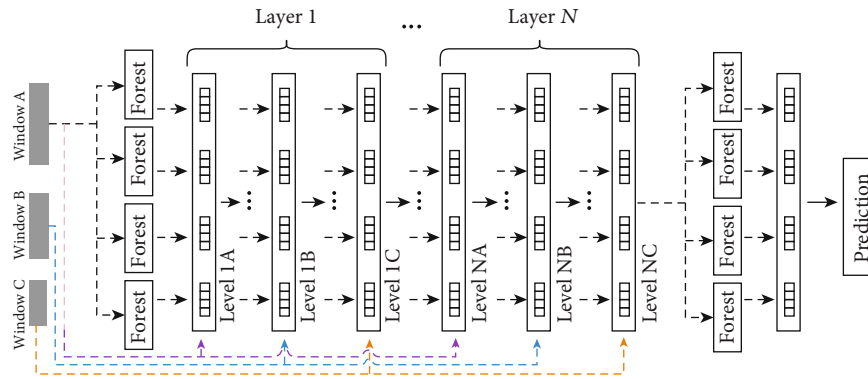


FIGURE 9: The procedure of cascaded forest.

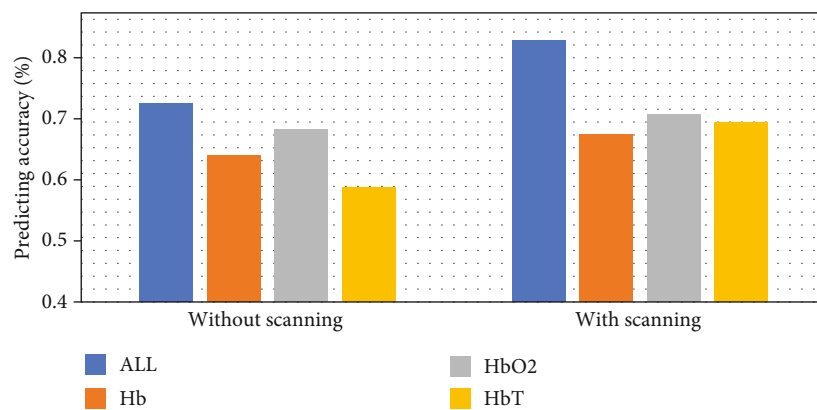


FIGURE 10: Mean accuracy of different chromophore feature selection.

random forests for each level, and each forest will produce an estimate of the class distribution.

After using three window sizes to conduct multigrained scanning, three feature vectors in different dimensions are produced, which will be used to train the three grades of the cascaded random forest correspondingly. For each instance, each tree will generate a distribution with the percentage of different classes that the training examples are divided into. By averaging across all trees in the same forest, each forest will produce the estimated result and form a 4-dimension class vector. Class vectors of all forests are then concatenated with the original feature vector of the corresponding level to be inputted to the next level of the cascade.

After increasing a new level, the performance of the whole cascade will be estimated on the validation set. This procedure will be repeated until the validation performance converges. If there is no performance gain, the training procedure will terminate automatically; then, the final prediction will be generated by pooling the results of the four random forests in the last layer.

#### 4. Experimental Results and Discussion

To verify the proposed system and test the performance of classifiers, we use a dataset collected by the experiments mentioned before from two average 23-year-old healthy men.

There are four classes labelled with MA, DS, SM, and REST, and each class has 48 instances.

In order to determine the optimal models, we firstly compared the performance of different kinds of chromophores for feature selection with and without scanning. The fNIRS signals of HbO<sub>2</sub> and Hb usually have a negative correlation relationship during mental tasks, and the change of HbO<sub>2</sub> is larger than Hb in actual cortical activation [26]. It is consistent with the result that only taking HbO<sub>2</sub> as a feature can achieve higher accuracy than Hb in Figure 10. This also explains the poor performance of only taking HbT as raw features, because it usually has the same tendency as HbO<sub>2</sub> but with a smaller change. However, when the blood flow change gives rise to similar trend changes in HbO<sub>2</sub> and Hb, HbT could be an important feature to reflect facts. It is obviously shown that taking the combination of all three kinds of concentrations has a better performance than taking any single kind of chromophores.

We then compared the performance of different light intensity levels. After scanning the raw feature with the window size ranging from 36 to 144, corresponding to 1/8 and 1/2 width, respectively, the results are shown in Figure 11. Different scanning window sizes show different data features from different time frequency domains. Some of them contain more useful information for classification. As a result, the classification accuracy varies with the

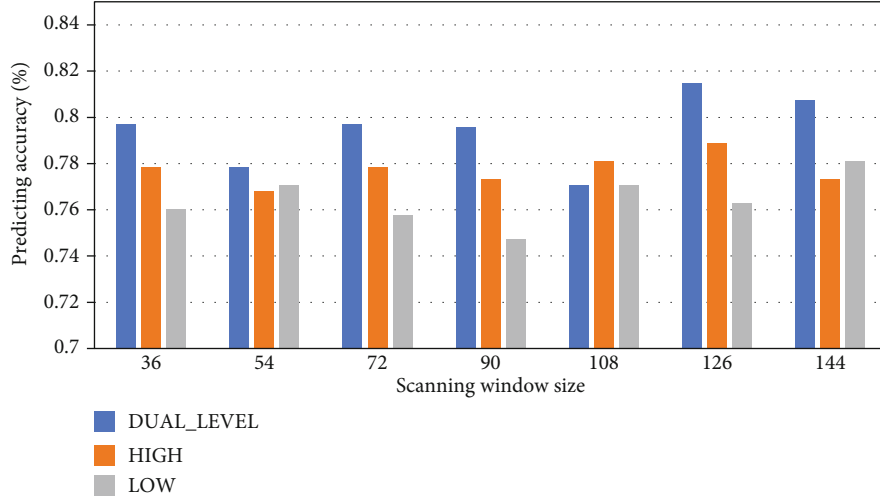


FIGURE 11: Mean accuracy of different light intensity level selection.

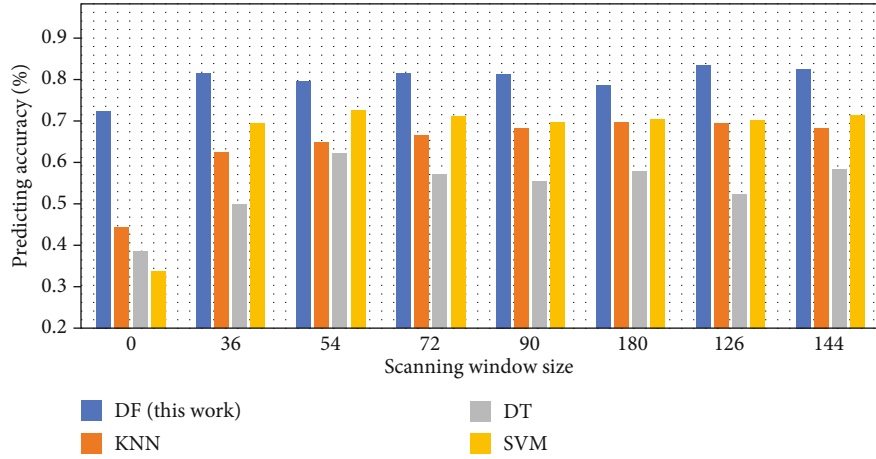


FIGURE 12: Mean accuracy of four methods with different window sizes.

scanning window size. Selecting data under dual-level light intensity shows higher mean accuracy than a single high-level or low-level intensity. This result is consistent with the fact that dual-level light intensity provides more channel information than single level under multiple source-detector separation distance layout configuration, relaxes the complexity of hardware, and also saves the temporal resolution by avoiding channel by channel calibration, which are the two important aspects for wearable BCI equipment.

The data collected by the dual-level light intensity method and all three kinds of chromophores were then selected to construct the features. To compare some traditional machine learning classifiers employing support vector machine (SVM), decision tree (DT), and k-nearest neighbours (KNN) with the deep forest (DF) classifier, we performed 4-fold cross-validation to evaluate the accuracy. As shown in Figure 12, all models and datasets were evaluated with different single-grained scanning sizes, and size 0 means no scanning for the raw features. It is vividly shown that the deep forest classifier has a better performance than other

TABLE 1: Parameters of the deep forest algorithm in this work.

Symbol	Value	Remark
W1	36	Size of the first scanning window
W2	90	Size of the second scanning window
W3	126	Size of the third scanning window
S	36	Size of the scanning step
N_cls	4	Number of fNIRS data classes
N_mf	30	Number of trees in multigrained scanning forests
N_cf	101	Number of trees in cascade forests
F	0.2	Split fraction for cascade training set splitting

classifiers, especially without scanning to reconstruct the raw features. Other classifiers also benefit a lot from the scanning process with forests, which shows an improvement of mean accuracy in Figure 12.

After a comparison among all these algorithms and sizes, we selected three window sizes with the best performance in

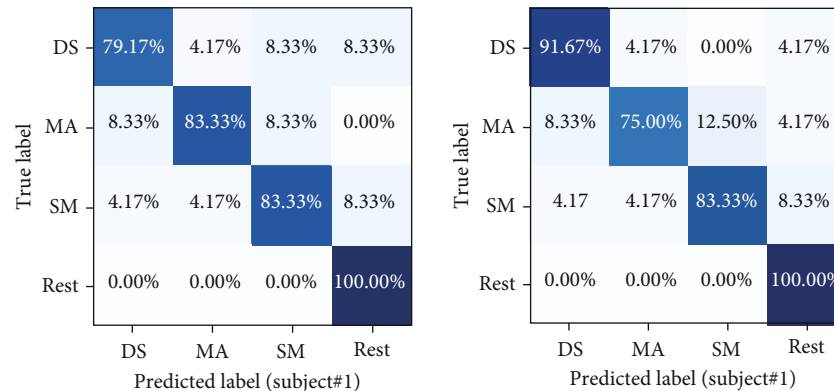


FIGURE 13: Confusion matrixes of two subjects.

TABLE 2: Comparison with fNIRS-based mental task classification.

Year/publication	2018 [3]	2015 [6]	2012 [7]	This work
# of detector/source	6/6	18/15	3/10	8/6
Sample rate	13.3 Hz	10 Hz	31.25 Hz	43.8 Hz
Wireless	Yes	No	No	Yes
Weight	Approx. 750 g	Approx. 130Kg	20 kg	450 g
Portability	Yes	No	No	Yes
# of intensity level	1	1	1	2
# of mental state	3	3	3	4
Classifier	sLDA	LDA	LDA	DF
Accuracy	64.1%	71.7%	62.5%	86.9%

different size ranges to do multigrained scanning. The values of hyperparameters in the deep forest algorithm are listed in Table 1.

After training with optimal hyperparameters, the generated model was used to predict the test sets and achieved an average accuracy of 86.95%, and the confusion matrixes of two subjects are shown in Figure 13.

The results indicate that the rest state is easy to be identified as the right label, but the MA task, DS task, and SM task might be predicted as the rest state by mistake when there are no obvious fluctuations in the concentration. These three tasks might also be confused with each other sometimes; it is mainly because motion artifacts exist. It will be improved with other algorithms in our further work.

Table 2 also compares this work with other recently published fNIRS-based mental task classification. With the designed multichannel fNIRS system, dedicated source-detector layout, and dual-level intensity data acquisition, the proposed work is convenient to wear and transmit data and achieves the highest classification accuracy with 4 states.

In conclusion, dual-level light intensity excitation will benefit the brain activity classification by providing more useful channels, which is important for portable compact NIRS-BCI equipment when using a multi-interval source/detector layout to locate the monitoring point on a specific brain region. And the deep forest algorithm can achieve higher accuracy than other methods, especially without scan-

ning. This indicates that deep forest has a potential to deal with raw data, which will cost less time and is promising in future NIRS-BCI application.

## 5. Conclusions

This paper proposed a continuous-wave fNIRS system, which has multiple channels of different source-detector intervals to extract the spatial characteristic and collect data, providing flexibility for choosing the concerned brain region. The system is compactable and wearable by involving a dual-level light-emitting intensity mode for better SNR. The system was applied to collect fNIRS data during three cognitive mental tasks and the rest state in the PFC. By employing a deep forest algorithm, our system could achieve a higher classification accuracy than other methods, even with raw data. According to the comparison of different hyperparameters, we determined the optimal model with three-grained scanning. Finally, this work achieves 86.9% accuracy for 4 different cortical activation states.

## Disclosure

The research in this paper is an extension of the previous work presented as conference abstract in 2019 IEEE Biomedical Circuits and Systems Conference (BioCAS)

according to the following link: <https://ieeexplore.ieee.org/document/8919082>.

## Conflicts of Interest

The authors declare that there is no conflict of interest regarding the publication of this paper.

## Acknowledgments

This work is supported by the National Key Research and Development Program of China under Grant No. 2019YFB2204500, in part by the Natural Science Foundation of China (NSFC) under Grant 61904104, and in part by the Science, Technology and Innovation Action Plan of Shanghai Municipality, China under Grant No. 1914220370.

## References

- [1] F. F. Jobsis, "Noninvasive, infrared monitoring of cerebral and myocardial oxygen sufficiency and circulatory parameters," *Science*, vol. 198, no. 4323, pp. 1264–1267, 1977.
- [2] D. A. Boas, C. E. Elwell, M. Ferrari, and G. Taga, "Twenty years of functional near-infrared spectroscopy: introduction for the special issue," *NeuroImage*, vol. 85, pp. 1–5, 2014.
- [3] J. Shin, J. Kwon, and C.-H. Im, "A ternary hybrid eeg-nirs brain-computer interface for the classification of brain activation patterns during mental arithmetic, motor imagery, and idle state," *Frontiers in Neuroinformatics*, vol. 12, p. 5, 2018.
- [4] G. Bauernfeind, D. Steyrl, C. Brunner, and G. R. Müller-Putz, "Single trial classification of fnirs-based brain-computer interface mental arithmetic data: a comparison between different classifiers," in *2014 36th Annual International Conference of the IEEE Engineering in Medicine and Biology Society*, pp. 2004–2007, Chicago, IL, USA, August 2014.
- [5] K.-S. Hong, N. Naseer, and Y.-H. Kim, "Classification of prefrontal and motor cortex signals for three-class fNIRS-BCI," *Neuroscience Letters*, vol. 587, pp. 87–92, 2015.
- [6] L. C. Schudlo and T. Chau, "Towards a ternary NIRS-BCI: single-trial classification of verbal fluency task, Stroop task and unconstrained rest," *Journal of Neural Engineering*, vol. 12, no. 6, article 066008, 2015.
- [7] S. D. Power, A. Kushki, and T. Chau, "Automatic single-trial discrimination of mental arithmetic, mental singing and the no-control state from prefrontal activity: toward a three-state NIRS-BCI," *BMC Research Notes*, vol. 5, no. 1, p. 141, 2012.
- [8] L. Nyberg, P. Marklund, J. Persson et al., "Common prefrontal activations during working memory, episodic memory, and semantic memory," *Neuropsychologia*, vol. 41, no. 3, pp. 371–377, 2003.
- [9] A. von Lüthmann, C. Herff, D. Heger, and T. Schultz, "Toward a wireless open source instrument: functional near-infrared spectroscopy in mobile neuroergonomics and BCI applications," *Frontiers in Human Neuroscience*, vol. 9, no. 871, 2015.
- [10] T. Watanabe, R. Sekine, T. Mizuno, and M. Miwa, "Development of portable, wireless and smartphone controllable near-infrared spectroscopy system," in *Oxygen Transport to Tissue XXXVIII. Advances in Experimental Medicine and Biology*, vol. 923pp. 385–392, Springer, Cham.
- [11] A. V. Lüthmann, "M3BA: new technology for mobile hybrid BCIs," in *Proceedings of the 6th International Brain-Computer Interface Meeting*, organized by the BCI Society, 2016.
- [12] M. Abtahi, G. Cay, M. J. Saikia, and K. Mankodiya, "Designing and testing a wearable, wireless fNIRS patch," in *2016 38th Annual International Conference of the IEEE Engineering in Medicine and Biology Society (EMBC)*, pp. 6298–6301, Orlando, FL, USA, August 2016.
- [13] D. Chitnis, D. Airantzis, D. Highton et al., "Towards a wearable near infrared spectroscopic probe for monitoring concentrations of multiple chromophores in biological tissue in vivo," *Review of Scientific Instruments*, vol. 87, no. 6, article 065112, 2016.
- [14] D. Wyser, O. Lambercy, F. Scholkmann, M. Wolf, and R. Gassert, "Wearable and modular functional near-infrared spectroscopy instrument with multidistance measurements at four wavelengths," *Neurophotonics*, vol. 4, no. 4, article 041413, 2017.
- [15] F. Scholkmann, S. Kleiser, A. J. Metz et al., "A review on continuous wave functional near-infrared spectroscopy and imaging instrumentation and methodology," *Neuroimage*, vol. 85, pp. 6–27, 2014.
- [16] G. Gratton, J. S. Maier, M. Fabiani, W. W. Mantulin, and E. Gratton, "Feasibility of intracranial near-infrared optical scanning," *Psychophysiology*, vol. 31, no. 2, pp. 211–215, 1994.
- [17] S. C. Bunce, M. Izzetoglu, K. Izzetoglu, B. Onaral, and K. Pourrezaei, "Functional nearinfrared spectroscopy," *IEEE Engineering in Medicine and Biology Magazine*, vol. 25, no. 4, pp. 54–62, 2006.
- [18] D. T. Delpy, M. Cope, P. van der Zee, S. Arridge, S. Wray, and J. Wyatt, "Estimation of optical pathlength through tissue from direct time of flight measurement," *Physics in Medicine and Biology*, vol. 33, no. 12, pp. 1433–1442, 1988.
- [19] A. Sassaroli and S. Fantini, "Comment on the modified Beer-Lambert law for scattering media," *Physics in Medicine and Biology*, vol. 49, no. 14, pp. N255–N257, 2004.
- [20] L. Kocsis, P. Herman, and A. Eke, "The modified Beer-Lambert law revisited," *Physics in Medicine & Biology*, vol. 51, no. 5, pp. N91–N98, 2006.
- [21] Y. Fukui, Y. Ajichi, and E. Okada, "Monte Carlo prediction of near-infrared light propagation in realistic adult and neonatal head models," *Applied Optics*, vol. 42, no. 16, pp. 2881–2887, 2003.
- [22] M. Kohl, C. Nolte, H. R. Heekeren et al., "Determination of the wavelength dependence of the differential pathlength factor from near-infrared pulse signals," *Physics in Medicine and Biology*, vol. 43, no. 6, pp. 1771–1782, 1998.
- [23] G. E. Strangman, Z. Li, and Q. Zhang, "Depth sensitivity and source-detector separations for near infrared spectroscopy based on the Colin 27 brain template," *PLoS One*, vol. 8, no. 8, article e66319, 2013.
- [24] C.-K. Lee, C. W. Sun, P. L. Lee et al., "Study of photon migration with various source-detector separations in near-infrared spectroscopic brain imaging based on three-dimensional Monte Carlo modeling," *Optics Express*, vol. 13, no. 21, pp. 8339–8348, 2005.
- [25] Z.-H. Zhou and J. Feng, "Deep forest: towards an alternative to deep neural networks," in *Proceedings of the 26th International Joint Conference on Artificial Intelligence*, pp. 3553–3559, 2017.
- [26] G. Lee, S. H. Jin, S. T. Yang, J. An, and B. Abibulaev, "Crosscorrelation between HbO and HbR as an effective feature of motion artefact in fNIRS signal," in *2018 6th International Conference on Brain-Computer Interface (BCI)*, pp. 1–3, GangWon, South Korea, January 2018.



## Research Article

# Improved Spatial Resolution of Electroencephalogram Using Tripolar Concentric Ring Electrode Sensors

Xiang Liu,<sup>1</sup> Oleksandr Makeyev<sup>2</sup>,<sup>1</sup> and Walter Besio<sup>1</sup>

<sup>1</sup>Department of Electrical, Computer, and Biomedical Engineering, University of Rhode Island, 4 East Alumni Ave., Kingston, RI 02881, USA

<sup>2</sup>Department of Mathematics, Diné College, 1 Circle Dr., Tsaile, AZ 86556, USA

Correspondence should be addressed to Oleksandr Makeyev; [omakeyev@dinecollege.edu](mailto:omakeyev@dinecollege.edu)

Received 22 November 2019; Accepted 29 April 2020; Published 8 June 2020

Academic Editor: Tiago H. Falk

Copyright © 2020 Xiang Liu et al. This is an open access article distributed under the Creative Commons Attribution License, which permits unrestricted use, distribution, and reproduction in any medium, provided the original work is properly cited.

The electroencephalogram (EEG) is broadly used for research of brain activities and diagnosis of brain diseases and disorders. Although EEG provides good temporal resolution of millisecond or less, it does not provide good spatial resolution. There are two main reasons for the poor spatial resolution: the blurring effects of the head volume conductor and poor signal-to-noise ratio. We have developed a tripolar concentric ring electrode (TCRE) Laplacian sensor and now report on computer simulations comparing spatial resolution between conventional EEG disc electrode sensors and TCRE Laplacian sensors. We also performed visual evoked stimulus experiments and acquired visual evoked potentials (VEPs) from healthy human subjects. From the simulations, we found that TCRE Laplacian sensors can provide approximately a tenfold improvement in spatial resolution and pass signals from specific volumes. Placing TCRE sensors near the brain region of interest will allow passage of the wanted signals and rejection of distant interference signals. We were also able to detect VEPs on the scalp surface and show that TCREs separated VEP sources better than conventional disc electrodes.

## 1. Introduction

Electroencephalography (EEG) is widely used in diagnosis of brain-related disorders and research. However, EEG suffers from poor spatial resolution due to the blurring effects primarily from different conductivities of the volume conductor [1].

To improve the spatial resolution, the surface Laplacian has been applied to EEG [1, 2]. The surface Laplacian is a high-pass spatial filter, which sharpens the blurred potential distribution on the surface [2] and produces an image proportional to the cortical potentials [3].

Two approaches have been used to calculate the surface Laplacian. The global surface Laplacian approach is based on the potential interpolation on the surface [4–6]. A drawback of this approach is that building the potential interpolation equations requires a significant number of electrodes [7].

The local surface Laplacian approach approximates the surface Laplacian based on potentials from neighboring electrodes only [8]. This approach also has significant drawbacks:

(1) when the neighboring electrodes are too sparse, which is usually the case with the 10-20 system configuration, the resulting local surface Laplacian might not be a good estimation of the surface Laplacian [7], and (2) the locations where the surface Laplacian could be estimated are limited.

This paper assesses a local Laplacian that overcomes the drawback of sparse electrode distortion by employing the tripolar concentric ring electrode (TCRE; Figure 1) introduced by Besio et al. [9]. Instead of using neighboring electrodes to estimate the surface Laplacian, the three recording surfaces of a single TCRE (outer ring, middle ring, and the central disc) are used. The second drawback can also be alleviated by interpolation of the TCRE local surface Laplacian. To illustrate these points, the global surface Laplacian and local surface Laplacian are compared using a four-layer concentric inhomogeneous spherical head model [10]. This model has been selected for this study to ensure consistency with previous results of others having used it to compare Laplacian estimation methods [11]. Moreover, unlike some of the more realistic head models, it allows straightforward modeling of

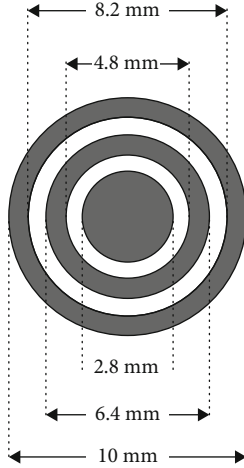


FIGURE 1: Tripolar concentric ring electrode with dimensions of its central disc, middle ring, and outer ring.

dipoles resembling visual evoked potentials, implementation of Laplacian estimation approaches, calculation of half-sensitivity volume, and application of spatial subspace decomposition. In the comparison, the global surface Laplacian estimation is based on the spherical spline interpolation method introduced by Perrin et al. [6], while the local surface Laplacian estimation is based on the TCRE Laplacian algorithm [9]. Noise is added to the simulations to make the results more realistic.

## 2. Materials and Methods

**2.1. Global Surface Laplacian Estimation Based on Spherical Spline Interpolation.** The spherical spline interpolation method was introduced by Perrin et al. [6]. This model approximates the head as the surface of a sphere. The equations described by Perrin et al. for the spherical spline interpolation are

$$V(\mathbf{r}) = c_0 + \frac{1}{4\pi} \sum_{i=1}^N c_i \sum_{n=1}^{\infty} \frac{2n+1}{n^m(n+1)^m} \mathbf{p}_n(\cos(\mathbf{r}, \mathbf{r}_i)), \quad (1)$$

where  $N$  is the number of electrodes,  $m$  is the order of the spline interpolation ( $m=3$  for this study),  $\mathbf{r}$  is the vector of the location where the potential is interpolated,  $\mathbf{r}_i$  is the vector of the location of the  $i^{\text{th}}$  electrode,  $\mathbf{p}_n$  is the  $n^{\text{th}}$  degree Legendre polynomial. With  $n$  increasing in (1) as part of the sum, in Perrin et al. [6],  $\mathbf{p}_n$  was “computed via the recurrence relation” and “the sum of the first 7 terms of the series” was “sufficient to obtain a precision of  $10^{-6}$ ”. In this study, the maximum value of  $n$  was increased to 60 to further improve the precision. The parameters vector  $C$  is the solution of equations (2) and (3):

$$GC + Tc_0 = Z, \quad (2)$$

$$T' C = 0, \quad (3)$$

where  $T' = (1, 1, \dots, 1)$ ,  $C' = (c_1, c_2, \dots, c_N)$ ,  $Z' = (z_1, z_2, \dots, z_N)$ ,  $G = (g_{ij}) = (g(\cos(\mathbf{r}, \mathbf{r}_i)))$ , and  $g(x) = 1/4\pi \sum_{n=1}^{\infty} (2n+1)/n^m(n+1)^m \mathbf{p}_n(x)$ . The surface Laplacian operator in the spherical coordinate system is defined as

$$\Delta_{\text{surf}} = \frac{1}{r^2} \frac{\partial}{\sin \theta} \frac{\partial}{\partial \theta} \left( \sin \theta \frac{\partial}{\partial \theta} \right) + \frac{1}{r^2 \sin^2 \theta} \frac{\partial^2}{\partial \phi^2}. \quad (4)$$

Applying the operator from equation (4) to equation (1) produces the surface Laplacian of the spherical interpolation:

$$\Delta_{\text{surf}} V(\mathbf{r}) = -\frac{1}{4\pi r^2} \sum_{i=1}^N c_i \sum_{n=1}^{\infty} \frac{2n+1}{n^{m-1}(n+1)^{m-1}} \mathbf{p}_n(\cos(\mathbf{r}, \mathbf{r}_i)). \quad (5)$$

We used a truncated singular value decomposition method to solve the inverse problem of the ill-posed matrix in equations (2) and (3) [12].

**2.2. Local Surface Laplacian Estimation Based on Tripolar Concentric Ring Electrode.** Based on the 2-dimensional Taylor expansion of the potential on the surface Laplacian nine-point locations, the tripolar Laplacian is given by the combination of the potentials from the three recording surfaces of the TCRE [9]:

$$\text{SL} = -\frac{16(V_m - V_d) - (V_o - V_d)}{3R^2}. \quad (6)$$

In equation (6), SL denotes the surface Laplacian,  $V_d$  denotes the potential from the central disc,  $V_m$  denotes the potential from the middle ring,  $V_o$  denotes the potential from the outer ring, and  $R$  is the radius of the middle ring. As  $R$  changes, the size of the sensor changes, and the spatial resolution also varies with it.

**2.3. The Four-Layer Spherical Head Model and the Analytical Surface Laplacian.** In our simulations, we used a four-layer concentric inhomogeneous spherical model [10] to represent the human head (Figure 2). Current dipoles, described later, are employed to model the brain activity.

The potential on the surface of the model due to a current dipole located at the  $z$ -axis in the brain is given by the following equations [10]:

$$V_x = \frac{P_x \cos \phi}{4\pi\sigma_4 R^2} \sum_{n=1}^{\infty} \frac{(2n+1)^4 f^{n-1}(cd)^{2n+1} P_n^1(\cos \theta)}{n\Gamma}, \quad (7)$$

for the  $x$ -direction component of the dipole,

$$V_y = \frac{P_y \sin \phi}{4\pi\sigma_4 R^2} \sum_{n=1}^{\infty} \frac{(2n+1)^4 f^{n-1}(cd)^{2n+1} P_n^1(\cos \theta)}{n\Gamma}, \quad (8)$$



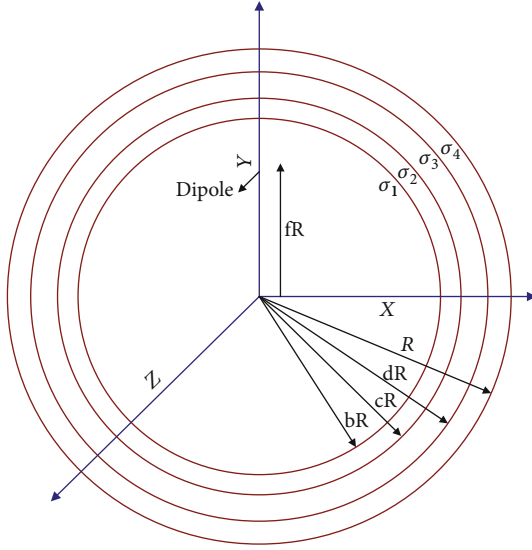


FIGURE 2: Four-layer concentric inhomogeneous spherical head model with the radii of the layers equal to  $R = 8.8\text{cm}$ ,  $dR = 8.5\text{cm}$ ,  $cR = 8.1\text{cm}$ , and  $bR = 7.9\text{cm}$  and the conductivities of the layers equal to  $\sigma_1 = 3.3 \times 10^{-3}$ ,  $\sigma_2 = 10.0 \times 10^{-3}$ ,  $\sigma_3 = 4.2 \times 10^{-5}$ , and  $\sigma_4 = 3.3 \times 10^{-3}\text{S/cm}$ , from inside to outside, respectively.

for the  $y$ -direction component of the dipole, and

$$V_z = \frac{P_z}{4\pi\sigma_4 R^2} \sum_{n=1}^{\infty} \frac{(2n+1)^4 f^{n-1} (cd)^{2n+1} P_n^1(\cos\theta)}{n\Gamma}, \quad (9)$$

for the  $z$ -direction component of the dipole, where

$$\begin{aligned} \Gamma = & d^{2n+1} \{ b^{2n+1} n(k_1 - 1)(k_2 - 1)(n+1) \\ & + C^{2n+1} (k_1 n + n + 1)(k_2 n + n + 1) \} \\ & \times \{ (k_3 n + n + 1) + (n+1)(k_3 - 1)d^{2n+1} \} \\ & + (n+1)c^{2n+1} \{ b^{2n+1} (k_1 - 1)(k_2 n + k_2 + n) \\ & + c^{2n+1} (k_1 n + n + 1)(k_2 - 1) \} \\ & \times \{ n(k_3 - 1) + (k_3 n + k_3 + n)d^{2n+1} \}, \end{aligned} \quad (10)$$

$$k_1 = \frac{\sigma_1}{\sigma_2},$$

$$k_2 = \frac{\sigma_2}{\sigma_3},$$

$$k_3 = \frac{\sigma_3}{\sigma_4}.$$

Applying the surface Laplacian operator equation (4) to equations (7), (8), and (9), the analytical surface Laplacian is given by

$$\begin{aligned} \Delta_{surf} V_x = & \frac{P_x \cos\phi}{4\pi\sigma_4 R^2} \sum_{n=1}^{\infty} \frac{1}{n\Gamma} \times \left\{ (2n+1)^4 f^{n-1} (cd)^{2n+1} \right. \\ & \cdot \left. \left( -\frac{P_n^1(\cos\theta)}{R^2 \sin^2\theta} + \Delta_{surf} P_n^1(\cos\theta) \right) \right\}, \end{aligned} \quad (11)$$

$$\begin{aligned} \Delta_{surf} V_y = & \frac{P_y \sin\phi}{4\pi\sigma_4 R^2} \sum_{n=1}^{\infty} \frac{1}{n\Gamma} \times \left\{ (2n+1)^4 f^{n-1} (cd)^{2n+1} \right. \\ & \cdot \left. \left( -\frac{P_n^1(\cos\theta)}{R^2 \sin^2\theta} + \Delta_{surf} P_n^1(\cos\theta) \right) \right\}, \end{aligned} \quad (12)$$

$$\begin{aligned} \Delta_{surf} V_z = & \frac{P_z}{4\pi\sigma_4 R^2} \sum_{n=1}^{\infty} \frac{1}{n\Gamma} \\ & \times \left\{ (2n+1)^4 f^{n-1} (cd)^{2n+1} \Delta_{surf} P_n^1(\cos\theta) \right\}, \end{aligned} \quad (13)$$

where

$$\begin{aligned} \Delta_{surf} P_n^1(\cos\theta) = & \frac{1}{R^2 \sin^3\theta} \{ P_n(\cos\theta) (n(n+1)^2 \cos\theta \sin^2\theta \\ & - (n+1) \cos\theta) + P_{n+1}(\cos\theta) ((n+1) \\ & - n(n+1) \sin^2\theta) \}, \end{aligned}$$

$$\Delta_{surf} P_n(\cos\theta) = -\frac{n(n+1)}{R^2} P_n(\cos\theta). \quad (14)$$

By rotating the coordinate system, the analytical potential and surface Laplacian imposed by a dipole at an arbitrary brain location area can be computed according to equations (7)–(9) and (11)–(13).

**2.4. Sensitivity Distribution of Conventional Electrodes and TCRES Based on Half-Sensitivity Volume.** The sensitivity distribution of an electrode is directly related to its spatial resolution. In this comparison, the lead field was used to calculate the sensitivity distribution. The lead field is the current density distribution in the volume conductor generated by feeding current to electrode pairs [13]. We also employed the concept of half-sensitivity volume (HSV), which is defined as the volume where the measured sensitivity is at least half of the maximum sensitivity [13], to quantize the sensitivity distribution for the electrodes.

**2.5. Sensitivity Comparison of Conventional Electrodes and TCRES Based on Spatial Subspace Decomposition Method.** Common spatial subspace decomposition (CSSD), which helps to retrieve signal components specific to one condition from complex EEG background, was developed to separate specific brain activities from the background [14]. Since EEG is considered to have spatial resolution of 3.0 to 4.0 cm [15–17], we tested at a higher spatial resolution for comparison. In our simulation, an 8 by 8 simulated electrode array was placed on the scalp above the visual cortex area with a 1.0 cm center-to-center distance between electrodes to maximize the spatial resolution. Potential integration was performed separately and independently for each electrode to eliminate mutual influence of neighboring electrodes. A simulated signal dipole with eccentricity of 0.9 was placed under the electrode array. Two simulated noise dipoles with an eccentricity of 0.75 were concurrently activated with the signal dipole under the array as background brain activity. In the simulation, we first calculated the simulated background by setting the magnitude of the signal dipole to zero. Then,

TABLE 1: Locations and moments of the ten dipoles for modeling brain activities.

Dipole number	X (cm)	Y (cm)	Z (cm)	Moment (R, radial; T, tangential; U, unit; and D, dipole)
1	4.3	-5.3	4	RUD
2	6	-3	4	RUD
3	5	-4.6	4.1	RUD
4	-2.3	-4.4	6	RUD
5	-2.2	4.6	6	RUD
6	4.3	-5.3	4	TUD
7	6	-3	4	TUD
8	5	-4.6	4.1	TUD
9	-2.3	-4.4	6	TUD
10	-2.2	4.6	6	TUD

we calculated the simulated visual evoked potential (VEP) combined with background. Finally, the CSSD was applied to the simulated data to extract the VEP. The simulated TCRES EEG (tEEG) VEP from the TCRES was calculated for comparison. Another simulation with only the signal dipole was also conducted to compare the power distribution of the simulated disc potential and tripolar Laplacian. In all of the simulations, potentials on the disc electrodes were calculated from the conventional disc electrodes that had the same diameter as the outer ring of the TCRES, 1.0 cm.

*2.6. Comparison of Global Spline Surface Laplacian and Local TCRES Surface Laplacian with Computer Simulation.* To model the activities of the brain cortex area, ten dipoles with an eccentricity around 0.89 were used one at a time (Table 1). The locations of the dipoles were modeled in the visual cortex area of the brain to compare the simulation results to those of actual VEP recording experiments. The moments of the first five dipoles had a radial direction, and the remaining five dipoles were at the same locations, but with a tangential direction.

Since an electrode shunts the scalp area under it, to simulate the potential on the recording surfaces of the TCRES and conventional disc electrodes, we averaged a number of “sampling points” uniformly distributed on the surface of the electrode. To determine the number of sampling points needed for stable calculations, we incrementally increased their density and compared the averaged potential until the difference in potential due to adding more points was less than 0.1%. The order of magnitude of that number was in the thousands of sampling points per electrode. We used the same density of sampling points for each of the recording surfaces of the TCRES and the same sampling points for each TCRES. A similar procedure was used for the disc electrodes. In the simulation, TCRES were given the same dimensions as shown in Figure 1, and conventional disc electrodes were simulated with the same diameter as the outer ring of the TCRES, 1.0 cm.

The global spline surface Laplacian and the local TCRES surface Laplacian were calculated at the locations of the elec-

trodes and then compared to the analytical surface Laplacian using the correlation coefficient.

*2.7. Statistical Analysis.* All the statistical analysis was performed using Design-Expert software (Stat-Ease Inc., Minneapolis, MN, USA). Full factorial design of analysis of variance (ANOVA) was used with four categorical factors [18]. The first factor (A) was the type of the electrode presented at two levels corresponding to conventional disc electrodes and tripolar concentric ring electrodes. The second factor (B) was the number of electrodes presented at four levels corresponding to 19, 32, 64, and 128 electrodes. The 19 electrodes were placed at the standard 10-20 system while 32, 64, and 128 electrode locations were selected from the 5-5 system [19]. The third factor (C) was the presence and type of noise presented at four levels corresponding to no noise, presence of white Gaussian noise (WGN) at 20% standard deviation ratio of the WGN to the potential [20], presence of a deep noise dipole with an eccentricity of around 0.85 (simulating brain activity not considered to be the brain source of interest), and presence of both WGN and the noise dipole. Finally, the fourth factor (D) was the dipole location presented at ten levels corresponding to 10 signal dipole locations from Table 1. The response variable was the correlation coefficient of the simulated surface Laplacian and the analytical surface Laplacian calculated for each of the  $2 * 4 * 4 * 10 = 320$  combinations of levels of four factors. The full factorial design of our study is presented in Table 2.

*2.8. Visual Evoked Surface Potential and Laplacian Recording Experiment.* In this experiment, the scalp was prepared with the mild abrasive NuPrep (Natus Medical West Warwick RI). Next, recording electrodes with approximately 0.2 cm of Ten20 paste (for skin-to-electrode impedance matching and to hold the electrodes in place) were placed over the visual cortex. Finally, reference and ground electrodes were placed on the forehead between the eyes in an identical manner. Signals from the outer ring of the TCRES were used to emulate the disc electrodes. Synchrony between these two signals has been demonstrated in time domain using cross-correlation in phantom and human data ( $r \geq 0.99$ ) [21] as well as in frequency domain using coherence in human data ( $C \geq 0.98$ ) [22]. Both of the results strongly suggesting equivalency of signals from the outer ring of the TCRES, and signals from conventional disc electrodes were later confirmed on a more comprehensive human dataset [23]. A flashing LED array, PS60/LED, and Comet AS40 (Natus Medical, West Warwick, RI) were used to activate the visual cortex, similar to the computer model, of the human brain and record the EEG. The visual stimulus was expected to generate a signal source in the visual cortex similar to the dipoles we placed in the computer simulation. The signals were filtered (1-70 Hz) and digitized (200 S/s). Due to the limit of the hardware, only 15 channels were available in the experiments. To keep the electrodes at a similar density as we used in the simulation, all 15 electrodes were placed over the visual cortex area from the standard 10-5 system. The locations of the electrodes are listed in Table 3. The frequency of the PS60/LED was 2 Hz. The subjects ( $n = 6$ ) were seated in a

TABLE 2: Full factorial design of analysis of variance and obtained response variable.

Group averages for 10 levels of factor D (signal dipole location)	Categorical factors			Correlation between the simulated and the analytical surface Laplacians (mean $\pm$ standard deviation)
	A: type of the electrode	B: number of electrodes	C: presence and type of noise	
1	Conventional disc	19	No noise	0.5882 $\pm$ 0.1581
2	TCRE	19	No noise	0.9908 $\pm$ 0.0196
3	Conventional disc	32	No noise	0.6669 $\pm$ 0.1693
4	TCRE	32	No noise	0.9823 $\pm$ 0.0406
5	Conventional disc	64	No noise	0.8242 $\pm$ 0.1141
6	TCRE	64	No noise	0.9937 $\pm$ 0.0073
7	Conventional disc	128	No noise	0.8885 $\pm$ 0.0989
8	TCRE	128	No noise	0.9737 $\pm$ 0.0311
9	Conventional disc	19	WGN	0.4801 $\pm$ 0.2041
10	TCRE	19	WGN	0.9649 $\pm$ 0.0104
11	Conventional disc	32	WGN	0.6035 $\pm$ 0.1138
12	TCRE	32	WGN	0.9634 $\pm$ 0.0074
13	Conventional disc	64	WGN	0.7095 $\pm$ 0.0139
14	TCRE	64	WGN	0.9619 $\pm$ 0.0411
15	Conventional disc	128	WGN	0.7515 $\pm$ 0.0783
16	TCRE	128	WGN	0.9633 $\pm$ 0.0050
17	Conventional disc	19	Noise dipole	0.4662 $\pm$ 0.2787
18	TCRE	19	Noise dipole	0.8846 $\pm$ 0.1186
19	Conventional disc	32	Noise dipole	0.6199 $\pm$ 0.2052
20	TCRE	32	Noise dipole	0.9236 $\pm$ 0.0877
21	Conventional disc	64	Noise dipole	0.7950 $\pm$ 0.1177
22	TCRE	64	Noise dipole	0.9549 $\pm$ 0.0424
23	Conventional disc	128	Noise dipole	0.9082 $\pm$ 0.0904
24	TCRE	128	Noise dipole	0.9877 $\pm$ 0.1334
25	Conventional disc	19	WGN+dipole	0.4752 $\pm$ 0.0224
26	TCRE	19	WGN+dipole	0.9480 $\pm$ 0.1864
27	Conventional disc	32	WGN+dipole	0.6780 $\pm$ 0.0738
28	TCRE	32	WGN+dipole	0.9390 $\pm$ 0.0376
29	Conventional disc	64	WGN+dipole	0.7329 $\pm$ 0.0156
30	TCRE	64	WGN+dipole	0.9551 $\pm$ 0.0611
31	Conventional disc	128	WGN+dipole	0.7614 $\pm$ 0.0881
32	TCRE	128	WGN+dipole	0.9580 $\pm$ 0.0097

comfortable chair with their eyes approximately 4.0 cm from the photic stimulator. For each subject, we recorded about two-and-a-half minutes of EEG signals. There was approximately 30 seconds of baseline EEG, with no photic stimulation, and then approximately two minutes of photic stimulation.

The photic trigger signal was also recorded to synchronize epochs during ensemble averaging. The analysis of recorded EEG signals depended on the type of signals recorded. For the EEG from the outer ring of the TCRES, the spline interpolation and surface Laplacian methods discussed above were applied to calculate the spline surface

Laplacian and map them to the surface of the spherical head model over the visual cortex area. For the TCRE EEG surface Laplacian, we simply applied the interpolation algorithm to map the recorded Laplacian values to the corresponding surface.

### 3. Results

*3.1. Sensitivity Distribution of Conventional Electrodes and TCRES Based on Half-Sensitivity Volume.* Figure 3 shows the simulated HSV of a pair of conventional disc electrodes and a TCRE. In the HSV computer simulation, a pair of disc

TABLE 3: Electrode locations in the VEP experiments.

Electrode location	X (cm)	Y (cm)	Z (cm)
CP5	-7.885	-2.974	2.499
P3	-4.990	-5.958	4.127
Pz	0.000	-6.283	6.151
P4	4.981	-5.958	4.127
CP6	7.885	-2.974	2.499
P5	-6.521	-5.588	1.874
P6	6.521	-5.588	1.883
P7	-7.075	-5.157	-0.774
PO7	-5.139	-7.101	-0.616
PO3h	-2.526	-8.008	2.622
POz	0.000	-8.175	3.238
PO4h	2.517	-8.008	2.622
P8	7.075	-5.166	-0.774
O1	-2.702	-8.351	-0.414
O2	2.702	-8.351	-0.414

electrodes was placed on the spherical surface separated by 90 degrees. This separation angle was selected based on where the reference and signal electrode placements were in physical experiments. In our physical human VEP experiments, the separation angle, from the forehead to the visual cortex, was more like 180 degrees, rather than just 90 degrees; however, the larger angle would not affect the results. A single TCRE was utilized since it can be seen as a combination of two pairs of electrodes at a single location: the outer ring minus the disc and the middle ring minus the disc. Simulated potentials on the electrodes were calculated from a unit dipole located in the inner sphere of the brain. After the potentials were calculated, the dipole was moved. This procedure was repeated until the HSV volume could be determined. The simulation shows that the HSV of the disc electrode is 9.6 times greater than the HSV of TCREs.

*3.2. Sensitivity Comparison of Conventional Electrodes and TCREs Based on Spatial Subspace Decomposition Method.* The 64 extracted signals from the  $8 \times 8$  arrays of TCREs and disc electrodes were normalized separately. The average power of the 64 normalized disc potentials was equal to  $0.44 \pm 0.31$  while the average power of the 64 normalized tripolar Laplacians was equal to  $0.23 \pm 0.24$  (mean  $\pm$  standard deviation). These results indicate that the distribution of the power of the tripolar Laplacian is more focused on a smaller number of TCREs, while the power of the disc potential tends to be distributed over a larger number of disc electrodes.

Figure 4 shows the simulated normalized VEP from a location near the center of the 64-electrode array. The  $x$ -axis is the distance from the electrodes to the signal dipole, the  $y$ -axis is the normalized magnitude of the signal calculated at each electrode of the  $8 \times 8$  array, “\*” denotes the disc electrode, “o” denotes the TCRE, and “+” denotes the analytical Laplacian. From Figure 4, as the distance increases between the electrode and the dipole source, the magnitude of the

recorded signal on TCREs attenuates much quicker than that recorded on the disc electrodes. In other words, the VEP power was mainly distributed on just a few close TCREs, while it was distributed over a wider area of the conventional disc electrode array. It can also be seen that the TCRE Laplacian is very similar to the analytical Laplacian.

*3.3. Comparison of Global Spline Surface Laplacian and Local TCRE Surface Laplacian with Computer Simulation.* Correlation coefficient data obtained in this simulation for 320 combinations of factor levels is presented in Table 2 averaged for ten dipole locations.

The effect of factors A, B, C, and D on the correlation coefficient was assessed along with the effect of all possible two- and three-factor interactions. The effect of the four-factor interaction ABCD could not be evaluated. The ANOVA results suggest that all the factors and all of the assessed interactions have statistically significant effects in the model (d.f. = 238,  $F = 17.6$ ,  $p < 0.0001$ ) for the optimal power transformation of 2.81 determined using the Box-Cox procedure [18]. The effects of the main factors were A (d.f. = 1,  $F = 2736.5$ ,  $p < 0.0001$ ), B (d.f. = 3,  $F = 120.1$ ,  $p < 0.0001$ ), C (d.f. = 3,  $F = 34.7$ ,  $p < 0.0001$ ), and D (d.f. = 9,  $F = 10.3$ ,  $p < 0.0001$ ).

*3.4. Visual Evoked Surface Laplacian Comparison Experiments.* From Figure 5, we can see that the TCRE Laplacian sensors were able to separate VEP sources. In panel (a), the spline Laplacian map from the 15 disc electrode signals at 95 ms in panel (c), in the top central area there is a red and orange area (designated with an arrow). In the same area of panel (b), from 110 ms in panel (d), we can see the TCRE Laplacian sensor map from the 15 TCRE signals which shows that there were two distinct sources (shown by arrow). Panels (c) and (d) show the normalized grand-averaged EEG and tEEG VEPs used to build the maps in panels (a) and (b), respectively. From panel (c), it can be seen that many of the traces are similar while this is not the case in panel (d) from the TCREs. From panels (c) and (d), we can see that there is a positive wave at approximately 50 to 110 ms and 105 to 115 ms, respectively, after the photic stimulation pulse.

## 4. Discussion

We conducted multiple computer simulations and acquired real signals to compare spatial sensitivity between disc electrode and TCRE sensors. The sensitivity comparison of the disc electrode spline Laplacian and tripolar Laplacian based on HSV shows that the tripolar Laplacian is more sensitive than the disc electrode spline Laplacian. The HSV for the tripolar Laplacian is nearly 10 times smaller than the disc electrode spline Laplacian HSV (Figure 3). These results show that the tripolar Laplacian records signals from a local volume compared to two broad volumes for the disc electrode spline Laplacian.

We also used the CSSD method and showed that TCRE sensors are more focused on local potentials. This can be explained in terms of obtained HSV results. The TCRE sensors are sensitive to local sources so only the sensors that

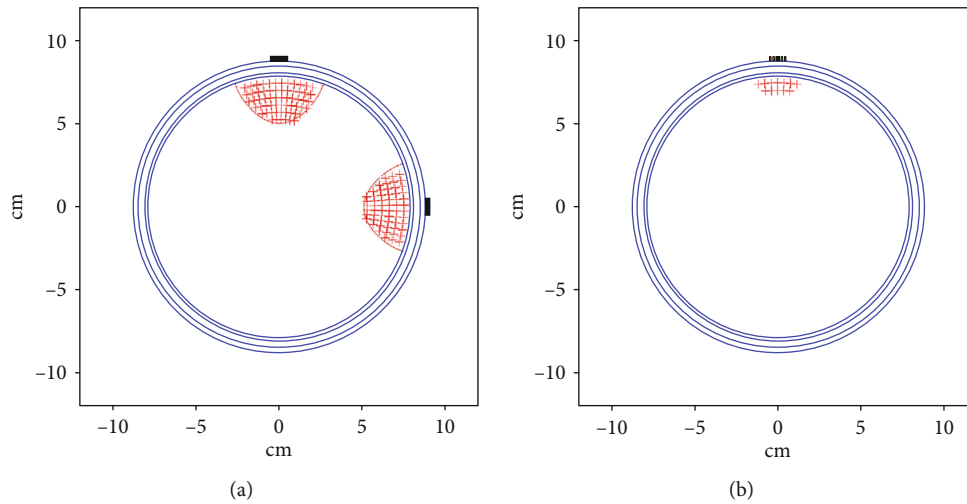


FIGURE 3: The red (hashed) lines show the HSV of conventional disc electrodes (a) and TCRES (b).

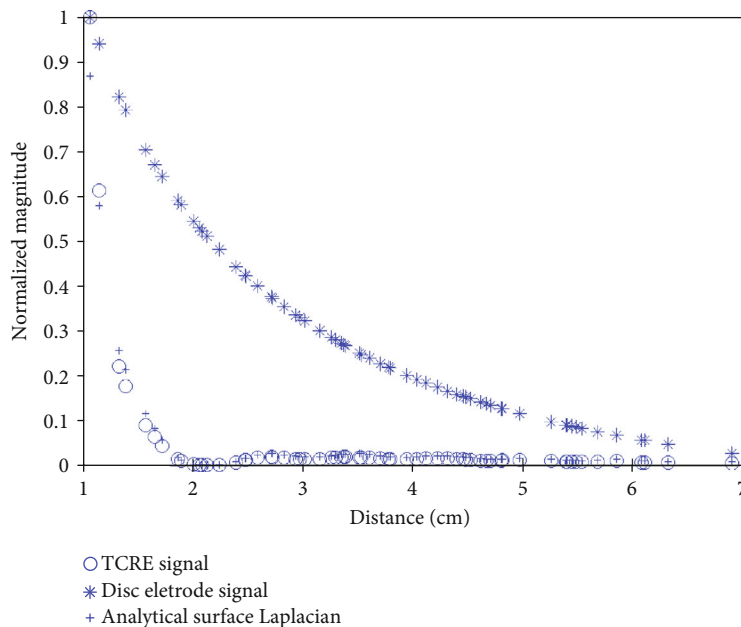


FIGURE 4: A comparison, at a location near the center of the  $8 \times 8$  array, of the calculated spline Laplacian “\*,” TCRE Laplacian “o,” and the analytical Laplacian, the gold standard “+.” The spline Laplacian was calculated from the disc electrode potentials. The disc electrode potentials were calculated from a uniform density of points over the outer ring of the 1.0 cm diameter TCRE similar to the way the outer ring of the TCRE was used as an emulation of the conventional disc electrode in real visual evoked potential experiments based on their equivalency [21–23]. The tripolar Laplacian matches the analytical Laplacian trace very well.

are close to the sources (whether they are signal or noise sources) will correspond to high power. At the same time, conventional disc electrodes, which have a nearly 10-fold larger HSV, record signals from a much larger volume therefore providing less discrimination between source locations. This relative lack of discrimination for conventional disc electrodes suggests that we can place TCRE sensors closer together (i.e., at higher spatial resolution than disc electrodes) and still detect independent sources.

ANOVA results for comparing the global spline surface Laplacian to the local TCRE surface Laplacian show statistical significance of the effect of all four categorical factors included in this study. While it was important to confirm that

the quality of Laplacian estimation increases with an increase in the number of electrodes (factor B), decreases in the presence of the noise (factor C), and is affected by the signal dipole location (factor D), the most important result is that, for the case of the factor A, the local TCRE Laplacian is significantly better than the global spline Laplacian at approximating the analytic Laplacian.

A potential limitation of the current full factorial design is that we could not assess the effect of interaction of all four factors. Without replications, including this interaction into the model makes it overspecified with all the degrees of freedom being in the model and none assigned to the residual (error). On the other hand, adding replications to the design



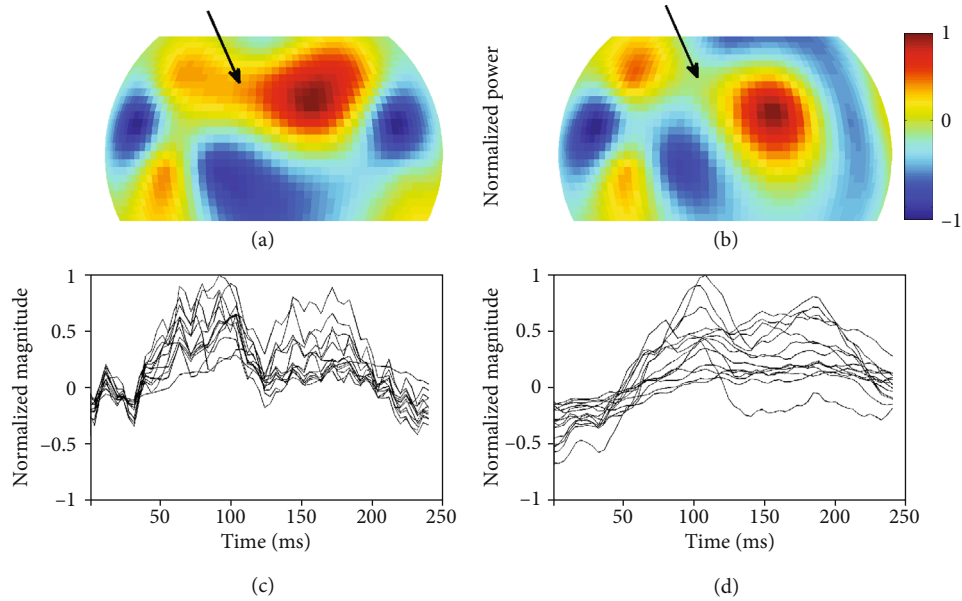


FIGURE 5: (a) Spline Laplacian VEP map (95 ms), (b) tripolar Laplacian VEP map (110 ms), (c) the normalized grand-averaged EEG VEP signals from each channel, and (d) the normalized grand-averaged tEEG VEP signals from each channel.

would be of limited value since all of the factor levels except for the two levels of factor C involving stochastic WGN are deterministic in nature so replicating the simulation for majority of level combinations would have yielded identical results. For the same reason, randomization of the simulation run order would have also been of limited value in our case even though in other cases it may help balancing out the effect of nuisance factors [18]. Other assumptions of ANOVA including normality, homogeneity of variance, and independence of observations were confirmed ensuring the validity of the analysis with no studentized residuals being outliers, i.e., falling outside the  $[-3, 3]$  range [18].

In the simulation, the eccentricities of signal dipoles were set at around 0.9, closer to the surface of the brain. This alteration was made since we were mainly interested in the visual cortex area of the brain. In a previous study [24], the eccentricities of the dipoles were usually set at 0.85 or smaller. The eccentricity of the dipole has considerable impact on the Laplacian estimation. Generally, smaller eccentricities improve the performance for both spline and tripolar Laplacian estimations.

The VEP experiments showed that we can acquire VEP signals from humans and, according to the map of Figure 5(b), were able to show two separate positive regions in the TCRE Laplacian maps that were not separated in the spline Laplacian maps (Figure 5). It should be noted that we are not certain where the sources are in the visual cortex. Panels (a) and (b) are representative of the other subjects, where there were distinct positive regions in the TCRE Laplacian maps but not in the spline Laplacian maps.

Directions of future work include moving to a more realistic head model, assessing other standard EEG responses (for example, P300), and comparing how the sensitivity profile maps on the cortical surface for TCRES and conventional disc electrodes.

## 5. Conclusion

In this study, computer simulation results serve as an analytical basis for the human visual evoked potential results using half-sensitivity volume, common spatial subspace decomposition, and a comprehensive comparison between global spline surface Laplacian and local surface Laplacian estimates via tripolar concentric ring electrodes on four-layer spherical head model using full factorial design of analysis of variance. Both computer simulations and human visual evoked potential experiments suggest that there is a statistically significant improvement in spatial resolution and estimation of the Laplacian via tripolar concentric ring electrodes compared to conventional disc electrodes and the spline Laplacian but further investigation is needed for conclusive proof.

## Data Availability

Part of the data used to support the findings of this study are available from the corresponding author upon request. The rest was lost due to a hardware failure after the manuscript was finalized.

## Disclosure

The content is solely the responsibility of the authors and does not necessarily represent the official views of the National Science Foundation.

## Conflicts of Interest

The authors declare no conflict of interest.

## Acknowledgments

We would like to thank all of our participants for their time and Zhenghan Zhu for developing the preamplifiers used to record the human VEP data. We would also like to acknowledge a partial overlap between this manuscript and Ph.D. thesis “A comparison of tripolar concentric ring electrodes to disc electrodes and an EEG real-time seizure detector design” by Xiang Liu. Parts of this research were supported by the National Science Foundation (award numbers 0933596 and 1157882 to Walter Besio as well as by award numbers 1622481 and 1914787 to Oleksandr Makeyev).

## References

- [1] P. L. Nunez, R. B. Silberstein, P. J. Cadusch, R. S. Wijesinghe, A. F. Westdorp, and R. Srinivasan, “A theoretical and experimental study of high resolution EEG based on surface Laplacians and cortical imaging,” *Electroencephalography and Clinical Neurophysiology*, vol. 90, no. 1, pp. 40–57, 1994.
- [2] B. He, “Brain electric source imaging: scalp Laplacian mapping and cortical imaging,” *Critical Reviews in Biomedical Engineering*, vol. 27, no. 3–5, pp. 149–188, 1998.
- [3] P. L. Nunez and R. Srinivasan, *Electric Fields of the Brain: the Neurophysics of EEG*, Oxford University Press, 2006.
- [4] F. Babiloni, C. Babiloni, F. Carducci, L. Fattorini, P. Onorati, and A. Urbano, “Spline Laplacian estimate of EEG potentials over a realistic magnetic resonance-constructed scalp surface model,” *Electroencephalography and Clinical Neurophysiology*, vol. 98, no. 4, pp. 363–373, 1996.
- [5] C. G. Carvalhaes and P. Suppes, “A spline framework for estimating the EEG surface Laplacian using the Euclidean metric,” *Neural Computation*, vol. 23, no. 11, pp. 2974–3000, 2011.
- [6] F. Perrin, J. Pernier, O. Bertrand, and J. F. Echallier, “Spherical splines for scalp potential and current density mapping,” *Electroencephalography and Clinical Neurophysiology*, vol. 72, no. 2, pp. 184–187, 1989.
- [7] J. Le, V. Menon, and A. Gevins, “Local estimate of surface Laplacian derivation on a realistically shaped scalp surface and its performance on noisy data,” *Electroencephalography and Clinical Neurophysiology/ Evoked Potentials Section*, vol. 92, no. 5, pp. 433–441, 1994.
- [8] B. Hjorth, “An on-line transformation of EEG scalp potentials into orthogonal source derivations,” *Electroencephalography and Clinical Neurophysiology*, vol. 39, no. 5, pp. 526–530, 1975.
- [9] W. G. Besio, K. Koka, R. Aakula, and W. Dai, “Tri-polar concentric ring electrode development for Laplacian electroencephalography,” *IEEE Transactions on Biomedical Engineering*, vol. 53, no. 5, pp. 926–933, 2006.
- [10] B. N. Cuffin and D. Cohen, “Comparison of the magnetoencephalogram and electroencephalogram,” *Electroencephalography and Clinical Neurophysiology*, vol. 47, no. 2, pp. 132–146, 1979.
- [11] C. Tandonnet, B. Boris, T. Hasbroucq, and F. Vidal, “Spatial enhancement of EEG traces by surface Laplacian estimation: comparison between local and global methods,” *Clinical Neurophysiology*, vol. 116, no. 1, pp. 18–24, 2005.
- [12] P. C. Hansen, “The truncatedSVD as a method for regularization,” *BIT Numerical Mathematics*, vol. 27, no. 4, pp. 534–553, 1987.
- [13] J. Malmivuo, V. Suihko, and H. Eskola, “Sensitivity distributions of EEG and MEG measurements,” *IEEE Transactions on Biomedical Engineering*, vol. 44, no. 3, pp. 196–208, 1997.
- [14] Y. Wang, P. Berg, and M. Scherg, “Common spatial subspace decomposition applied to analysis of brain responses under multiple task conditions: a simulation study,” *Clinical Neurophysiology*, vol. 110, no. 4, pp. 604–614, 1999.
- [15] A. R. Spitzer, L. G. Cohen, J. Fabrikant, and M. Hallett, “A method for determining optimal interelectrode spacing for cerebral topographic mapping,” *Electroencephalography and Clinical Neurophysiology*, vol. 72, no. 4, pp. 355–361, 1989.
- [16] R. Srinivasan, P. L. Nunez, and R. B. Silberstein, “Spatial filtering and neocortical dynamics: estimates of EEG coherence,” *IEEE Transactions on Biomedical Engineering*, vol. 45, no. 7, pp. 814–826, 1998.
- [17] R. Srinivasan, D. M. Tucker, and M. Murias, “Estimating the spatial Nyquist of the human EEG,” *Behavior Research Methods, Instruments, & Computers*, vol. 30, no. 1, pp. 8–19, 1998.
- [18] D. C. Montgomery, *Design and Analysis of Experiments*, John Wiley & Sons, 2008.
- [19] R. Oostenveld and P. Praamstra, “The five percent electrode system for high-resolution EEG and ERP measurements,” *Clinical Neurophysiology*, vol. 112, no. 4, pp. 713–719, 2001.
- [20] B. He, D. Yao, J. Lian, and D. Wu, “An equivalent current source model and Laplacian weighted minimum norm current estimates of brain electrical activity,” *IEEE Transactions on Biomedical Engineering*, vol. 49, no. 4, pp. 277–288, 2002.
- [21] O. Makeyev, Y. Boudria, Z. Zhu, T. Lennon, and W. G. Besio, “Emulating conventional disc electrode with the outer ring of the tripolar concentric ring electrode in phantom and human electroencephalogram data,” in *2013 IEEE Signal Processing in Medicine and Biology Symposium (SPMB)*, Brooklyn, NY, USA, December 2013.
- [22] O. Makeyev, T. Lennon, Y. Boudria, Z. Zhu, and W. G. Besio, “Frequency domain synchrony between signals from the conventional disc electrode and the outer ring of the tripolar concentric ring electrode in human electroencephalogram data,” *2014 40th Annual Northeast Bioengineering Conference (NEBEC)*, 2014, Boston, MA, USA, April 2014, 2014.
- [23] Z. Zhu, J. Brooks, O. Makeyev, S. M. Kay, and W. G. Besio, “Equivalency between emulated disc electrodes and conventional disc electrode human electroencephalography,” *2014 36th Annual International Conference of the IEEE Engineering in Medicine and Biology Society*, 2014, Chicago, IL, USA, August 2014, 2014.
- [24] B. He, Y. Wang, and D. Wu, “Estimating cortical potentials from scalp EEGs in a realistically shaped inhomogeneous head model by means of the boundary element method,” *IEEE Transactions on Biomedical Engineering*, vol. 46, no. 10, pp. 1264–1268, 1999.

## Research Article

# Time-Frequency Linearization of Reactive Cortical Responses for the Early Detection of Balance Losses

Giovanni Mezzina  and Daniela De Venuto 

Department of Electrical and Information Engineering, Politecnico di Bari, Bari 70125, Italy

Correspondence should be addressed to Giovanni Mezzina; [giovanni.mezzina@poliba.it](mailto:giovanni.mezzina@poliba.it)

Received 23 August 2019; Revised 10 November 2019; Accepted 7 December 2019; Published 31 December 2019

Guest Editor: Hassan Mostafa

Copyright © 2019 Giovanni Mezzina and Daniela De Venuto. This is an open access article distributed under the Creative Commons Attribution License, which permits unrestricted use, distribution, and reproduction in any medium, provided the original work is properly cited.

Aiming at finding a fast and accurate preimpact fall detection (PIFD) strategy, this paper proposes a novel methodology that precociously discriminates the occurrence of unexpected loss of balance from the steady walking, by analyzing the subject's cortical signal modifications (at the scalp level) in the time-frequency domain. In this study, the subjects were asked to walk at their preferred speed on the treadmill platform programmed to provide unexpected bilateral slippages. The proposed PIFD method exploits synchronously recorded electromyographic (EMG: 2 channels from the same lower limb muscle bundle, bilaterally) and electro-encephalographic (EEG: 13 channels from motor, sensory-motor and parietal cortex areas) signals. To validate the method offline, also, the lower limb kinematics has been reconstructed via a motion capture system (23 reflective markers and 8 fixed cameras). During the PIFD system functioning, the EMG signals from the lateral gastrocnemii are first translated in a binary waveform and then used to trigger the EEG analysis. Once enabled via EMG (every gait cycle), the EEG computation branch extracts and linearizes the rate of variation in the EEG power spectrum density (PSD) for five bands of interests:  $\theta$  (4–7 Hz),  $\alpha$  (8–12 Hz),  $\beta$  I,  $\beta$  II,  $\beta$  III rhythms (13–15 Hz, 16–20 Hz, and 21–28 Hz). The slope of the linearized trend identifies, in this context, the cortical responsiveness parameter. Experimental results from six subjects revealed that the proposed system can distinguish the loss of balance with an overall accuracy of ~96% (average value between sensitivity and specificity). The discrimination process requests, on average, 370.6 ms. This value could be considered suitable for the implementation of countermeasures aimed at restoring the balance of the subject.

## 1. Introduction

The World Health Organization (WHO) statistics demonstrated that falls are a common occurrence and a serious health issue for the general population. In fact, in 2019, only in the United States, 29 million of falls have been recorded, resulting in 7 million of invalidating injuries. Moreover, it has been estimated that every 19 minutes an older adult die from a fall, while every 11 seconds an older adult is treated in the emergency room for the same reason. According to the Centers for Disease Control (CDC), falls are the leading cause of fatal injury among old adults and the most frequent reason for nonfatal trauma as well [1, 2]. These statistics support the clinical evidence according to which the natural aging process would alter the abilities to face the unexpected perturbations of the balance through the compensatory and

anticipatory countermeasures [3, 4]. In this respect, the fall detection (FD) context arises with the main objective of creating systems, or devices, capable of detecting the fall events automatically in a short time and with good accuracy.

The first classification of FD strategies divides the algorithms into two macroareas: Postfall Mobility Detection (PFMD) and Preimpact Fall Detection (PIFD) algorithms.

The algorithms from the first macroarea (i.e., PFMD) detect the fall events when they already occurred. Typically, they assess the posthumous state of the subject mobility. The paradigm of these systems is as follows: (1) identify the fall, (2) evaluate the user mobility, and (3) call the assistance to avoid death due to “long-lie” phenomenon [5, 6] (the “long-lie” concerns the inability of elderly people to get up again after a fall event). The PFMD architectures present an intrinsic limitation: falls can only be detected as a result of

body-ground impacts; thus, it is not possible to prevent injuries directly caused by impacts. This limit can be overcome by using PIFD strategies [7, 8]. The PIFD architectures exploit techniques capable of recognizing the fall event before the body impacts in a disruptive manner with the ground [7].

Different from the PFMD techniques, the PIFD strategies require very short time to detect a fall event, trying to keep high accuracies in the fall recognition. Indeed, these strategies are designed and developed to be integrated into a closed-loop control system with on-demand fall protection devices or support for postural control. Although these systems are still under investigation and not already available on the market (if not for research purposes), the idea of merging PIFD strategies and protection countermeasures is considered a promising solution in the field of fall prevention [8]. Table 1 provides a detailed overview of PIFD strategies and solutions at the state of the art. The table shows, for each considered article, the technology used to collect data for the fall detection implementation, the fall indicators, the classification method, the type of analyzed falls, and the performance in terms of sensitivity (Se), specificity (Sp), and average detection time (DT).

The devices used to detect fall early can be classified as context-aware devices or wearable devices. Among the works analyzed in Table 1, three studies [9–11] are based on context-aware technologies and coincide with those related to the recognition of falls from induced slipping. These studies use motion capture systems (MCS) as the main acquisition devices. MCS analyze kinematic determination by means of reflective markers placed on specific anatomical reference points of the human body. The trajectories of the markers are therefore traced by cameras mounted in fixed positions. The main pros of using MCS are that the fall indicators can be determined with extreme precision [7, 8, 12], while the main cons are the costs and the limited operating volume that can be framed by the cameras.

Table 1 presents some studies in which the detection of falls is made using a single type of wearable sensor [13–15]. The use of a single type of sensor has the advantage of significantly reducing the complexity and the computational request of the PIFD system [8]. Nevertheless, it has been demonstrated that, at present, the only acceleration signals do not allow to discern the phenomena of loss of equilibrium from activities like falls (e.g., running or jumping) [16]. Inertial measurement units (IMUs) solve the problem thanks to the simultaneous embedding of triaxial accelerometers and gyroscopes. Another interesting PIFD strategy is the one proposed in [17–22]. The authors propose a fully physiological signal-based cyber-physical system for fall detection. It consists of a wearable and wireless acquisition interface that exploits data from EEG and EMG.

The classification methods in Table 1 can be divided into the following: single and multiple threshold-based algorithms, machine learning-based approaches, or statistical models. Among the analyzed methods, the threshold algorithms are certainly the simplest in many aspects. Threshold-based algorithms are generally computationally efficient, suitable in real-time PIFD applications. Despite a fast detection, in most cases, these approaches provide accu-

racy below the 90%. To improve the PIFD strategy discrimination capability, realizing more efficient threshold-based systems, several solutions use ML methodologies [10, 14, 23]. Nevertheless, the ML algorithms request for a prolonged classifier training period. The authors in [17] analyze EEG and EMG signals by means of a logic-based matchmaking algorithm, which allows fast classification of the no voluntary movements. It is noteworthy that most of the solutions in Table 1 analyze simulated falls (SF), in which the subjects were asked to fall voluntarily or with specific postures. However, most real-life fall events occur due to unexpected perturbations and are characterized by an involuntary nature.

The performance of a PIFD strategy can be expressed in terms of accuracy and efficiency. The accuracy is defined by two parameters: sensitivity and specificity. Commonly, the sensitivity parameter is defined by the ratio between the number of correctly recognized fall events and the total number of evaluated falls. Similarly, the specificity can be defined as the ratio between the amount of successfully detected activities not identifiable as falls (e.g., walking steps) and the total number of these activities. The strategy efficiency is, instead, evaluated in terms of detection time, which is the time range from the perturbation initiation and the fall event recognition.

Ultimately, in terms of performance, Table 1 shows that the sensitivity of the proposed solutions ranges between 88% and 100% ( $95.21 \pm 4.81\%$ ), while the specificity one between 88.5% and 100% ( $94.59 \pm 5.14\%$ ). Data shows that the greatest problem of the proposed solutions (in term of accuracy) is related to the high number of false alarms, which reduce the specificity of the PIFD systems. It leads to overall system accuracies of  $94.9 \pm 4.01\%$ . Since the compensating actions related to the output of the PIFD strategy must be designed to avoid the falls, the detection times must be accurately estimated to demonstrate the temporal compliance of the system. In this respect, the authors in [24] set a detection time of 550 ms as the maximum intervention limit for the implementation of countermeasures aimed at restoring the balance of the subject. Data in Table 1 show that the detection time settles at around  $559 \pm 153.77$  ms and, among the evaluated works, only the systems proposed in [10, 11, 15] provide detection times lower than the threshold of 550 ms, paving the way to their possible use in strategies for postural recovery. Other solutions are, instead, typically used to trigger total body or hip airbag-based protection systems, which can reduce the extent of the body-ground impact (that evolves in 700 ms-1000 ms).

In this context, the here proposed work is aimed at addressing the following challenges:

- (i) To create a low compute-intensive algorithm that can analyze in time and frequency domain the reactive cortical dynamics (at the scalp-level) involved in balance adjustments when the steady walking is suddenly perturbed by slippages
- (ii) To design a method to reach high values of accuracy (>95%), while maintaining detection time under the limit imposed by authors in [24]: 550 ms



TABLE 1: Overview PIFD strategies at the state of the art.

Ref.	Technology	Fall indicators	Class. Algorithm	Fall type	Performance
[13]	Trunk-positioned 3D ACC	Trunk vertical velocity (TVV)	Single Thr: TVV > 1.3 m/s	n. 3 SF: FwF, BwF, SdF	Se (%) = 100 Sp (%) = 98.27 DT (ms) = 577.00
[25]	Waist-positioned 3D GYR and ACC	Waist vertical velocity (WVV)	Single Thr:  WVV  > max WVV in nonfall activities	n. 4 SF: FwF, BwF, SdF, OrF	Se (%) = 100 Sp (%) = 100 DT (ms) = 675.15
[26]	9DoF IMU by Xsens Tech. positioned on chest	Acceleration and angular velocity of the chest segment	Multiple Thr: (1) acc. > 7 m/s <sup>2</sup> (2) ang. velocity > 3°/s	n. 3 SF: FwF, BwF, SdF	Se (%) = 89.5 Sp (%) = 91.6 DT (ms) = 617.35
[14]	Trunk-positioned 3D ACC	Acceleration Time Series (ATS) of the chest	ML: (1) The extracted ATS trains a HMM (2) The HMM outcome is compared with a single Thr	n. 2 SF: FwF, SdF	Se (%) = 100 Sp (%) = 88.75 DT (ms) = 598.40
[23]	Waist-positioned 3D GYR and ACC	Acceleration and angular velocity of the waist segment	ML: (1) Mean and variance of the $x, y, z$ axis acceleration and angular velocity (2) Classification by SVM	n. 4 SF: FwF, BwF, SdF, falling from sit IF: slip-induced fall	Se (%) = 93.5 Sp (%) = 85.6 DT (ms) = 775.20
[17]	EEG wireless headset+surface EMG	EEG Power Spectrum Density (PSD) level in BP, $\mu$ , $\beta$ rhythms	Multiple Thr: (1) The EMG is used as a trigger for cortical analysis (2) The EEG PSD is evaluated in BP, $\mu$ , $\beta$ bands (3) The levels are compared with history-based thresholds	n. 1 SF: BwF IF: loss of balance on weighbridge	Se (%) = 90 Sp (%) = 87 DT (ms) = 168 (from gastrocnemius contraction)
[9]	MCS: total body monitoring	Acceleration and vertical velocity of upper arms, trunk, tibia, and head	Multiple Thr+statistical model: threshold based on a ARIMA model based on data history	IF: slip-induced fall	Se (%) = 88.5 Sp (%) = 92.9 DT (ms) = 680.00
[10]	MCS: total body monitoring	Acceleration of all the monitored body segments	ML: (1) The accelerations are analyzed by ICA (2) A neural network is used to distinguish walk from perturbations	IF: slip-induced fall	Se (%) = 92.7 Sp (%) = 98 DT (ms) = 351.00
[11]	MCS+trunk-positioned IMU sensor	Sagittal angle and angular velocity of the trunk	Multiple Thr+statistical model: threshold based on a AR model based on data history	IF: slip-induced fall	Se (%) = 100 Sp (%) = 96.5 DT (ms) = 355.00
[15]	Hip encoder on active pelvis orthosis	Hip angle	Single Thr: increment of the error function between the current hip angles (from encoder) and the ones provided by a pool of adaptive oscillators	IF: slip-induced fall	Se (%) = 92.7 Sp (%) = 98 DT (ms) = 403.00

Technology acronyms—ACC: accelerometer; GYR: gyroscope; MCS: motion capture system; IMU: inertial measurement unit; DoF: degree of freedom. Class. algorithm acronyms—Thr: threshold; ML: machine learning; HMM: Hidden Markov Model; SVM: support vector machine; BP: Bereishaf potential (EEG); ARIMA: autoregressive integrated moving average; ICA: independent component analysis; AR: autoregression. Type of fall acronyms—SF: simulated fall; IF: involuntary fall (unexpected); FwF: forward fall; BwF: backward fall; SdF: lateral fall; OrF: fall from orthostatic position.

(iii) To realize a first-of-a-kind *fully* wearable sensor-based PIFD strategy in slippage recognition, which is typically entrusted to MCS

In this respect, the proposed study investigates changes in the cortical involvement when subjects were actively managing unexpected slippages delivered during steady walking. The proposed method synchronously records electrophysio-

logical signals from 2 EMG electrodes placed bilaterally on the gastrocnemii and 13 EEGs along motor, sensory-motor, and parietal areas. The EMG signals from the lateral gastrocnemii are the first 1-bit digitized and then used as a trigger for the EEG analysis. During the cortical analysis, the system extracts the variation in the EEG power spectrum density for five bands of interest (i.e.,  $\theta$  (4–7 Hz),  $\alpha$  (8–12 Hz),  $\beta$  I,  $\beta$  II, and  $\beta$  III rhythms) (13–15, 16–20, and 21–28 Hz) by using



the sliding window Fast Fourier Transform (FFT). The trend is then approximate by using a linear data fitting. The slope of the resulting linearized trend,  $m$ , identifies an approximate version of the clinical cortical responsiveness parameters.

Experimental results from six young and healthy subjects revealed a nonlateralized sharp increment of  $m$  just after the onset of the perturbation. Furthermore, the results show an interesting and concrete possibility of detecting the loss of balance induced by slips with good precision (96.02%) and with detection times shorter than the average of the state of the art ( $370.62 \pm 60.85$  ms).

The paper is organized as follows: Section 2 briefly defines the medical background, to facilitate the understanding of the detailed methodological bases of the algorithm. Section 3 discusses the experimental results providing a complete comparison with the state of the art, and Section 4 concludes the paper, presenting future perspectives.

## 2. Materials and Methods

**2.1. Medical Background: Reactive Cortical Dynamics.** Recent studies [27–36] have shown how the cerebral cortex regulates the excitability of subcortical postural centers to maintain the postural stability according to environmental demands [28]. Several studies on EEG signals [27–35] analyzed the cortical involvement in balance control. Typically, they focused on the study of event-related potentials (ERPs) elicited by mechanical perturbations of the subjects' balance. The proposed studies treated cortical reactions when the perturbations are provided to orthostatic posture [28, 29].

Few studies provided results about the reactive control spectral analysis [30–35]. They revealed important correlations among specific oscillatory rhythms, cognitive functions, and sensorimotor ones. Briefly, it has been proved [32, 33] that low-frequency cortical rhythms (<13 Hz) are related to perception and cognitive control. In a fall event context, the modulation of these oscillatory rhythms can be related to the visual field stabilization and active decoding of data coming from the vestibular system. Typically, these rhythms start oscillating in the first phase of the fall, involving the bands of interest:  $\theta$  and  $\alpha$ .

In a chronological order, the cortical involvement proceeds with the modulation of high-frequency cortical rhythms (>13 Hz). The latter are related to motor functions and in particular to the active concentration of the subject in muscle firing operations for the compensatory actions [34, 35]. According to the application-specific bands of interest, in this category, we consider the  $\beta$  bands (i.e.,  $\beta$ I,  $\beta$ II, and  $\beta$ III). The power increase in the above-mentioned bands must be analyzed carefully. In fact, even during walking, cortical dynamics present significant impulses in the motor cortex side opposite to the leg muscles in the swing phase. Nevertheless, it is expected that the responsiveness of cortical activity observed during walking is, in any case, lower than the one expected during the postural recovery phase. Moreover, since the  $\beta$  bands are linked to the planning of sudden and precise changes, they are expected to not intervene in situations of unperturbed walking. Under this hypothesis, the power level in these bands could be consid-

ered one of the most discriminating parameters in the context of fall recognition.

**2.2. Experimental Setup.** The main goal of the study is to analyze the subjects' cortical reactive dynamics when during a steady walk (at their preferred speed) the balance is suddenly perturbed by unexpected bilateral slippages. In this respect, during the experimental trials, participants wore a 32-channel wireless EEG headset (g.Nautilus Research by g.Tec) and 2 wireless EMG surface electrodes (Cometa Wave Plus by Cometa Systems) as shown in Figure 1.

Table 2 provides information about the adopted acquisition equipment (i.e., EEG and EMG). For each device, the table reports the number of monitored nodes or channels, equipment features such as the size and weight, and the electrode characteristics and acquisition parameters: resolution and sampling frequency.

Thirteen EEG sites were monitored: F3, Fz, F4, C3, Cz, C4, Cp5, Cp1, Cp2, Cp6, P3, Pz, and P4, according to the international 10–20 system [37]. The O2 electrode was used for noise suppression, AFz as ground, and A2 (right earlobe) as the reference electrode. The EEG data were sampled at 500 Hz with 24-bit resolution [37].

Ten surface EMG channels were monitored from the following bilateral muscle groups: anterior tibialis, lateral gastrocnemius, vastus medialis, rectus femoris, and biceps femoris. The EMG signals were recorded with a sample rate of 2048 Hz and down sampled to 500 Hz (16-bit resolution) to match the EEG signal sampling frequency [22]. In this study, only EMG signals related to the lateral gastrocnemius were retained (two EMG surface electrodes).

Both EEG and EMG were transmitted via Bluetooth Low Energy (BLE) protocol to a dedicated gateway and collected by a Simulink model.

Figure 1, supported by data in Table 2, demonstrates the low encumbrance of the final architectures. The choice of fully wireless and light acquisition devices makes the preimpact fall detection architecture wearable. Despite this, since the use of gel-based or pregelled electrodes could not be considered comfortable, different solutions are still under investigation.

Figure 1 also shows a set of 23 reflective markers for the 3D kinematics reconstruction placed on the subjects' lower limbs and 8 cameras. Specifically, spherical markers ( $d = 14$  mm) were mounted bilaterally on anterior superior iliac spines, sacrum, prominence of the greater trochanter external surface, lateral and medial epicondyle of the femurs, heads of fibula, lateral and medial malleolus, calcaneus, and first and fifth metatarsal heads. Additional markers were rigidly placed on wands over the midfemurs and midshaft of the tibia. It is important to stress that the MCS-oriented markers are only used for temporal coherence validation of the EEG/EMG signals and they are not part of the proposed architecture. In fact, kinematic records, electrophysiological signals, and the onset of the perturbation were synchronized offline on the same timeline for the system validation.

**2.3. Experimental Protocol.** During the experimental trials, subjects were asked to manage unexpected slippages while

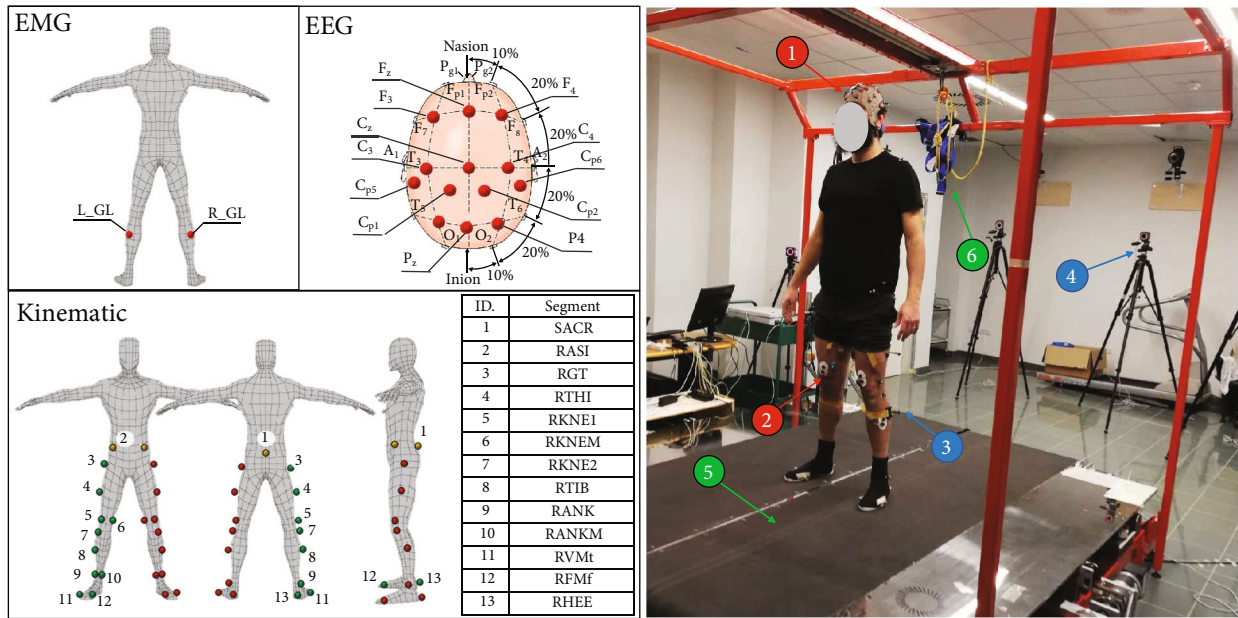


FIGURE 1: Experimental setup. The perturbation platform (SENLy) and a subject under test. On the figure, labels refer to the following: the wireless EEG headset (red: #1), the wireless surface EMG electrodes (red: #2), the set of markers (blue: #3), the motion analysis system camera (blue: #4), the perturbation platform SENLy (green: #5), and a safety harness (green: #6).

TABLE 2: EEG/EMG acquisition device features.

Sig.	Num.	Equipment features	Size (mm)	Electrode Type	Resolution	Sampling frequency
EEG	13 channels	EEG headset station: 70 × 55 × 30 mm Weight: 145 g Wireless 10 h continuous acquisition at 500 Hz	16 × 10 × 5	Active Gel based Sintered Ag/AgCl probe	24 bits	500 Hz
EMG	2 nodes	EMG single node: 33 × 23 × 19 mm Weight: 12 g Wireless 12 h continuous acquisition at 2048 Hz	18 × 12 × 5	Active Pregelled sintered Ag/AgCl holder ring	16 bits	2048 Hz ↓ 500 Hz

walking at their self-selected speed on a mechatronic platform named SENLy [38] (Figure 1—label #5). For safety reasons, the volunteers were secured by a harness attached to an overhead track.

SENLy is a platform designed to destabilize the balance control during motor tasks [38–40]. It consists of a split-belt treadmill, in which belts can be moved in the horizontal plane, both longitudinally and transversally. The platform is equipped with force sensors to identify the phases of the gait cycle during walking [40].

In the present study, the perturbations provided by SENLy consisted of sudden forward movements toward the anterior-posterior direction. Specifically, the selected belt was accelerated and decelerated up to the belt stop with a triangular speed profile (slope  $8 \text{ m/s}^2$  for a total displacement of

0.15 m). The belt movement was triggered by detecting the heel strike of the foot appointed for the perturbation.

After the first acclimation phase (~5 min), the protocol consisted of a series of 10 consecutive trials in which the subject gait was perturbed by a slippage. The slippages were equally delivered alternating right foot-related belt and the left foot one.

**2.4. The Preimpact Fall Detection Strategy.** The work proposes an innovative solution in the field of PIFD strategies, whose primary goal is the real-time detection of a loss of balance through the synchronized analysis of physiological signals (i.e., EEG and EMG).

The block diagram in Figure 2 provides a general overview of the implemented architecture.

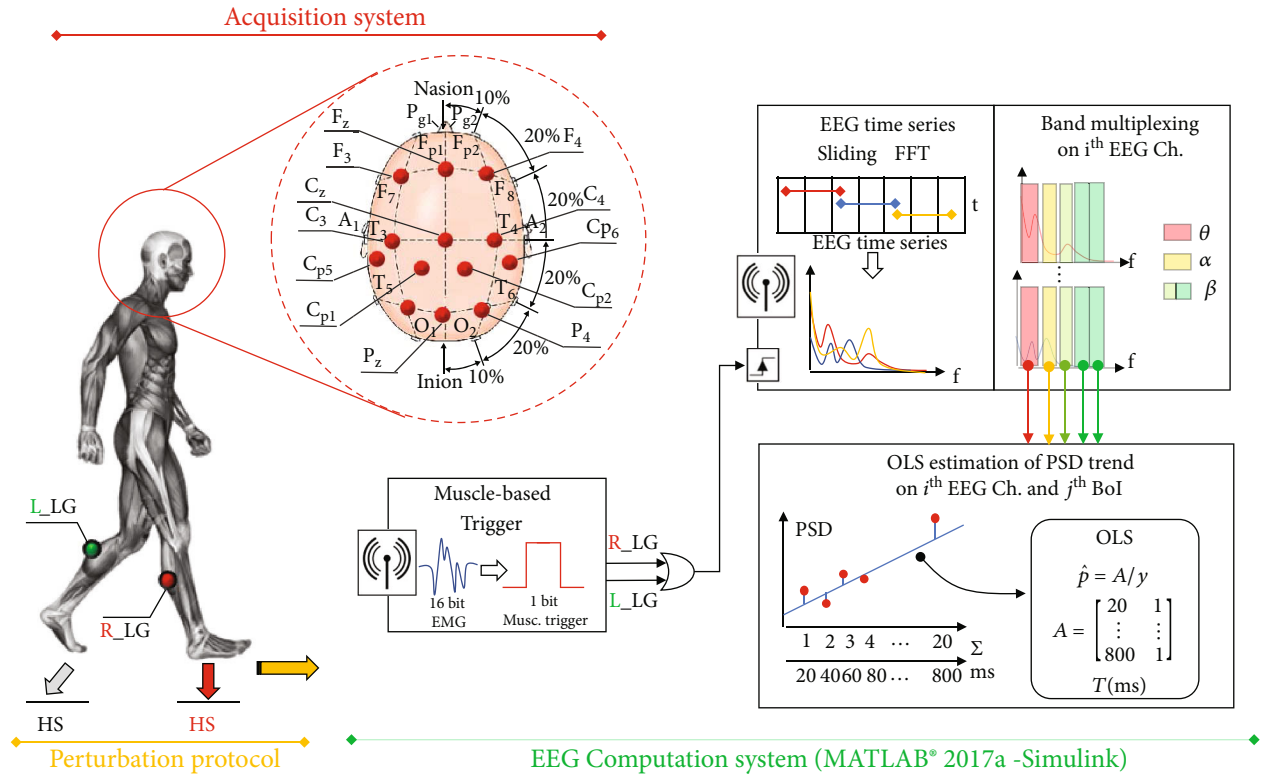


FIGURE 2: Overview of the proposed PIFD architecture. The block diagram recaps all the main procedure steps from signal acquisition to the PSD linear fitting extraction, which leads to final discrimination.

As shown in the figure, the system is composed of the three main parts: the acquisition system, the perturbation protocol, and the computing unit. The latter can be further divided in the EMG processing (i.e., Muscle-based Trigger) and the cortical analysis block that comprises the sliding window FFT, the band multiplexing process, and the ordinary least square (OLS) estimation of the power spectrum density trend.

From Figure 2, it is possible to notice how this architecture has been optimized and validated for the recognition of balance losses induced by SENLY as unexpected slippages (perturbation protocol—Figure 2).

As detailed in Section 2.2, the acquisition system in Figure 1 consists of an architecture that acquires and synchronizes EEG and EMG signals. Specifically, the system monitors 2 surface EMG surface electrodes placed on the lateral gastrocnemii (R(L)\_LG—Figure 1) and thirteen EEG channels distributed between motor, sensorimotor, and parietal cortex. The acquired physiological signals (i.e., EEG and EMG) are then wirelessly transmitted to a common gateway that deals with synchronizing, in real time, the data coming from the two different acquisition systems.

In this work, the gateway consists of a receiving station connected, via USB, to a laptop on which a dedicated real-time Simulink-MATLAB®2017a model is running.

The Computing System working principle can be described as follows: The collected EMG signals are wirelessly sent to the first block (i.e., the Muscle-based Trigger) that translates the electrophysiological activity into binary

signals. The trigger algorithm analyzes sample-by-sample the EMG, associating the value “1” to a contracted muscle, otherwise the value “0,”

This process of muscle activity digitization is entrusted to a moving average approach, which is able to adapt to changes in the subject’s muscle tone [22]. These two binary waveforms are then used to independently trigger the cortical analysis. In this context, it was useful to identify a specific phase of the step cycle in which to activate the cortical analysis. This choice allows the system to exclude, from the total computation, the cortical activity that is not strictly linked to the specific movement, reducing the amount of data to be analyzed and possible occurrences of false alarms in the electroencephalographic profile. The trigger associated with this muscle is named Master Trigger (MT) in the following. We selected lateral gastrocnemius as MT because it uniquely identifies the double support phase of the gait cycle.

As previously stated, the rising edge of the MT enables the cortical analysis at every step (i.e., right and left gastrocnemius contraction independently). The EEG computing block quantifies the rate of variation in the power of brain signals, considering five interest bands by means of a sliding window FFT. Each window returns a power value in each evaluated band, building five vectors of measurements, named—for the reasons of generality—“ $y$ ” in Figure 2. Then, the algorithm extracts, for each vector  $y$  a linear approximation of the PSD via ordinary least square (OLS) estimation. These models allow the system to extract, from the PSD measurement ( $y$ ), two parameters ( $\hat{p}$ ) via the matrix of base

function (A): the intercept and the slope of the resulting linearized PSD trend. The EEG responsiveness parameter practically consists in the slope. The EEG responsiveness parameters, extracted via linear models, contribute to the system calibration phase. In this stage, the system defines statistics-based models to identify the “standard” cortical behaviors.

During this phase, the implemented algorithm extracts a sequence of thresholds. The latter are then used to identify and classify all the statistically “nonstandard” behaviors (including the potential loss of balance) during the real-time operations. This classification phase is carried out by relating, among each other, the thresholds through a network of logical conditions. The network closes the processing, providing in the output the result of the binary classification: unperturbed step or potential loss of balance. If the output of the logical network is supplied in a time that is consistent with the fall dynamics, the system alert can be used to enable postural recovery strategies.

*2.4.1. Data Preprocessing.* The here-proposed system online treats the electrophysiological signals (i.e., EEG and EMG) following the following guidelines:

(1) *EMG.* Surface EMGs were on-line high-pass filtered with an 8th order Butterworth filter with cut-off frequency at 10 Hz to reject movement artifacts.

(2) *EEG.* According with the main studies in the field [28, 29, 36], the EEGs were progressively band-filtered between 1 Hz and 40 Hz by using an 8th order Butterworth filter before the transmission.

During every trial, an impedance check of all EEG electrodes was carried out in order to ensure a value lower than 40 k $\Omega$ .

A numeric notch filter (48-52 Hz) was implemented for both EEG and EMG signals.

(4) *Special Precautions.* EEG artifacts can be classified, in general, as physiological or non-physiological [41]. The former type includes eye movement (blinking, lateral and vertical movement), muscle contraction (tightening of the jaw, contraction of the neck muscle), and cardiac artifacts. The non-physiological artifacts include line noise, impedance shift, and interference from cable movement [41]. The acquisition of EEG signals during the gait increases the influence of these artifacts. Although there is no way to permanently delete all the above-mentioned artifacts, special precautions were taken during the recording sessions to limit their effects.

The use of active preamplified wet electrodes, with impedance check and fixing procedures of the electrode by PCB connection lines, guaranteed the attenuation of non-physiological artifacts. Moreover, in the experimental tests, the subjects were asked to fix their gaze on a frontal area at the eye level and to relax neck muscles during the experiment, avoiding, as far as possible, turning or swinging the head while walking.

To limit further confounding effects, the ambient lighting was kept constant, the ambient noise was reduced, and recording equipment and operators were kept out of the field of view.

The remaining artifacts will be rejected in the cortical analysis phase by embedding in the Simulink model an artifact rejection stage: the Riemannian Artifact Subspace Representation (rASR) method [42].

*2.4.2. Muscle-Based Trigger Generation.* As shown in Figure 2, the Muscle-based Trigger block is used to identify the onset of the contraction event for a specific muscle. For the particular application, in-depth knowledge of the EMG signal level is not as useful as knowing its binary approximation (e.g., ON/OFF). Although the ON/OFF condition conceptually and computationally simplifies the analysis of EMG signals, the algorithm of extraction of muscle triggers, presented in principle in Figure 3, must be able (i) to adapt to the characteristics of the muscle tone of the subject under test (intersubject variability) and (ii) to follow muscle tone changes during the trial.

In this respect, for this application, we refer to a method proposed in our previous works [22, 43] previously used in gait analysis applications. Briefly, it consisted of a dynamic threshold approach, in which each EMG signal (16-bit) was converted in a binary signal (named trigger). It assumes a logic value HIGH if the muscle is contracted, low otherwise (relaxed muscle). Figure 3 shows all the steps for the trigger generation.

The method, here, described in principle, compares the average of the signal power on a large time span of  $M = 500$  ms (PM) and the signal power average on a shorter time span of  $N = 250$  ms (i.e., the last 250 ms of the  $M$  register, PN). The process was refreshed sample-by-sample.

For the  $i$ th sample, PN was compared with the PM. If  $PN > PM$ , the trigger goes 1, otherwise 0.

*2.4.3. The Cortical Analysis System.* In this context, it has been experimented that the selected MTs (lateral gastrocnemii) typically react in  $323.19 \pm 52.38$  ms to the slippages. From literature [36], we know that  $\theta$  is the faster band (temporally) in intervening with a power variation (peak detectable at  $\sim 185$  ms from perturbation onset) and therefore the most critical to be reconstructed, in the perspective of a fitting with a linear model enabled by MT.

In this respect, in this study, the system extracts an EEG time window that starts at 800 ms (i.e., 400 samples) before and ends at the MT contraction onset. As previously stated, the EEG subsets undergo the first stage of artifact rejection via rASR. The artifact-free EEG subset is then split in 20 overlapped (10-sample step) 200-sample long time windows.

On each evaluated time window, the system operates an FFT with a spectral resolution of 2.5 Hz ( $f_{\text{sEEG}} = 500$  samples/s,  $L_{\text{win}} = 200$  samples). The spectral behavior is then evaluated according to

$$Y = \left| \frac{\text{FFT}(s_w)}{L_{\text{win}}} \right| \rightarrow S = 2 \cdot Y \left( 2 : \frac{L_{\text{win}}}{2} \right), \quad (1)$$



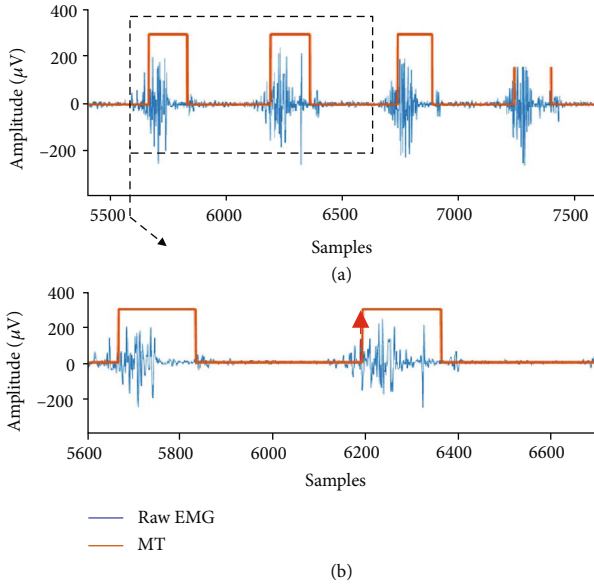


FIGURE 3: Overview of the muscle trigger extraction technique: (a) the Master Trigger (MT) is extracted from the raw EMG data; (b) detail of MT onset (red arrow).

where  $s_w$  is the 200-sample long sliding window to be evaluated and  $L_{win}$  is the number of samples that composes the analyzed data series. Once the spectral power  $\mathbf{S} \in \mathbf{R}^{L_{win}/2}$  for each window has been extracted, the system starts with the band multiplexing phase according to Figure 2 [44, 45]. During the band multiplexing stage, the system extract the behaviors of  $\theta$  (4–7 Hz),  $\alpha$  (8–12 Hz) bands and the  $\beta$  I,  $\beta$  II, and  $\beta$  III (13–15, 16–20, and 21–40 Hz) rhythms taking into the account the spectral resolution. In this respect, for every analyzed window, the system extracts the vector  $\mathbf{S}_{BoI} \in \mathbf{R}^{nBoI}$ , with  $nBoI = 5$ , the number of bands involved in the multiplexing. This vector (i.e.,  $\mathbf{S}_{BoI}$ ) consists of the sum of all the spectral contributions falling within the range of the analyzed band, according to

$$\mathbf{S}_{BoI} = \begin{bmatrix} \theta \rightarrow \sum_2^3 (S(i)) \Big|_{dB} \\ \alpha \rightarrow \sum_3^5 (S(i)) \Big|_{dB} \\ \beta I \rightarrow \sum_6^7 (S(i)) \Big|_{dB} \\ \beta II \rightarrow \sum_8^{10} (S(i)) \Big|_{dB} \\ \beta III \rightarrow \sum_{10}^{16} (S(i)) \Big|_{dB} \end{bmatrix} \in \mathbf{R}^{nBoI,1}. \quad (2)$$

Ultimately, in correspondence of the MT contraction,

- (1) The system extracts the vector  $\mathbf{S}_{BoI}$  (equation (2)) for all the 20 sliding widows composing the EEG chunk to be analyzed
- (2) All the vectors are embedded in a 2D matrix with a size of  $20 \times nBoI$ . Each column of this matrix recaps, in 20 points, the power spectrum measurements of a specific BoI in the 800 ms preceding the MT onset
- (3) The computation is then extended to the monitored channel ( $nCh = 13$ ), resulting in a 3D matrix  $\mathbf{MS}_{BoI} \in \mathbf{R}^{20, nBoI, nCh}$

Considering, for the sake of clarity, a single band of interest and a channel, the measurements related to the 20 windows are finally sent to a computation unit that deals with extracting linear models by means of least-square fitting (i.e., OLS estimation). In particular, this stage of cortical responsiveness computation is based on the simplified approximation that the brain response, described by 20 points, could be considered a straight line  $x(t) = m \cdot t + q$ .

Figure 4 shows a demonstrative and emphasized comparison (by referring to experimental basis), between a linear model extracted during walking (Figure 4(a)—blue) and a linear model from a reactive response to a perturbation (Figure 4(b)—red). Both the panels refer to channel F3 and the same band of interest (i.e.,  $\alpha$ ). Data related to walking (Figure 4(a)) refer to MT onset #16 of the Sub. 4-Trial 2. The MT associated with the selected contraction was left gastrocnemius (ipsilateral to F3).

As the final step, system discards the information considered useless in this context, such as the estimated intercept, deriving a matrix that contains only the estimated slopes,  $\hat{m}$ . For each MT contraction, a 2D matrix is defined:  $\mathbf{M} \in \mathbf{R}^{nBoI, nCh}$ , whose elements  $m_{j,i} = \hat{m} \Big|_{jBoI, iCh}$  are the slope estimation of the above-described OLS-based model in the  $j$ th band of interest and  $i$ th channel. For example, in Figure 4, the degree of cortical responsiveness was extracted by the system in the case of unperturbed gait (MT #16) is  $\hat{m} \Big|_{\alpha, F3} = 0.0125$  dB/ms; similarly, in the case of perturbation (MT #41), this parameter is  $\hat{m} \Big|_{\alpha, F3} = 0.25$  dB/ms. Note that the  $x$ -axis reports the window number, and each window consists of a 20 ms step.

**2.4.4. Logical Classifier.** As stated in Section 2.4.3, the cortical analysis system extracts the cortical responsiveness matrix  $\mathbf{M}$  for each evaluated contraction of the MT.

In the first calibration phase, the system collects several  $\mathbf{M}$  matrices from unperturbed walking steps. Thus, it builds a statistic of the “standard” cortical behavior for the subjects under test.

More in detail, the system calibration requires the storage of the  $\mathbf{M}$  matrices for a number,  $Nc$ , of unperturbed MT contractions. Once this data collection is over, a 3D matrix  $\mathbf{MC} \in \mathbf{R}^{nBoI, nCh, Nc}$  is available for further computation. The general  $\mathbf{MC}$  element,  $\hat{m}_c(j, k, i)$ , represents the  $\hat{m}$  value in the  $j$ th band of interest and  $k$ th channel extracted in correspondence of a generic  $i$ th MT contraction. By isolating the channel and band of interest data from the 3D cortical



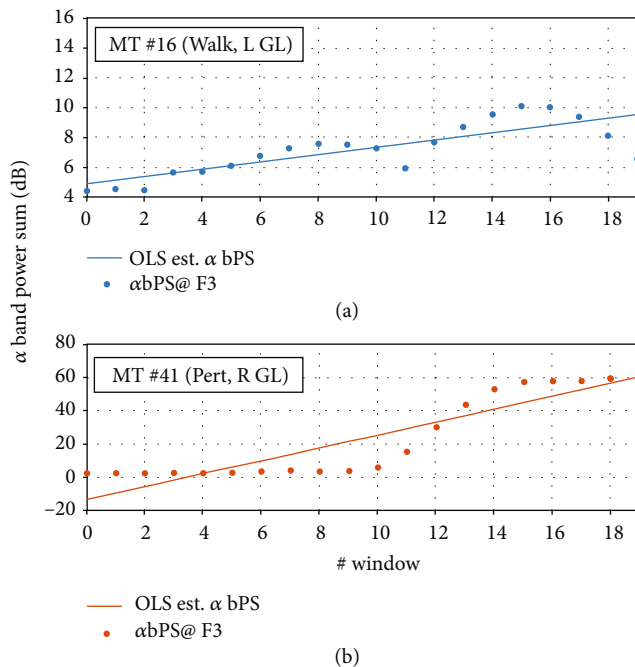


FIGURE 4: Comparison between OLS estimates of the sum of the powers in the  $\alpha$  band in case of fluid walking (a) and perturbed one (b). Data refer the F3 channel.

response matrix (i.e., by selecting the  $k$ th channel and the  $j$ th band), it is possible to extract 65 vectors of size  $\{1 \times N_c\}$ . The 65 vectors extracted from the EEG branch of the architecture are then subjected to a *generalization* step, in which the system averages, on several channels, the values of  $\hat{m}$  in a specific band. The resulting average constitutes groups of EEG channel called functional cortical groups. There are four functional cortical groups that roughly identify the monitored macroareas:

- (i) Supplementary Motor Area. There are  $nBoI = 5$  vectors, one per each band of interest, that include the  $\hat{m}$  value averaged on the channels: {F3, Fz, F4}
- (ii) Motor Area. There are  $nBoI = 5$  vectors, one per each band of interest, that include the  $\hat{m}$  value averaged on the channels: {C3, Cz, C4}
- (iii) Sensory-Motor Area. There are  $nBoI = 5$  vectors, one per each band of interest, that include the  $\hat{m}$  value averaged on the channels: {Cp5, Cp1, Cp2, Cp6}
- (iv) Parietal Area. There are  $nBoI = 5$  vectors, one per each band of interest, that include the  $\hat{m}$  value averaged on the channels: {P3, Pz, P4}

This step of generalization allows the system to obtain an immediate control on the general subject's cortical involvement status. Once the control structure has been made unambiguous by the generalization step, the calibration algorithm must statistically analyze only 20 vectors ( $5 BoI * 4$  functional groups). From these vectors, the system extracts the same number of thresholds based on percentile

analysis. Specifically, all the thresholds coincide with the 95<sup>th</sup> percentiles of the analyzed vector. These thresholds are used to determine the initial state of the system (calibration). At the first contraction of the MT, the threshold will be updated by discarding the first value (the oldest in chronological order) and replacing it with the new one. In consideration of this last vector, the thresholds will be cyclically updated. Once the system is progressively recalibrated, the classifier analyzes the contribution of each functional group to the overall involvement.

The pseudocode in Pseudocode 1 summarizes and widely comments the routines of classification and the calibration considering a single band of interest.

More in details, according to row 1 the system compares the  $\hat{m}$  values of each functional group (imX, with X acronym of the group) with the dedicated threshold (ThrX, with X acronym of the group). Then, if  $>50\%$  of the evaluated groups are interested in a power increase in the cortical activity, a generalization flag (Gen\_flag) is set to 1. The condition opens a second nested routine, the lateral\_check one (row 5). This routine evaluates if the power increment interests only one side of the cortex (by means of the difference among  $\hat{m}$  values from left side channels and right side ones). If the difference is below a certain tolerance, the lateralization flag (Lat\_flag) is set to 1, indicating that the increase is widespread. If both the generalization and lateralization flags are set the system call the Alarm\_on\_BoI routine. It means that on the specific band of interest (e.g.,  $\alpha$ ) the cortical activity is abnormal. If at least 3 bands of interest are interested in the widespread increase, the classification releases a global alarm, asking for an external intervention to restore the balance (potential fall detected).

### 3. Experimental Results

**3.1. Participants.** The fall detecting system has been validated on six young and healthy subjects, whose personal data and anthropometric measurements (mean  $\pm$  std) are reported in Table 3.

No falls were reported during the trials. All participants were able to recover their balance.

Before starting the experimental sessions, all participants signed an informed consent. Research procedures were in accordance with the Declaration of Helsinki and was approved by the Local Ethical Committee (Prot. no. 0028266/2019).

**3.2. PIFD Algorithm Performance.** As introduced in Section 1, the metrics commonly used to quantify the performance of a PIFD strategy are the accuracy, in terms of sensitivity and specificity, and efficiency through the detection time [7, 8].

In the present study, the above-mentioned performance has been experimentally extracted by means of the protocol described in Section 2.3, asking the subject to carry out ten consecutive trials, with an intertrial time of 2 minutes (rest). The performance is computed on a final dataset of 60 perturbations (10 for each analyzed subject).

```

Routine: Logic Network Classification
Inputs:
MSMA; imSMA; //MSMA: Vector of Nc  $\widehat{m}_c$  values from cortical group "Supplementary Motor Area"
//imSMA:  $\widehat{m}$  values from cortical group SMA @ ith MT contraction
MM1; imM1; //MM1: Vector of Nc  $\widehat{m}_c$  values from cortical group "Motor Area"
//imM1:  $\widehat{m}$  values from cortical group M1 @ ith MT contraction
MS1; imS1; //MSMA: Vector of Nc  $\widehat{m}_c$  values from cortical group "Sensory-motor area"
//imSMA:  $\widehat{m}$  values from cortical group S1 @ ith MT contraction
MPPC; imPPC; //MM1: Vector of Nc  $\widehat{m}_c$  values from cortical group "Parietal area"
//imM1:  $\widehat{m}$  values from cortical group PPC @ ith MT contraction

Outputs:
Gen_Flag; //Generalization Flag. It identifies a general cortical activity increment
Lat_Flag; //Lateralization Flag. It identifies a NOT lateralized cortical involvement
Alarm_on_BoI (); //The function is used to activate a warning flag on the specific evaluated BoI
/* Body Program LogicNetwork_Classifier */
1. [Class] LogicNetwork_Classifier (imSMA, imM1, imS1, imPPC){
2.   CG_Sum = [imSMA>ThrSMA imM1>ThrM1 imS1>Thrs1 imPPC>ThrPPC]/4;
3.   if (CG_Sum>0.5) {
4.     Gen_Flag=1;
5.     Lat_flag=lateral_check ();
6.     if (Lat_flag == 1) {
7.       → call Alarm_on_BoI ();
8.     }
9.   }
10.  calibration (imSMA, imM1, imS1, imPPC); //refresh calibration values
11. }
/*Example Calibration Step */
12. [ThrSMA, ThrM1, ThrS1, ThrPPC] calibration(imSMA, imM1, imS1, imPPC) {
13. //In the first calibration section, the system embeds the extraction of the 95th
percentile-based thresholds for every cortical group.
ThrsMA = prctile (*MSMA, 95); ...; ThrPPC = prctile (*MPPC, 95);
14. //In the second one, the vector is automatically updated with the new "im" value, preparing the system for the next contraction.
15. *MSMA(0) = []; *MSMA=[*MSMA imSMA]; ...; *MPPC(0)=[]; *MPPC=[*MPPC imPPC]
16. }

```

PSEUDOCODE 1: Pseudocode of logic network classifier routine and system calibration.

TABLE 3: Data and anthropometric measurements of the analyzed subjects.

Features	Value
Age	28.3 ± 5.1 years
Height	1.72 ± 0.06 m
Weight	65.2 ± 9.4 kg
Gender distribution	83% M, 17% F
Walking speed	1.11 ± 0.07 m/s

3.2.1. *PIFD Algorithm Performance: Accuracy.* Table 4 summarizes the system performance in terms of the following: muscular response side, number of active cortical groups, number of false alarms, and, finally, sensitivity and specificity. The “response side” column identifies the lateral gastrocnemius which first intervenes to try avoiding the fall. The experimental results show that in the presence of a balanced perturbation delivery (50% on the life side, 50% on the right one), subjects react the 57.22% of the cases by contracting the left gastrocnemius. This value does not consider the missing data (MD) due to misclassifications. The report

shows how three subjects (Subs 1, 5, and 6) potentially react according to the medical literature [12, 36] by contracting the gastrocnemius of the unperturbed leg to restore balance. In the remaining cases, an anomalous stiffness on the right limb was recorded.

The “active cortical groups” column identifies the number of functional cortical groups usually above the thresholds, averaged on the 5 bands of interest. In this respect, Table 4 shows how, on average, a “nonstandard” neural behavior is detected on the  $3.24 \pm 0.73$  cortical groups (mean and standard deviation on 5 bands of interest) in the presence of perturbation (F—Table 4). Similarly, the cortical groups actively involved in the steady walking (W—Table 4) are, on average,  $1.66 \pm 0.37$ . The results support the theoretical hypothesis behind the logical network classification: a widespread (not lateralized) and general cortical activity increment could identify a possible loss of balance.

Table 4 also shows how the proposed system can reach an overall sensitivity of  $Se (\%) = 93.33 \pm 5.16\%$  and a specificity of  $Sp (\%) = 98.91 \pm 0.44\%$ , fully competitive with the state of art. A quantitative comparison with the above detailed state-of-the-art solutions is shown in Figure 5.

TABLE 4: PIFD performance report: accuracy.

Sub.	Response side	Active cortical groups	False alarms	Se (%)	Sp (%)
1	R: 50% L: 40% 10% MD* <sup>1</sup>	F: $3.22 \pm 0.83$ W: $1.70 \pm 0.82$	3	90.00 (9/10)	99.22 (386/389)
2	R: 40% L: 60%	F: $3.10 \pm 0.73$ W: $1.50 \pm 1.17$	5	100.00 (10/10)	98.32 (292/297)
3	R: 30% L: 60% 10% MD* <sup>1</sup>	F: $3.10 \pm 0.73$ W: $1.80 \pm 0.83$	4	90.00 (9/10)	98.71 (308/312)
4	R: 20% L: 70% 10% MD* <sup>1</sup>	F: $3.20 \pm 0.78$ W: $2.30 \pm 1.15$	5	90.00 (9/10)	98.55 (339/344)
5	R: 50% L: 40% 10% MD* <sup>1</sup>	F: $3.20 \pm 0.78$ W: $1.20 \pm 1.22$	2	90.00 (9/10)	99.46 (370/372)
6	R: 50% L: 50%	F: $3.10 \pm 0.73$ W: $1.50 \pm 0.97$	3	100.00 (10/10)	99.20 (374/377)
Average 1 to 6	R: 42.77% L: $57.22\% \pm 13.40\%$	F: $3.14 \pm 0.06$ W: $1.67 \pm 0.37$	$3.67 \pm 1.21$	$93.33 \pm 5.16$	$98.91 \pm 0.44$

\*<sup>1</sup>MD: missing data due to misclassification; F: fall; W: steady walking.

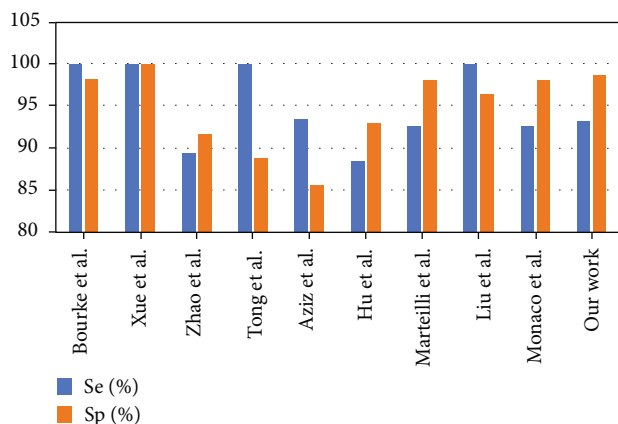


FIGURE 5: State-of-the-art comparison about the accuracy parameter of PIFD strategy.

**3.2.2. PIFD Algorithm Performance: Efficiency.** The efficiency of a PIFD strategy is typically evaluated in terms of time interval to reliably detect a loss of balance. This parameter can be derived as the time interval between the perturbation onset and the loss of balance status recognition. In this context, the proposed system has been validated by a motion capture system (MCS) to obtain, with proper precision, the perturbation onset provided by the SENLY platform in anterior-posterior direction on the selected limb.

The detection time, extracted during the experimental tests, is summarized in Table 5. They are computed considering the perturbation onset instant as the voltage step supplied

TABLE 5: PIFD performance report: efficiency.

Sub. ID	Speed (m/s)	Operating time (ms)	Detection time (ms)
1	1.05	$21.753 \pm 0.015$	$369.83 \pm 97.49$
2	1.10	$21.744 \pm 0.012$	$436.72 \pm 86.66$
3	1.00	$21.739 \pm 0.008$	$299.76 \pm 107.99$
4	1.15	$21.751 \pm 0.014$	$355.85 \pm 151.38$
5	1.18	$21.750 \pm 0.012$	$446.72 \pm 112.89$
6	1.17	$21.654 \pm 0.011$	$314.82 \pm 105.34$
Average 1 to 6	$1.11 \pm 0.07$	$21.732 \pm 0.035$	$370.62 \pm 60.85$

to SENLY via Vicon Nexus software programming (MCS). The time resolution of this rising edge is  $\leq 10$  ms, but conservatively, we considered it in the detection time.

In Table 5, the “operating time” column shows the computation time associated with the complete Computing System (Figure 2) working flow, which comprises (i) muscle trigger activation, (ii) sliding window FFT, (iii) band multiplexing, (iv) generalization and lateralization step, (v) logic network based classification, and (vi) recalibration of thresholds.

More generally, the report in Table 5 shows that, on six analyzed subjects, the implemented system requires, on average,  $370.62 \pm 60.85$  ms to detect the induced fall. More in detail, the only Computing System (Figure 2) demands, on average, for  $21.732 \pm 0.035$  ms to conclude the above-

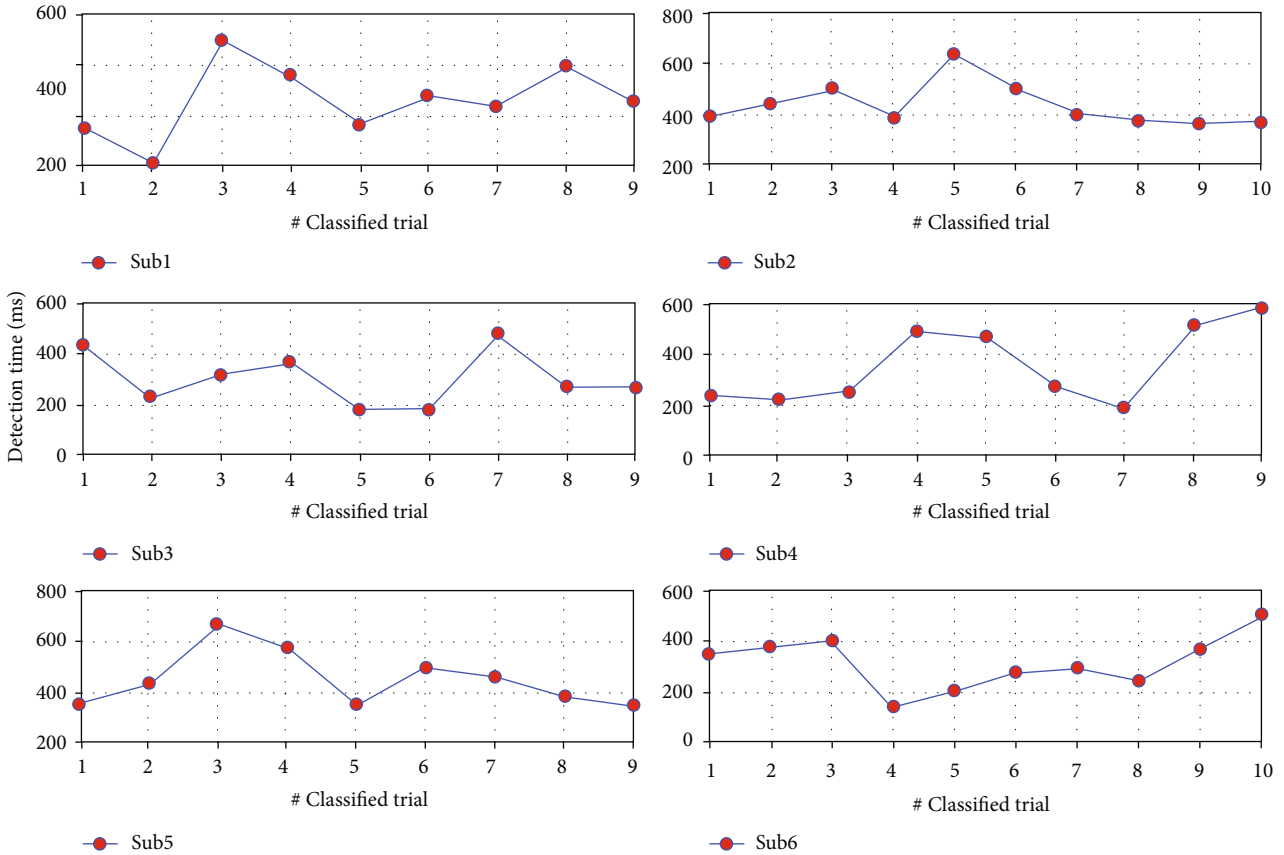


FIGURE 6: Implemented system detection times assessed on each trial and for each subject involved in the study.

defined six operations from muscle trigger activation to recalibration of thresholds.

The remaining time (~350 ms on average), with its high variability, is strictly related to the selected muscle bundle for the MT function (i.e., lateral gastrocnemius). In fact, it is better to remember that the system starts working from the contraction of the gastrocnemius (right or left independently). The times related to this physiological process remain not determinable with certainty. In this respect, the response times of the gastrocnemius constitute unavoidable delays in recognizing losses of balance and largely determine the efficiency of the system.

To provide a more complete overview of the efficiency, Figure 6 shows the trial-by-trial response times of the implemented system. In the worst case (i.e., Sub 2 and Trial 5), the system takes about 634 ms to intervene, while in the best case (i.e., Sub 6 and Trial 4), the system recognizes the loss of balance in about 160.4 ms.

The achieved detection times are competitive with respect to the state-of-the-art solutions, highlighting the system applicability in contexts of postural recovery strategy implementation.

A final comparative plot with the state-of-the-art solutions is provided in Figure 7. The plot shows the detection time versus the overall accuracy (i.e., mean between Se (%) and Sp (%)), providing an interesting metric for the performance assessment of the PIFD algorithm. Ideally, the algorithms should tend to the bottom-right corner.

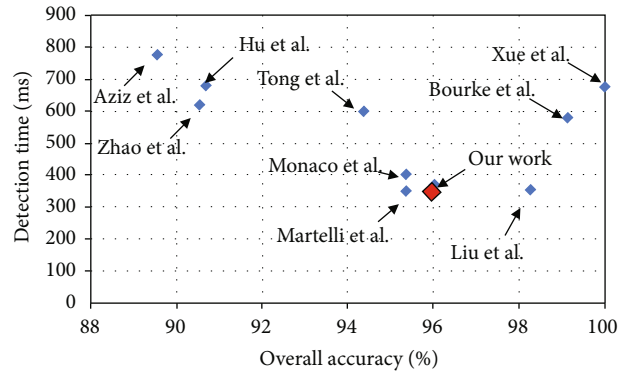


FIGURE 7: State-of-the-art comparison: detection time (ms) versus accuracy (%).

#### 4. Conclusions

In this paper, a novel methodology that early discriminates an unexpected loss of balance event from ordinary life movements, by analyzing the subjects' cortical signal modifications (at the scalp level) in the time-frequency domain has been presented.

The system was successfully tested and optimized for the early detection of balance losses when unexpected slippages occur during the walking, realizing a first-of-a-kind wearable sensor-based recognition system for induced slippages.

Experimental validation on six young adults demonstrated that the system recognizes a loss of balance with a sensitivity of 93.33% and a specificity of 98.91%. In terms of efficiency, the system asks for 370.62 ms to recognize a balance perturbation.

The here-proposed PIFD strategy has been designed to be low compute intensive and thus suitable for the implementation on a microcontroller or FPGA.

The performance (accuracy and detection time) suggest the technique for real-time applications. Despite this, future perspectives concern the application of the PIFD methodology to a catchment area more relevant to the objective (group of persons 65+), as well as the identification of the proper protection or mitigation strategies (e.g., by using wearable robotic platforms) and the improvement of the acquisition system wearability.

## Data Availability

The data used to support the findings of this study are available from the corresponding author upon request.

## Conflicts of Interest

The authors declare that there is no conflict of interest regarding the publication of this paper.

## Acknowledgments

This work was supported by the project AMICO (Assistenza Medica In COntextual awareness, AMICO Project ARS01\_00900) by the National Programs (PON) of the Italian Ministry of Education, University and Research (MIUR) (Decree no. 267).

## References

- [1] J. Massion, "Postural control system," *Current Opinion in Neurobiology*, vol. 4, no. 6, pp. 877–887, 1994.
- [2] M. P. Murray, A. A. Seireg, and S. B. Sepic, "Normal postural stability and steadiness: quantitative assessment," *The Journal of Bone & Joint Surgery*, vol. 57, no. 4, pp. 510–516, 1975.
- [3] D. S. Marigold and J. E. Miaszsek, "Whole-body responses: neural control and implications for rehabilitation and fall prevention," *The Neuroscientist*, vol. 15, no. 1, pp. 36–46, 2009.
- [4] J. E. Miaszsek, "Neural control of walking balance: if falling then react else continue," *Exercise and Sport Sciences Reviews*, vol. 34, no. 3, pp. 128–134, 2006.
- [5] N. Noury, T. Herve, V. Rialle et al., "Monitoring behavior in home using a smart fall sensor and position sensors," in *1st Annual International IEEE-EMBS Special Topic Conference on Microtechnologies in Medicine and Biology. Proceedings (Cat. No.00EX451)*, pp. 607–610, Lyon, France, 2000.
- [6] O. P. Ryyänen, S. L. Kivelä, R. Honkanen, and P. Laippala, "Falls and lying helpless in the elderly," *Zeitschrift für Gerontologie*, vol. 25, no. 4, pp. 278–282, 1992.
- [7] S. Chaudhuri, H. Thompson, and G. Demiris, "Fall detection devices and their use with older adults: a systematic review," *Journal of Geriatric Physical Therapy*, vol. 37, no. 4, pp. 178–196, 2014.
- [8] X. Hu and X. Qu, "Pre-impact fall detection," *BioMedical Engineering OnLine*, vol. 15, no. 1, p. 61, 2016.
- [9] X. Hu and X. Qu, "An individual-specific fall detection model based on the statistical process control chart," *Safety Science*, vol. 64, pp. 13–21, 2014.
- [10] D. Martelli, F. Artoni, V. Monaco, A. M. Sabatini, and S. Micera, "Pre-impact fall detection: optimal sensor positioning based on a machine learning paradigm," *PLoS One*, vol. 9, no. 3, article e92037, 2014.
- [11] J. Liu and T. E. Lockhart, "Development and evaluation of a prior-to-impact fall event detection algorithm," *IEEE Transactions on Biomedical Engineering*, vol. 61, no. 7, pp. 2135–2140, 2014.
- [12] D. A. Winter, *Biomechanics and Motor Control of Human Movement*, John Wiley & Sons, 2009.
- [13] A. K. Bourke, K. J. O'Donovan, and G. ÓLaighin, "The identification of vertical velocity profiles using an inertial sensor to investigate pre-impact detection of falls," *Medical Engineering & Physics*, vol. 30, no. 7, pp. 937–946, 2008.
- [14] L. Tong, Q. Song, Y. Ge, and M. Liu, "HMM-based human fall detection and prediction method using tri-axial accelerometer," *IEEE Sensors Journal*, vol. 13, no. 5, pp. 1849–1856, 2013.
- [15] V. Monaco, P. Tropea, F. Aprigliano et al., "An ecologically-controlled exoskeleton can improve balance recovery after slippage," *Scientific Reports*, vol. 7, no. 1, article 46721, 2017.
- [16] N. Pannurat, S. Thiemjarus, and E. Nantajeewarawat, "Automatic fall monitoring: a review," *Sensors*, vol. 14, no. 7, pp. 12900–12936, 2014.
- [17] D. De Venuto, V. F. Annese, M. de Tommaso, E. Vecchio, and A. L. Sangiovanni Vincentelli, "Combining EEG and EMG signals in a wireless system for preventing fall in neurodegenerative diseases," in *Ambient Assisted Living*, B. Andò, P. Siciliano, V. Marletta, and A. Monteriù, Eds., vol. 11 of Biosystems & Biorobotics, Springer, Cham, Switzerland, 2015.
- [18] V. F. Annese and D. De Venuto, "Fall-risk assessment by combined movement related potentials and co-contraction index monitoring," *2015 IEEE Biomedical Circuits and Systems Conference (BioCAS)*, 2015, pp. 1–4, Atlanta, GA, USA, 2015.
- [19] D. de Venuto, D. T. Castro, Y. Ponomarev, and E. Stikvoort, "0.8  $\mu$ W 12-bit SAR ADC sensors interface for RFID applications," *Microelectronics Journal*, vol. 41, no. 11, pp. 746–751, 2010.
- [20] V. F. Annese and D. De Venuto, "The truth machine of involuntary movement: FPGA based cortico-muscular analysis for fall prevention," in *2015 IEEE International Symposium on Signal Processing and Information Technology (ISSPIT)*, pp. 553–558, Abu Dhabi, United Arab, 2015.
- [21] D. De Venuto, M. J. Ohletz, and B. Riccò, "Digital window comparator DfT scheme for mixed-signal ICs," *Journal of Electronic Testing*, vol. 18, no. 2, pp. 121–128, 2002.
- [22] D. De Venuto and M. J. Ohletz, "On-chip test for mixed-signal ASICs using two-mode comparators with bias-programmable reference voltages," *Journal of Electronic Testing*, vol. 17, no. 3/4, pp. 243–253, 2001.
- [23] O. Aziz, C. M. Russell, E. J. Park, S. Member, and S. N. Robynovitch, "The effect of window size and lead time on pre-impact fall detection accuracy using support vector machine analysis of waist mounted inertial sensor data," in *2014 36th Annual International Conference of the IEEE Engineering in Medicine and Biology Society*, pp. 30–33, Chicago, IL, USA, 2014.



- [24] Y. Lajoie and S. P. Gallagher, "Predicting falls within the elderly community: comparison of postural sway, reaction time, the Berg balance scale and the Activities-specific Balance Confidence (ABC) scale for comparing fallers and non-fallers," *Archives of Gerontology and Geriatrics*, vol. 38, no. 1, pp. 11–26, 2004.
- [25] G. Wu and S. Xue, "Portable preimpact fall detector with inertial sensors," *IEEE Transactions on Neural Systems and Rehabilitation Engineering*, vol. 16, no. 2, pp. 178–183, 2008.
- [26] G. Zhao, Z. Mei, D. Liang et al., "Exploration and implementation of a pre-impact fall recognition method based on an inertial body sensor network," *Sensors*, vol. 12, no. 11, pp. 15338–15355, 2012.
- [27] D. De Venuto, V. F. Annese, and G. Mezzina, "An embedded system remotely driving mechanical devices by P300 brain activity," in *Design, Automation and Test in Europe Conference and Exhibition (DATE), 2017*, pp. 1014–1019, Lausanne, Switzerland, 2017.
- [28] J. P. Varghese, R. E. McIlroy, and M. Barnett-Cowan, "Perturbation-evoked potentials: significance and application in balance control research," *Neuroscience & Biobehavioral Reviews*, vol. 83, pp. 267–280, 2017.
- [29] E. Wittenberg, J. Thompson, C. S. Nam, and J. R. Franz, "Neuroimaging of human balance control: a systematic review," *Frontiers in Human Neuroscience*, vol. 11, p. 170, 2017.
- [30] A. Mierau, B. Pester, T. Hülsdünker, K. Schiecke, H. K. Strüder, and H. Witte, "Cortical correlates of human balance control," *Brain Topography*, vol. 30, no. 4, pp. 434–446, 2017.
- [31] S. Makeig, K. Gramann, T.-P. Jung, T. J. Sejnowski, and H. Poizner, "Linking brain, mind and behavior," *International Journal of Psychophysiology*, vol. 73, no. 2, pp. 95–100, 2009.
- [32] J. F. Cavanagh and M. J. Frank, "Frontal theta as a mechanism for cognitive control," *Trends in Cognitive Sciences*, vol. 18, no. 8, pp. 414–421, 2014.
- [33] W. Klimesch, R. Fellinger, and R. Freunberger, "Alpha oscillations and early stages of visual encoding," *Frontiers in Psychology*, vol. 2, p. 118, 2011.
- [34] A. K. Engel and P. Fries, "Beta-band oscillations — signalling the status quo?," *Current Opinion in Neurobiology*, vol. 20, no. 2, pp. 156–165, 2010.
- [35] C. Neuper and G. Pfurtscheller, "Event-related dynamics of cortical rhythms: frequency-specific features and functional correlates," *International Journal of Psychophysiology*, vol. 43, no. 1, pp. 41–58, 2001.
- [36] T. Solis-Escalante, J. van der Crujisen, D. de Kam, J. van Kordelaar, V. Weerdesteyn, and A. C. Schouten, "Cortical dynamics during preparation and execution of reactive balance responses with distinct postural demands," *NeuroImage*, vol. 188, pp. 557–571, 2019.
- [37] D. De Venuto and J. Rabaey, "RFID transceiver for wireless powering brain implanted microelectrodes and backscattered neural data collection," *Microelectronics Journal*, vol. 45, no. 12, pp. 1585–1594, 2014.
- [38] L. B. Luciani, V. Genovese, V. Monaco, L. Odetti, E. Cattin, and S. Micera, "Design and evaluation of a new mechatronic platform for assessment and prevention of fall risks," *Journal of Neuroengineering and Rehabilitation*, vol. 9, no. 1, p. 51, 2012.
- [39] F. Aprigliano, D. Martelli, P. Tropea, G. Pasquini, S. Micera, and V. Monaco, "Aging does not affect the intralimb coordination elicited by slip-like perturbation of different intensities," *Journal of Neurophysiology*, vol. 118, no. 3, pp. 1739–1748, 2017.
- [40] D. Martelli, F. Aprigliano, P. Tropea, G. Pasquini, S. Micera, and V. Monaco, "Stability against backward balance loss: age-related modifications following slip-like perturbations of multiple amplitudes," *Gait & Posture*, vol. 53, pp. 207–214, 2017.
- [41] M. Sazgar and M. G. Young, "EEG Artifacts," in *Absolute Epilepsy and EEG Rotation Review*, pp. 149–162, Springer, Cham, Switzerland, 2019.
- [42] S. Blum, N. S. J. Jacobsen, M. G. Bleichner, and S. Debener, "A Riemannian modification of artifact subspace reconstruction for EEG artifact handling," *Frontiers in Human Neuroscience*, vol. 13, p. 141, 2019.
- [43] V. F. Annese and D. De Venuto, "Gait analysis for fall prediction using EMG triggered movement related potentials," in *2015 10th International Conference on Design and Technology of Integrated Systems in Nanoscale Era (DTIS)*, pp. 1–6, Naples, Italy, 2015.
- [44] M. Blagojevic, M. Kayal, M. Gervais, and D. De Venuto, "SOI hall-sensor front end for energy measurement," *IEEE Sensors Journal*, vol. 6, no. 4, pp. 1016–1021, 2006.
- [45] S. Carrara, M. D. Torre, A. Cavallini, D. De Venuto, and G. De Micheli, "Multiplexing pH and temperature in a molecular biosensor," in *2010 Biomedical Circuits and Systems Conference (BioCAS)*, pp. 146–149, Paphos, Cyprus, 2010.